

Electronic Thesis and Dissertation Repository

8-24-2012 12:00 AM

Quantification of bone and cement strains surrounding a distal ulnar implant with varying cement-stem interface conditions

Sayward R. Fetterly
The University of Western Ontario

Supervisor
Dr. Cynthia Dunning
The University of Western Ontario

Graduate Program in Mechanical and Materials Engineering
A thesis submitted in partial fulfillment of the requirements for the degree in Master of Engineering Science
© Sayward R. Fetterly 2012

Follow this and additional works at: <https://ir.lib.uwo.ca/etd>



Part of the [Biomedical Devices and Instrumentation Commons](#)

Recommended Citation

Fetterly, Sayward R., "Quantification of bone and cement strains surrounding a distal ulnar implant with varying cement-stem interface conditions" (2012). *Electronic Thesis and Dissertation Repository*. 777. <https://ir.lib.uwo.ca/etd/777>

This Dissertation/Thesis is brought to you for free and open access by Scholarship@Western. It has been accepted for inclusion in Electronic Thesis and Dissertation Repository by an authorized administrator of Scholarship@Western. For more information, please contact wlsadmin@uwo.ca.

QUANTIFICATION OF BONE AND CEMENT STRAINS SURROUNDING A DISTAL ULNAR IMPLANT WITH VARYING CEMENT-STEM INTERFACE CONDITIONS

(Spine Title: Bone & Cement Strains Following Distal Ulnar Arthroplasty)

(Thesis format: Integrated Article)

By

Sayward R. Fetterly

Graduate Program in Mechanical and Materials Engineering

A thesis submitted in partial
fulfillment of the requirements
for the degree of Master of
Engineering Science

The School of Graduate and Postdoctoral Studies
The University of Western Ontario
London, Ontario, Canada

© Sayward R. Fetterly 2012

THE UNIVERSITY OF WESTERN ONTARIO
SCHOOL OF GRADUATE AND POSTDOCTORAL STUDIES

Certificate of Examination

SUPERVISOR

Cynthia E. Dunning, Ph.D., P. Eng.
Department of Mechanical and Materials Engineering
Department of Surgery
Department of Medical Biophysics

EXAMINING BOARD

Michael D. Naish, Ph.D., P.Eng.
Department of Mechanical and Materials Engineering

Tim A. Newson, Ph.D., P.Eng.
Department of Civil and Environmental Engineering

Liyang Jiang, Ph.D., P.Eng.
Department of Mechanical and Materials Engineering

The thesis by **Sayward R. Fetterly** entitled:

**QUANTIFICATION OF BONE AND CEMENT STRAINS SURROUNDING A DISTAL ULNAR
IMPLANT WITH VARYING CEMENT-STEM INTERFACE CONDITIONS**

is accepted in partial fulfillment of the
requirements for the degree of Master of
Engineering Science

Date

Chair of the Thesis Examination Board

Abstract

Implant loosening following joint replacement surgery is a health-care concern. The role of implant-cement debonding on the propensity of loosening has received limited attention. This thesis examines changes in strains within the cement mantle and bone surrounding distal ulnar implants, as a function of cement-stem interface bonding.

A method to embed strain gauges within the cement mantle of the restrictive distal ulnar canal was developed. This technique was applied in 8 cadaveric distal ulnae, where strains were quantified at 2 internal and 5 external (*i.e.*, bone surface) locations under torsion and bending loads with bonded and de-bonded cement-stem interfaces. For a bonded stem, the distal-most external strains increased under all loading scenarios, while proximal internal strains increased only under torsional loading ($p < 0.05$). A finite element model of the testing scenarios with bending loads gave similar results. This work will contribute to the future optimization of distal ulnar implants.

Keywords: distal radioulnar joint, distal ulnar implant, bone cement, cement-stem interface conditions, implant debonding, strain gauge embedment

Statement of Co-Authorship

The research conducted in this study resulted from a collaborative effort of multiple individuals. Without their assistance this thesis could not have been completed.

Chapter 1: Sayward Fetterly – wrote manuscript; Cynthia Dunning – reviewed and revised manuscript

Chapter 2: Sayward Fetterly – study design, data collection, data analysis, wrote manuscript; Yara Hosein – support in developing the cementing technique; Cynthia Dunning – study design, data review, reviewed and revised manuscript

Chapter 3: Sayward Fetterly – study design, data collection, data analysis, wrote manuscript; Graham King – surgical assistance; Cynthia Dunning – study design, data review, reviewed and revised manuscript

Chapter 4: Sayward Fetterly – study design, data collection, data analysis, wrote manuscript; Jaques Milner – wrote and operated material property assignment software; Mark Neuert – study design, software support; Cynthia Dunning – study design, data review, reviewed and revised manuscript

Chapter 5: Sayward Fetterly – wrote manuscript; Cynthia Dunning – reviewed and revised manuscript

Acknowledgements

Foremost, I would like to thank Dr. Cynthia Dunning for going above and beyond her duties as an advisor. Without your dedication, support, and encouragement this thesis would not have been possible. Thank you for the opportunity to work with such a wonderful mentor.

I would also like to thank the members of the Jack McBain Biomechanical Testing Laboratory. In particular: Yara for her numerous hours of cementing support, Stew and Tim for their abundance of knowledge, Jake for his crash course in SolidWorks, and Mark for his incredible patience in teaching me Abaqus®. Thank you for making my time at Western both fun and memorable.

Last but never least I would like to thank my family. Thank you for supporting of all my choices and encouraging me to do my best. With a special thank you to my parents, having you there for me means more to me than you could ever know.

Dedication

To my wonderful parents for their eternal love and support,
my friends for their optimism and encouragement,
and Greg for his open ears and kind heart.

Table of Contents

Certificate of Examination	ii
Abstract	iii
Statement of Co-Authorship	iv
Acknowledgements	v
Dedication.....	vi
List of Figures	x
List of Tables	xii
List of Equations	xiv
List of Appendices	xv
List of Abbreviations, Symbols, and Nomenclature	xvi
Chapter 1 - Introduction	1
1.1 The Distal Radioulnar Joint (DRUJ)	2
1.1.1 Joint Anatomy and Motion	2
1.1.2 DRUJ Injuries and Disorders.....	4
1.2 Surgical Treatment Options for DRUJ Disorders.....	5
1.3 Distal Ulnar Arthroplasty	8
1.3.1 Bone Cement	10
1.3.2 Implant Loosening and Debonding.....	13
1.3.3 Stress Shielding	14
1.4 Post Arthroplasty Strain Measurement	15

1.4.1 Piezoresistive foil gauge overview	15
1.4.2 Wheatstone Bridges.....	19
1.4.3 Strain Gauge Embedment.....	19
1.5 Finite Element Analysis (FEA).....	23
1.5.1 Finite Element Components	24
1.5.2 Model Parameters	25
1.6 Study Rationale	28
1.7 Objectives and Hypotheses.....	29
1.8 Thesis Outline.....	30
1.9 References	30
Chapter 2 - Development and Validation of a Strain Gauge Embedment Methodology for Use with PMMA Bone Cement	39
2.1 Introduction	39
2.2 Materials and Methods.....	41
2.3 Results.....	44
2.4 Discussion.....	48
2.5 References	50
Chapter 3 - Experimental Examination of the Effect of Implant Debonding on Load Transfer	52
3.1 Introduction	52
3.2 Materials and Methods.....	53

3.3	Results.....	63
3.4	Discussion.....	65
3.5	References	72
Chapter 4 - Finite Element Examination of the Effect of Implant Debonding on Load Transfer		75
4.1	Introduction	75
4.2	Materials and Methods.....	77
4.3	Results.....	83
4.4	Discussion.....	88
4.5	References	91
Chapter 5 - Summary and Conclusions		93
5.1	Summary.....	93
5.2	Strengths and Limitations	95
5.3	Future Directions	97
5.4	Overall Significance.....	99
5.5	References	99
Appendices		100
Curriculum Vitae		180

List of Figures

Figure 1.1: Left forearm in supinated position	3
Figure 1.2: Surgical techniques for repair of the DRUJ.....	6
Figure 1.3: Commercially available distal ulnar head implants.....	11
Figure 1.4: Uniaxial strain gauge	16
Figure 1.5: Triaxial gauge orientation.....	18
Figure 1.6: Wheatstone bridge circuit	20
Figure 1.7: Elements options with associated nodes	26
Figure 2.1: Drift of an embedded strain gauge	45
Figure 2.2: Linearity of strain response	46
Figure 3.1: Internal gauge position and orientation.....	55
Figure 3.2: MicroScribe®	56
Figure 3.3: Implant oriented for embedment	58
Figure 3.4: External gauge location and alignment.....	59
Figure 3.5: Experimental setup and points of load application	61
Figure 3.6: Implant orientation pre and post-ulna torsion to 7°	64
Figure 3.7: Mean and standard deviation between specimens in bending	66
Figure 3.8: Mean and standard deviation between specimens in combined loading ..	67
Figure 3.9: Mean and standard deviation between specimens in torsion.....	68
Figure 4.1: Strain output using large and small meshes.....	84
Figure 4.2: Strain output of experimental and FE models.....	85
Figure 4.3: Bland-Altman plots for each interface condition	87

Figure A.1: Drift of an encapsulated strain gauge	107
Figure A.2: Gauging baseplate	111
Figure A.3: Required tools for strain gauge fixation	112
Figure A.4: LabVIEW program front panel	114
Figure A.5: LabVIEW program back panel	115
Figure A.6: Specimen number 09-12057 in potting fixture	119
Figure A.7: Experimental loading protocol	130
Figure A.8: Verification of 3D image orientation.	158
Figure A.9: Thresholding	159
Figure A.10: Axial view of a polyline series and mask	161
Figure A.11: Editing the geometry of the imported bone IGS file	164
Figure A.12: Axial view of the coordinate points selected in Mimics.....	166
Figure A.13: Bone model segmented to denote external gauge locations.	168
Figure A.14: Axial view of the implant coordinate points	168
Figure A.15: Implant and cement model segmented to denote gauge locations.	170
Figure A.16: Implant and cement model	172
Figure A.17: Completed node set for both internal gauge locations	175
Figure A.18: Probe values input window	179

List of Tables

Table 2.1: Coefficients of variation within session, within day and between days	47
Table 4.1: Difference between independent and averaged gauge response.....	78
Table 4.2: Development of bone and cement model	80
Table 4.3: RMSE for bonded and debonded conditions	86
Table A.1: Accuracy of encapsulated gauge throughout load application range	108
Table A.2: Hysteresis for strain gauge embedment pilot study	116
Table A.3: Average recorded principal strain by load and testing day	117
Table A.4: Standard deviation of recorded principal strain	117
Table A.5: Debonding characteristics of release agent coated implants	126
Table A.6: Principal strain in specimen 11-03022 under bending load application.....	133
Table A.7: Principal strain in specimen 10-01004 under bending load application.....	134
Table A.8: Principal strain in specimen 11-03026 under bending load application.....	135
Table A.9: Principal strain in specimen 09-12057 under bending load application.....	136
Table A.10: Principal strain in specimen 09-13055 under bending load application.....	137
Table A.11: Principal strain in specimen 10-06020 under bending load application.....	138
Table A.12: Principal strain in specimen 11-03045 under bending load application.....	139
Table A.13: Principal strain in specimen 11-03057 under bending load application.....	140
Table A.14: Principal strain in specimen 11-03022 during torsional loading.....	141
Table A.15: Principal strain in specimen 10-01004 during torsional loading.....	142
Table A.16: Principal strain in specimen 11-03026 during torsional loading.....	143
Table A.17: Principal strain in specimen 09-12057 during torsional loading.....	144

Table A.18: Principal strain in specimen 09-13055 during torsional loading.....	145
Table A.19: Principal strain in specimen 10-06020 during torsional loading.....	146
Table A.20: Principal strain in specimen 11-02045 during torsional loading.....	147
Table A.21: Principal strain in specimen 11-03057 during torsional loading.....	148
Table A.22: Principal strain in specimen 11-03022 during combined loading.....	149
Table A.23: Principal strain in specimen 10-01004 during combined loading.....	150
Table A.24: Principal strain in specimen 11-03026 during combined loading.....	151
Table A.25: Principal strain in specimen 09-12057 during combined loading.....	152
Table A.26: Principal strain in specimen 09-13055 during combined loading.....	153
Table A.27: Principal strain in specimen 10-06020 during combined loading.....	154
Table A.28: Principal strain in specimen 11-03045 during combined loading.....	155
Table A.29: Principal strain in specimen 11-03057 during combined loading.....	156

List of Equations

Equation 1	17
Equation 2	17
Equation 3	17
Equation 4	24
Equation 5	76
Equation 6	76
Equation 7	76
Equation 8	81
Equation 9	167
Equation 10	167
Equation 11	169
Equation 12	169

List of Appendices

Appendix 1	– Glossary of Terms	101
Appendix 2	– Preliminary Testing of Gauge Carrier for Internal Strain Gauge Embedment.....	103
Appendix 3	– Cementing Technique.....	110
Appendix 4	– Internal Strain Gauge Application Technique.....	111
Appendix 5	– Strain Data Collection Program	114
Appendix 6	– Gauge Embedment Pilot Study Strain Data.....	116
Appendix 7	– Detailed Specimen Information.....	118
Appendix 8	– Fixture Utilized in the Ulnar Fixation Process.....	119
Appendix 9	– Cement-Stem Bonded/Debonded Interface Testing Procedure	120
Appendix 10	– Debonding Agent Validation.....	125
Appendix 11	– External Strain Gauge Application Technique	128
Appendix 12	– Loading Protocol	130
Appendix 13	– Free Body Diagram of Ulna with Loads	131
Appendix 14	– Experimentally Derived Principal Strain Data.....	132
Appendix 15	– Detailed Bone and Implant Modeling Process	157

List of Abbreviations, Symbols, and Nomenclature

$^{\circ}$ – degrees

μ – micro

ϵ – strain

ρ_{density} – apparent density

$\rho_{\text{resistivity}}$ – resistivity

σ – stress

τ – shear stress

3D – three dimensional

A – cross-sectional area

ASTM – American Society for Testing and Materials

cm – centimetre

CoV – coefficient of variation

CT – computed tomography

DRUJ – distal radioulnar joint

E – elastic modulus

F – applied forces

F_f – coefficient of friction

FEA – finite element analysis

GB – gigabyte

h – hour

k – element stiffness matrix

L – length

LDPE – low density polyethylene

mm – millimetre

MMA – methylmethacrylate

N – newton

PMMA – poly(methyl methacrylate)

PRUJ – proximal radioulnar joint

PVC – polyvinyl chloride

R – resistance

RAM – random access memory

RMSE – root mean squared error

s – second

Std Dev – standard deviation

u – nodal displacements

V – volts

V_{in} – input voltage

V_{out} – output voltage

Chapter 1 - Introduction

***OVERVIEW:** Distal ulnar implants are one of the options available to surgeons in the treatment of painful and debilitating disorders of the distal radioulnar joint. As with many implant designs, loosening of the prosthesis and resorption of the surrounding bone are potential complications that would lead to the need for revision surgery. The ultimate goal of this thesis' work is to improve the current understanding of the stress/strain distribution in the cement and bone surrounding a distal ulnar implant with fixed versus debonded interface conditions. This is done using experimental and finite element modeling techniques. This chapter presents the anatomy, disorders, and treatment options of the distal radioulnar joint, as well as the necessary background information for both the experimental and finite element methods used throughout this study. The chapter concludes with the study rationale, objectives and hypothesis. Definitions of medical terminology for those readers who may be unfamiliar are available in Appendix 1.*

1.1 The Distal Radioulnar Joint (DRUJ)

1.1.1 Joint Anatomy and Motion

The forearm is comprised of two bones, the radius and the ulna, which articulate in two distinct locations (Figure 1.1). The synovial joints at the elbow (*i.e.*, proximal radioulnar joint, PRUJ) and the wrist (*i.e.*, distal radioulnar joint, DRUJ) allow for rotation of the hand about the long axis of the forearm. In supination, the ulna is located medially and the two bones are parallel. As the forearm rotates into the pronated position, the distal radius rotates about the ulna through an arc of approximately 130-180⁰, with the midpoint defined as the neutral position (Darcus and Salter, 1953; Salter and Darcus, 1953; Shaaban *et al.*, 2008). Load distribution between the radius and ulna varies throughout forearm rotation, with less radial and greater ulnar load in pronation (Ekenstam *et al.*, 1984). On average, 80% of loads applied to the hand travel through radius and the remaining 20% through the ulna (Plamer and Werner, 1983).

The DRUJ behaves as a pivot, with the ulnar head rotating within the sigmoid notch of the distal radius. Though previously this rotation was attributed to the movement of the radius about a stationary ulna, this assessment of the joint dynamics is incomplete. In actuality, radial-ulnar movement incorporates both rotation and sliding components due to the curvature of the sigmoid notch being 4-7 mm larger than that of the ulnar head (Ekenstam and Hagert, 1985; Ekenstam, 1992).

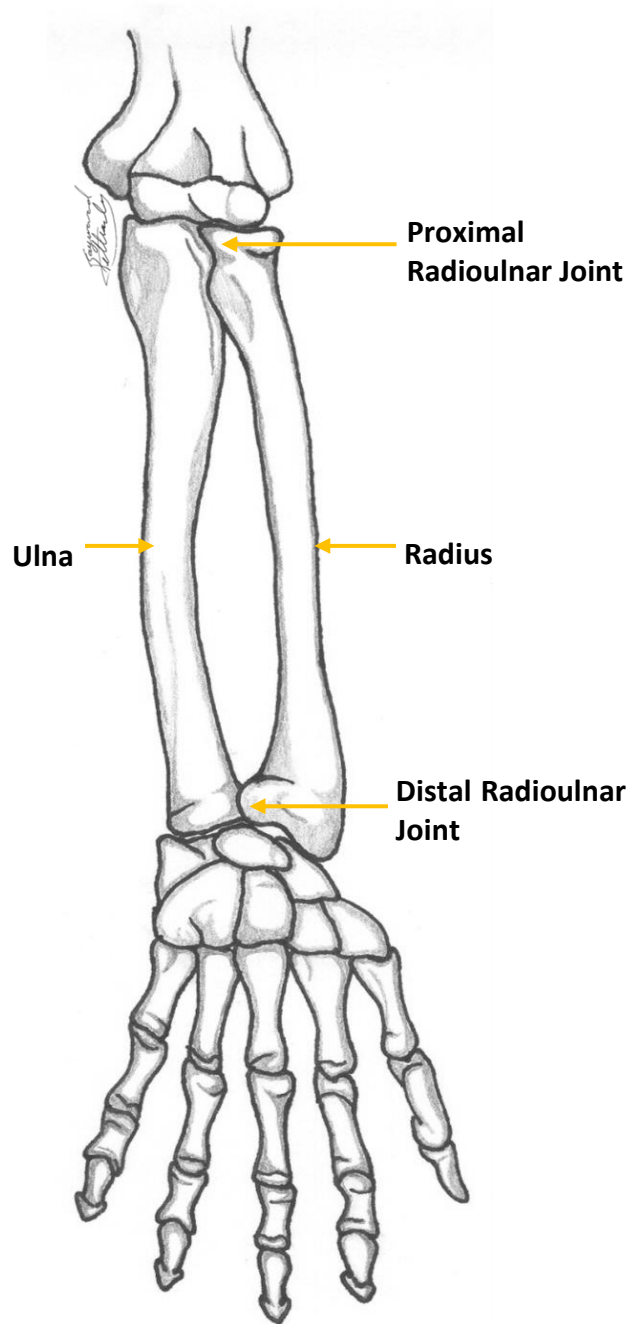


Figure 1.1: Left forearm in supinated position

An anterior view of the left forearm in supination is depicted. The forearm is comprised of two bones, the radius and ulna, which articulate at the distal and proximal radioulnar joints.

The ulnar head glides from a posterior-distal to an anterior-proximal position as the forearm moves from pronation to supination (Plamer and Werner, 1983). Furthermore, the ulna moves slightly laterally while the radius travels medially into pronation, and the reverse is true for supination (Patrick, 1946; Ray *et al.*, 1951).

There has been one reported study that used an instrumented ulna to experimentally determine the loading of the distal radial ulnar joint in a cadaver forearm. This study, conducted by Gorden *et al.* (2006), found torsional loads up to 0.13 Nm in the distal radioulnar joint during unrestrained forearm rotation. They also determined that during unresisted motion, loads across the DRUJ were highly variable ranging from 2 N to a maximum of 26 N.

1.1.2 DRUJ Injuries and Disorders

There are multiple sources of injury to the DRUJ, from chronic conditions including congenital disorders and arthritis, to traumatic injuries such as fractures, ligament tears, and dislocations (Cooney, 1993; Chidgey, 1995). In particular, the wrist is affected in 50% of rheumatoid arthritis patients in the first two years, increasing to >90% after 10 years (Trieb, 2008). Rheumatoid arthritis has been shown to directly impact the DRUJ in approximately 30% of patients (Weiler and Bogoch, 1995), and the second most common complication from Colles' (*i.e.*, wrist) fractures is arthritis of the DRUJ (Cooney *et al.*, 1980; Roysam, 1993). These disorders are commonly associated with pain, instability, and restrictions in forearm rotation and grip strength (Bell *et al.*, 1985). Since use of the hand and wrist are required for most routine activities, these symptoms can severely impact the functionality and enjoyment of life for many patients. As a result,

the aim of DRUJ treatments is to reduce pain and restore functionality to the joint (Peterson *et al.*, 1995).

1.2 Surgical Treatment Options for DRUJ Disorders

Current surgical treatment options for DRUJ disorders include ulnar head resection (Darrach's procedure), ulnar shortening osteotomy, Sauve-Kapandji procedure, and distal ulnar arthroplasty (Figure 1.2).

Ulnar head resection is utilized in the treatment of severely unstable or arthritic joints. Though the origin of this procedure dates back to the 1980's (Sauerbier, 2002), William Darrach is usually associated with the surgery for his work performed in the early 1900's (Darrach, 1913). In this procedure the distal ulnar head is removed and the patient's arm immobilized until fully healed (Figure 1.2A). However, despite the initial success of the surgery, it is associated with multiple complications. Post-surgery impairments to forearm motion, grip strength, wrist circumduction, and the hand's lifting capabilities have been observed (Garcia-Elias, 2002). Aside from the functional loss, clicking of the wrist during forearm rotation, and ulnar migration of the carpus resulting in hand and wrist deformity have also been reported (Goncalves, 1974; Bell *et al.*, 1985). Moreover, the shortened ulna, resulting from the procedure, often impinges on the radius causing persistent pain, which is known as Ulnar Impingement Syndrome. The poor results associated with Darrach's procedure are a direct result of the removal of the ulnar head which is not a vestigial bone, but rather essential to joint functionality (Bell *et al.*, 1985; Garcia-Elias, 2002; Sauerbier, 2002).

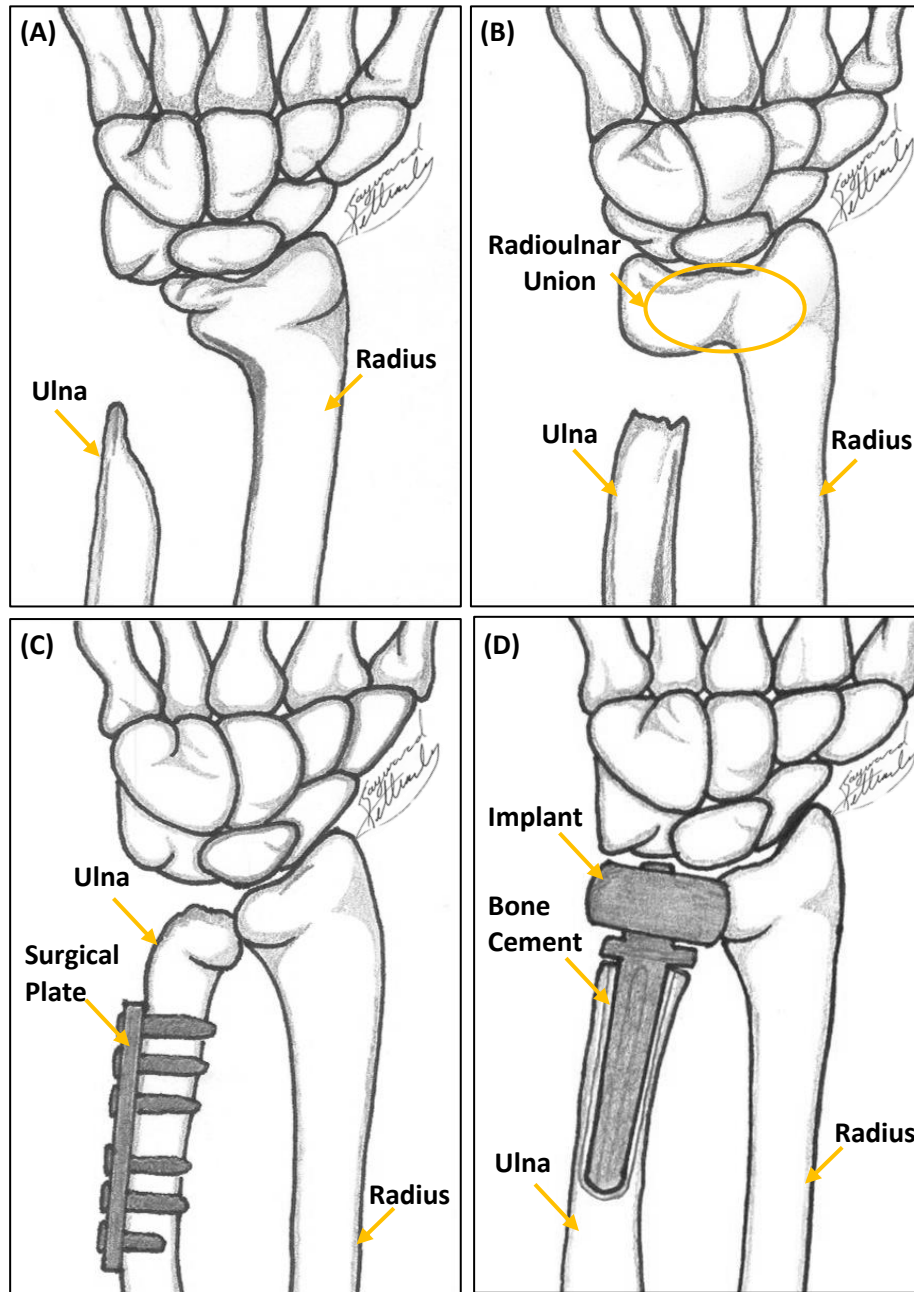


Figure 1.2: Surgical techniques for repair of the DRUJ

Several surgical techniques are available for repair of the DRUJ including: **(A)** Darrach's procedure, post ulnar head resection; **(B)** Sauve-Kapandji procedure, with full distal union of the ulna and radius; **(C)** Ulnar shortening, the resected ulna stabilized with a surgical plate; and **(D)** Distal ulnar arthroplasty, implant fixated through the use of bone cement.

Multiple alternatives to Darrach's procedure have been proposed to attempt and alleviate DRUJ discomfort while minimizing surgical complications. The Sauve-Kapandji procedure involves the resection of a segment of the ulna just proximal to the ulnar head and the fusing of the remaining distal ulna to the radius (Figure 1.2B). The results of this procedure are consistently better than those obtained through ulnar head resection (Nakamura *et al.*, 1992; Vincent *et al.*, 1993; George *et al.*, 2004). However, though the procedure does produce satisfactory results, there are still multiple complications. Following the procedure, pain, loss of grip strength, joint instability and clicking sounds during wrist and forearm movement have all been noted. As well, Ulnar Impingement Syndrome remains a problem, as the shortened ulna may still impinge on the radius (Nakamura *et al.*, 1992; Carter and Stuart, 2000).

Another alternative to Darrach's procedure is ulnar shortening, in which 1-3 mm of the distal ulna is removed and a surgical plate applied to unite the shortened bone while enhancing post-surgical stability (Figure 1.2C). Though this procedure has been successful in treating early post-traumatic osteoarthritis and ulnar impaction syndrome, its applications are very limited (Chun, 1993; Scheker and Severo, 2001). Ulnar shortening is unsuitable for severely arthritic patients or those with damage to the ulnar head (Loh *et al.*, 1999). The procedure has also been associated with joint instability, and patient complaints of plate irritation, necessitating its removal through additional surgeries (Scheker and Severo, 2001; Gaebler and McQueen, 2003).

Though there are multiple resection surgeries in use to treat DRUJ patients, none are able to fully restore the joint to its original functioning condition. Complications due to

pain and instability can impinge on quality of life and leave patients dissatisfied with the procedure (Goncalves, 1974; Carter and Stuart, 2000; Scheker and Severo, 2001; Sauerbier, 2002). This is particularly evident in young or active individuals where complications are more prevalent (Ozer and Scheker, 2006), and has given rise to the use of joint replacement surgery, or arthroplasty.

1.3 Distal Ulnar Arthroplasty

Distal ulnar arthroplasty is preferable to resection as it preserves the anatomical relationship of the joint by replacing the ulnar head with a mechanical implant (Figure 1.2D). As such, the diseased or damaged ulnar head is resected and implant inserted into the intramedullary canal. Depending on the needs of the patient and the quality of the surrounding bone, the implant may be inserted directly into the host bone canal (using press-fitting techniques), or the canal enlarged and filled with bone cement prior to implantation, with the bone cement acting as a viscous fixative securing the implant in the desired location (DiMaio, 2002). With either technique, the prosthesis is then capable of load-bearing and maintaining distal articulation, thereby preserving the mobility of the joint and restoring forearm functionality. In addition, a correctly inserted implant will preserve the cosmetic appearance of the wrist.

The first reported use of a distal ulnar prosthesis was in 1972 by Dr. Alfred Swanson (Berg, 1976). He developed a heat-molded silicone rubber implant with a domed head to shield the rough edges of the residual distal ulna, and tapered stem to secure the prosthesis in the intramedullary canal (Sagerman *et al.*, 1992). Though early reports

appeared promising (Swanson, 1973; Berg, 1976), the implant was associated with multiple long-term complications. In particular, implant fracture, tilting, dislocation, bone resorption, and silicone synovitis have plagued this prosthesis design (Jolly et al., 1992; Sagerman et al., 1992; Stanley and Herbert, 1992; Masaoka et al., 2002). As a result of these complications, the Swanson implant is no longer in use.

Overcoming the challenges encountered by the Swanson prosthesis, several innovative new prosthetic designs have been introduced onto the market. There are currently three designs available: the Herbert ulnar head, Advanta uHead, and Wright E-centrix (Figure 1.3). The Herbert ulnar head prosthesis is comprised of a ceramic head and titanium stem with a porous surface designed for a 'contact fit' with the ulna (KLS Martin Group, 2007). The UHead prosthesis is entirely comprised of cobalt chrome with suture holes on the head to allow soft tissue attachment (Small Bone Innovations Inc, 2006). Wright's E-centrix prosthesis is designed with an offset cobalt chrome prosthetic head to improve wear properties and cosmesis, as well as, a roughened portion of the head surface to encourage soft tissue attachment. The implant stem is comprised of biocompatible titanium (King, 2007). As well, both the UHead and E-centrix implants are designed with fluted and tapered stems to enhance rotational stability. Both of the UHead and E-centrix implants were designed for use with bone cement, whereas, originally the Herbert prosthetic was designed solely for uncemented implantation. All three prosthetic designs are available with interchangeable head and stem sizes to account for variations in patient physiology, as well as, optional stem collars to adapt the implant for greater degrees of revision.

At this point, early results have been obtained for all three implant designs and midterm results are available for the Herbert ulnar head implant. Early clinical results for all three implants show positive correlations with pain reduction and improved stability (Van Schoonhoven *et al.*, 2000; Roidis *et al.*, 2007; Willis *et al.*, 2007). Midterm results for the Herbert implant were also satisfactory; however observations of ectopic calcification of the surrounding soft tissues, and cases of implant loosening requiring cementing and revision surgery have occurred (Garcia-Elias, 2007; Herbert and van Schoonhoven, 2007). The short term results for the Advanta uHead were likewise promising; however, instances of implant loosening have been reported, requiring revision surgery to cement the implant thereby ensuring stronger fixation (Cooney III and Berger, 2005). Due to the limited availability of clinical data and long-term studies it is not yet known how the designs of these three implants will relate to their acceptance; however, it appears that distal ulnar arthroplasty is likely to become the future standard of care (Ozer and Scheker, 2006).

1.3.1 Bone Cement

Bone cement has a long history of use in arthroplasty to ensure proper implant fixation. Dating back to 1891, Dr. Gluck was the first surgeon to experiment with copper, amalgam, plaster of paris, and stone kit bone cements (Ritt *et al.*, 1994). In the 1950's, Smith progressed from Gluck's original work, initiating the use of poly(methyl methacrylate) (PMMA) for use in arthroplasty. By the 1960's, Charnley was using PMMA in the fixation of prostheses to the femoral shaft during hip replacement surgery (Charnley, 1960; DiMaio, 2002).



Figure 1.3: Commercially available distal ulnar head implants

There are currently three distal ulnar head implants commercially available: **(A)** Herbert ulnar head implant by KLS Martin (www.klsmartin.com); **(B)** Advanta uHead prosthesis (www.totalsmallbone.com); and **(C)** Wright E-centrix implant (www.wmt.com).

As a result of this initial work, poly(methyl methacrylate) has now become established as the most common method of fixation in joint replacement surgeries (Lewis, 1997; Sugino *et al.*, 2008).

PMMA is comprised of two components, a base powder containing poly(methyl methacrylate), and a liquid containing methylmethacrylate (MMA) monomer. Upon combining the components, an exothermic reaction occurs creating a viscous mixture that cures to produce homologous chains of repeating methylmethacrylate subunits (DiMaio, 2002). In surgery, the fluidity of the cement enables it to be injected into the intramedullary canal prior to implant insertion, such that when cured it forms a non-resorbable cement mantle that stabilizes and secures the implant.

The cement fluidity is critical to proper mantle development; however, this property is influenced by multiple factors. The powder to liquid ratio is carefully formulated such that under ideal conditions ($23^{\circ}\text{C} \pm 1^{\circ}\text{C}$, $50\% \pm 10\%$ relative humidity) all brands of bone cement have a maximum dough time of 5 min, and settling time between 5 and 15 min (Ginebra *et al.*, 2002). Throughout the working period the cement viscosity is not constant, with a pronounced increase in viscosity over time as the polymerization reaction progresses. However, due to the pseudoplastic nature of PMMA, the viscosity of the mixture may be temporarily decreased with an increase in shear rate (*e.g.* using a syringe to quickly inject the cement) (Lewis, 1997).

The handling period of bone cement is also highly susceptible to variations in temperature and mixing method. Decreasing the temperature of the liquid and powder components prior to mixing, through chilling of the cement to approximately 4°C , will

slow the polymerization reaction and extend the workability period (Lidgren *et al.*, 1987). Likewise, vacuum mixing has been shown to increase the workability period by up to one minute (Lidgren *et al.*, 1987; Ginebra *et al.*, 2002). The polymerization reaction of the cement is also susceptible to changes in environmental temperature and humidity, where increasing either factor will shorten the working period (Haas *et al.*, 1975). Due to the influence of all such factors on the viscosity of PMMA bone cement, it is not possible to establish a fixed timeframe during which the material will remain viscous; however, according to Lewis (1997), the typical working period is 3-6 min from the start of mixing.

There are approximately 70 commercial bone cements currently marketed to the medical community. The primary difference between formulations is the molecular weight of the pre-polymer PMMA, the ratio of PMMA to MMA, or the inclusion of additives. Additives are often inserted to increase the polymerization reaction rate, act as a radiopacifier, or provide colorant to simplify *in vivo* identification. Antibiotics or antimicrobial agents may also be added to reduce incidence of postoperative infection (Sanjukta, 2008). With or without the inclusion of these additives, all bone cements must meet ASTM biocompatibility and physical performance standards before receiving approval for commercial use (ASTM, 2010a, 2010b).

1.3.2 Implant Loosening and Debonding

There is clear literary evidence that cemented implants perform satisfactory for elderly patients or those with reduced activity levels (Levy *et al.*, 2000; Ranawat *et al.*, 2004; Rasquinha and Ranawat, 2004). In patients with higher activity levels, concerns have

been raised regarding aseptic loosening and debonding of cemented implants. Implant loosening is defined as motion, beginning on the microscopic scale, of the implant relative to the surrounding cement and/or bone. Implant debonding is believed to occur with the deterioration of the intermolecular interactions (specific adhesion) between the cement and implant, which some believe occurs in all prosthesis (Ahmed *et al.*, 1984). When this adhesive bond is broken (*i.e.*, debonding) the effect on implant load transfer and the progression of loosening is currently unknown; however, both implant loosening and debonding have been associated with implant failure (Mann *et al.*, 1991; Verdonschot and Huiskes, 1996; Garcia-Elias, 2002; Nuño and Avanzolini, 2002; Lennon, 2003; Cooney III and Berger, 2005; Willis *et al.*, 2007).

The exact cause of implant loosening is not well known; however, based on implant retrievals, several hypotheses have been developed (McGee *et al.*, 2000; Sundfeldt *et al.*, 2006). Loosening has been associated with implant malpositioning, the selection of an undersized implant, or over reaming of the intramedullary canal (Herbert and van Schoonhoven, 2007). For the cemented stems, it has also been hypothesized that failure of the implant-cement bond (Verdonschot and Huiskes, 1996) or mechanical failure of the cement due to crack propagation initiating at the cement-stem interface may be the causative factor (Jasty *et al.*, 1991). Stems may also loosen if the surrounding bone is removed, by the phenomenon known as “stress shielding”.

1.3.3 Stress Shielding

Stress shielding is the reduction in bone density surrounding an orthopaedic implant due to the removal of anatomical joint loading (*i.e.*, load is borne by the implant, and

thus bone loading is reduced). This ultimately acts as a causative factor in the loosening of the implant (Maloney *et al.*, 1989). This reduction in force is a result of the implant stiffness being greater than that of the surrounding bone, thereby altering the load distribution to the bone. However, it is unclear how the level of bonding at the cement-implant interface may affect the stress shielding phenomenon. That is, how the magnitude and type of load reaching the bone may be influenced by debonding of the implant from its cement mantle, which some argue occurs for all cemented implants within their lifespan (Verdonschot and Huiskes, 1998).

1.4 Post Arthroplasty Strain Measurement

Changes in stress distribution to the structures surrounding cemented implants are thought to occur as a result of debonding and implant loosening. Since it is not possible to directly measure stress, strain gauges applied to both the cement and bone surrounding the implant provide one quantitative method for determining alterations in stress/strain patterns.

1.4.1 Piezoresistive foil gauge overview

Piezoresistive foil gauges or strain gauges are comprised of a grid of aluminum or stainless steel wires encapsulated between two sheets of polyamide or epoxy film (Figure 1.4). The wire grid is oriented in a single direction such that applied strain will stretch the grid along its length. As the wire deforms, a change in resistance occurs in accordance with Equation 1.

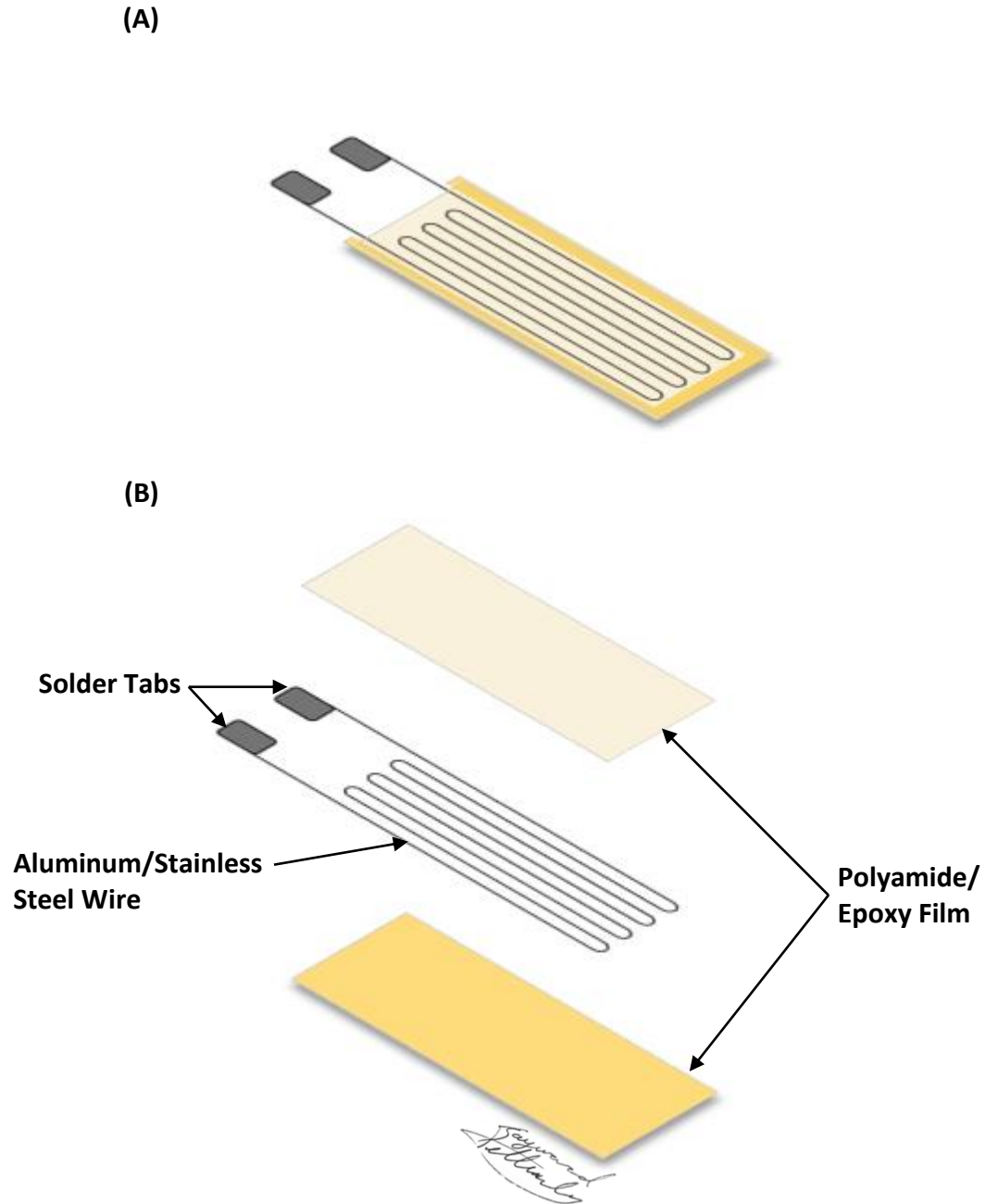


Figure 1.4: Uniaxial strain gauge

Commercially available gauges are comprised of two thin layers of polyamide or epoxy film surrounding a metal wire. Displayed are the (A) isometric and (B) assembly views of a uniaxial strain gauge.

$$R = \frac{(\rho_{\text{resistivity}}L)}{A} \quad \text{Equation 1}$$

Where: $\rho_{\text{resistivity}}$ = Resistivity of the wire
 L = Length of the conductor
 A = Cross-sectional area of the wire

As the wire stretches, its length (L) increases and cross-sectional area (A) decreases, resulting in an increase in resistance (R) that is proportional to the change in strain. Strain gauges are also sensitive to changes in temperature and pressure, as such they are not recommended for applications where these variables change during the desired measurement period.

Uniaxial or multiaxial strain gauges are commercially available. Uniaxial gauges allow for one directional strain measurement; however, in studies involving axial and shear strain, or requiring the calculation of the principal strain, triaxial gauges are preferred. Standard triaxial rosettes are composed of three wire grids oriented in a 0-45-90° pattern. Using strain obtained from a triaxial gauge as displayed in Figure 1.5, and the formulae provided in Equation 2 and Equation 3, the respective maximum (ϵ_{max}) and minimum (ϵ_{min}) principal strains may be determined for a given location as:

$$\epsilon_{\text{max}} = \frac{(\epsilon_A + \epsilon_C)}{2} + \left(\frac{1}{\sqrt{2}}\right) \sqrt{(\epsilon_A - \epsilon_B)^2 + (\epsilon_B - \epsilon_C)^2} \quad \text{Equation 2}$$

$$\epsilon_{\text{min}} = \frac{(\epsilon_A + \epsilon_C)}{2} - \left(\frac{1}{\sqrt{2}}\right) \sqrt{(\epsilon_A - \epsilon_B)^2 + (\epsilon_B - \epsilon_C)^2} \quad \text{Equation 3}$$

Where: ϵ = Strain

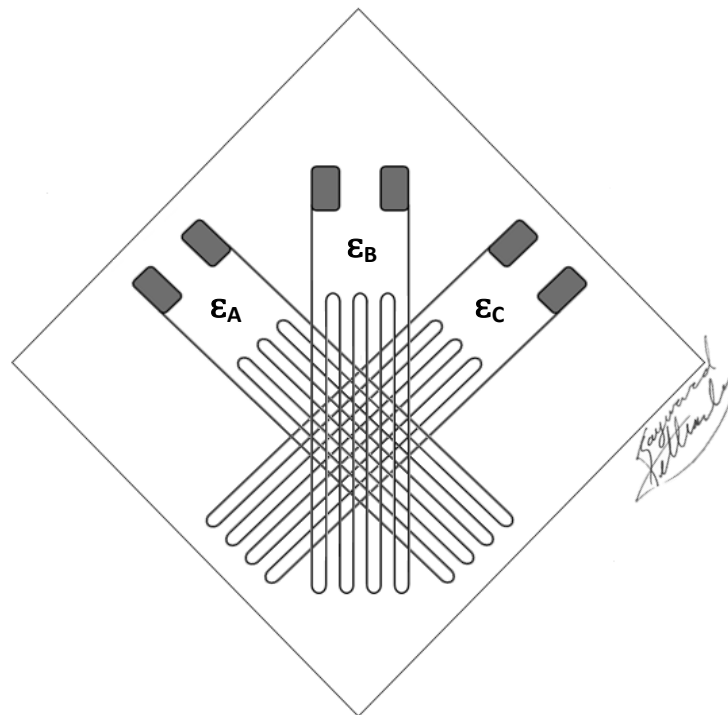


Figure 1.5: Triaxial gauge orientation

Standard triaxial rosettes are composed of three uniaxial strain gauges oriented in a 0-45-90° pattern. Utilizing the strain response of all three gauges principal strain may be calculated.

1.4.2 Wheatstone Bridges

Wheatstone bridges are used in conjunction with strain gauges to isolate and amplify the desired signal while reducing any undesirable components. Each Wheatstone bridge is comprised of four arms, with a resistor on each arm, and allows for both the application of an input voltage (V_{in}) and measurement of an output voltage (V_{out}) (Figure 1.6). When the resistances are equal and the bridge balanced, an output voltage of zero will be recorded. Strain gauges may be substituted for one, two or four of the Wheatstone bridge's resistors. When the gauges are incorporated into the circuit, changes in resistance that result from the change in the length of the wire in the gauge will impact the output voltage; therefore, in this scenario voltage changes are proportional to changes in strain.

1.4.3 Strain Gauge Embedment

While applying a strain gauge to an external surface is a well-known and relatively straight-forward procedure, challenges can arise when attempting to embed them within a material. Embedded strain gauges have been utilized since the early 1960's to measure the strains within artificial solids. The original technique was pioneered by Brasier and Dove for the insertion of gauges without altering the strain pattern within the material (Brasier and Dove, 1961; Dove *et al.*, 1962). The validity of this method in measuring both static and dynamic strains was established by Serdengecti *et al.* and its functionality in measuring strains in both bending and tension was confirmed by Epelle (Serdengecti *et al.*, 1962; Epelle, 1975).

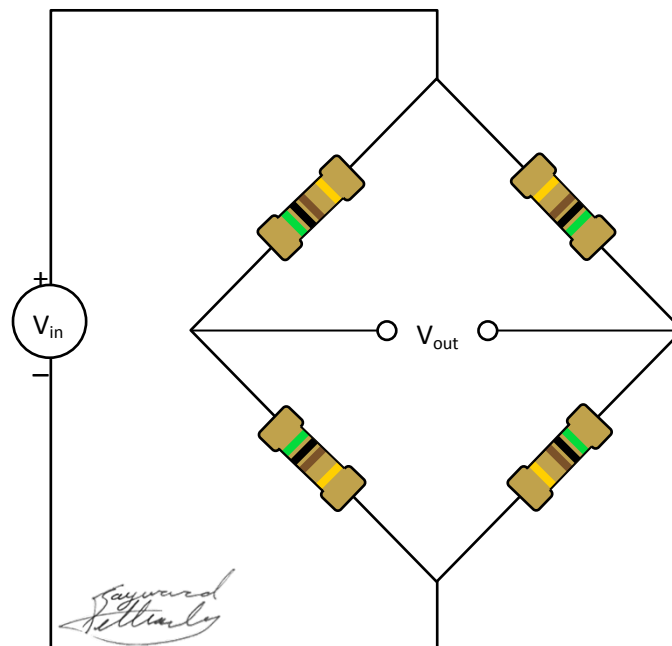


Figure 1.6: Wheatstone bridge circuit

Wheatstone bridges are frequently used in conjunction with strain gauges to accentuate desired signals and attenuate those that are undesired. They are comprised of four arms, with a resistor or gauge inserted in each arm. The circuit allows for both the application of an input (or excitation) voltage (V_{in}) and measurement of an output voltage (V_{out}) (which is related to the measured strain).

Since then, multiple methods of technique optimization and error reduction have been reported in the literature (Little, 1982; Little *et al.*, 1990; Ajovalasit, 2005).

Two primary methods of strain gauge embedment have emerged. The first method uses a three-dimensional multi-gauge construct to measure all load components in a given space. This technique was pioneered by Babut and Brant, who developed a linked nine-gauge device utilizing vibrating-wire strain gauges, and tested their apparatus within a cement construct (Babut and Brandt, 1977). Little and O'Keefe along with Baker and Dove offered an alternative designs, by creating three dimensional strain rosettes, comprised of three gauges mounted on a carrier (Baker and Dove, 1963; Little, 1984; Little and O'Keefe, 1989). Both sensors were determined to have a high degree of accuracy; however, they are limited in application due to the large sensor size and are rarely used in medical applications (Babut and Brandt, 1977; Little and O'Keefe, 1989).

1.4.3.1 Methods of Embedment in Bone Cement

The application of gauge embedment techniques to examine strains in bone cement has been limited. Initial embedment techniques affixed a strain gauge onto a PMMA wafer that was then inserted into a bone cement cantilever beam. This technique showed a positive experimental to theoretical agreement of greater than 89%, but was not representative of the geometric conditions found in a cement mantle (Draganich *et al.*, 1982). Due to these positive results, the technique was further developed for use in comparing the strains within the cement mantle of a femoral implant during dynamic and static loading (Davey *et al.*, 1993; O'Connor *et al.*, 1996; Estok *et al.*, 1997). Though the results appeared viable, in the experimental procedure the gauges were grouped

into a cluster at the superior end of the cement mantle and aligned vertically along the medial and lateral mantle segments with the embedded lead wires bound together. This close vertical gauge alignment and method for handling wires within the region under study has been shown to cause local reinforcement in the cement and reduced strain response (Ajovalasit, 2005).

Fisher *et al.* modified this method of gauge embedment, rather than affixing the gauge on a wafer, the implant stem was coated with a thin layer of bone cement and the gauges fixed to known locations. The instrumented stem was then implanted into composite femoral replicas for testing. Strong correlations between experimental and theoretical strains were determined for the gauges in PMMA cantilever beams; however, validation of the final testing method was not conducted (Fisher *et al.*, 1997).

Cristofolini and Viceconti cemented 10 localized areas on the proximal portion of 12 hip stems and instrumented each area with a triaxial gauge prior to implanting the gauged stems into composite femurs. During testing, all gauge wires were embedded into grooves along the implant stem, which were then filled with putty and smoothed to maintain stem geometry. The reproducibility and robustness of this application was validated through the repetitive application of loads simulating the heel-strike phase of gait (Cristofolini and Viceconti, 2000). Cristofolini *et al.* also utilized this procedure in the testing of stress shielding in epiphyseal hip prostheses (Cristofolini *et al.*, 2009). However, in both studies, the gauge wires were embedded within the implant stem potentially impacting the stem-cement interface, thereby altering the load transfer from the stem to the cement in the affected areas.

Despite the limitations inherent in strain gauge embedment, the aforementioned studies have validated its use in measuring strains within the cement mantle for femoral implants. However, further research is needed to determine the optimal method of triaxial gauge embedment and test its applicability to upper limb implants, in which the smaller size of the host bone increases the challenge.

1.5 Finite Element Analysis (FEA)

The Finite Element Method was developed in the 1940's (Logan, 2002), and was introduced to the field of orthopedic biomechanics by Brekelmans *et al.* in 1972. From its humble beginnings as an analysis program using a lattice of one-dimensional elements to solve for stresses in continuous solids (McHenry, 1943), it has grown into a powerful tool through which complex biomechanical problems may be addressed. The suitability of FEA for use in biomechanical problems may be attributed to its functionality in analyzing complex shapes, materials and loading patterns to determine the resultant stresses and strains (Huiskes and Chao, 1983). Such data may be determined not only at discrete points, as can be accomplished experimentally, but also throughout the specimen. As well, a single FEA model may be examined under multiple loading conditions or in a variety of scenarios, a situation that would be experimentally impractical due to cost constraints, restrictions in cadaver availability, and time.

Of the commercially available modeling softwares, the Abaqus[®] program (Simulia, Providence, Rhode Island, USA) is one of the most commonly used for biomedical applications. This software was originally developed in 1978 by David Hibbitt and Bengt

Karlsson to study mechanical restraints in nuclear reactor cores (Webb, 2009). It has since developed into a robust software package capable of integrating geometry based and imported meshes, and modeling linear and nonlinear materials and contact properties (Simulia, 2012).

1.5.1 Finite Element Components

Finite element analysis is used to determine mechanical stresses of a loaded object in complex scenarios where it would not be feasible to complete the calculations manually using theoretical equations. Such scenarios include instances where the object has complex material properties or geometry, indeterminate structures, large deformations, or in when complex loads are applied.

The premise behind the method is to decentralize the part into smaller segments called finite elements, with each element linked at nodes, boundary lines, or shared interfaces. Simple equations (Equation 4) may then be used to describe the relationship of force vs. deformation for each element, normally at the node locations:

$$F = ku \quad \text{Equation 4}$$

Where: F = Applied forces
 k = Element stiffness matrix
 u = Nodal displacements

Elements are fit to the object's surface to form a mesh, with the quality of the resultant mesh highly dependent on the element selection, with regards to size and type. Elements used to model 3-D solids are generally based on tetrahedral or hexahedral structures, which may be further divided into linear or quadratic forms (Figure 1.7).

Quadratic elements (with mid-edge nodes) are able to model curved surfaces and generate a more accurate result, but also require greater computer power. Despite the computational restrictions, quadratic elements are recommended for utilization in biomechanical modeling of complex skeletal components, as linear elements have been associated with poor performance and failure to adequately predict stress in regions with large gradients (Polgar *et al.*, 2001). Previous studies have also shown that quadratic tetrahedral elements are capable of producing accurate results when modeling biological structures (Au *et al.*, 2005; Ramos and Simões, 2006).

1.5.2 Model Parameters

To develop a finite element model, the geometry of the object being analyzed must first be defined. For complex anatomical subjects, such as a biological specimen, three dimensional imaging data is often used (Taddei *et al.*, 2007; Yosibash *et al.*, 2007). A subject specific finite element model may be developed by taking a computer tomography (CT) scan of the specimen. Once the scan is obtained, the bone to be analysed is isolated from the extraneous imaging data through alteration of the image's attenuation levels, where different materials (with their associated properties) may be identified in different attenuation ranges. Once complete, a mesh is applied (Section 1.5.1).

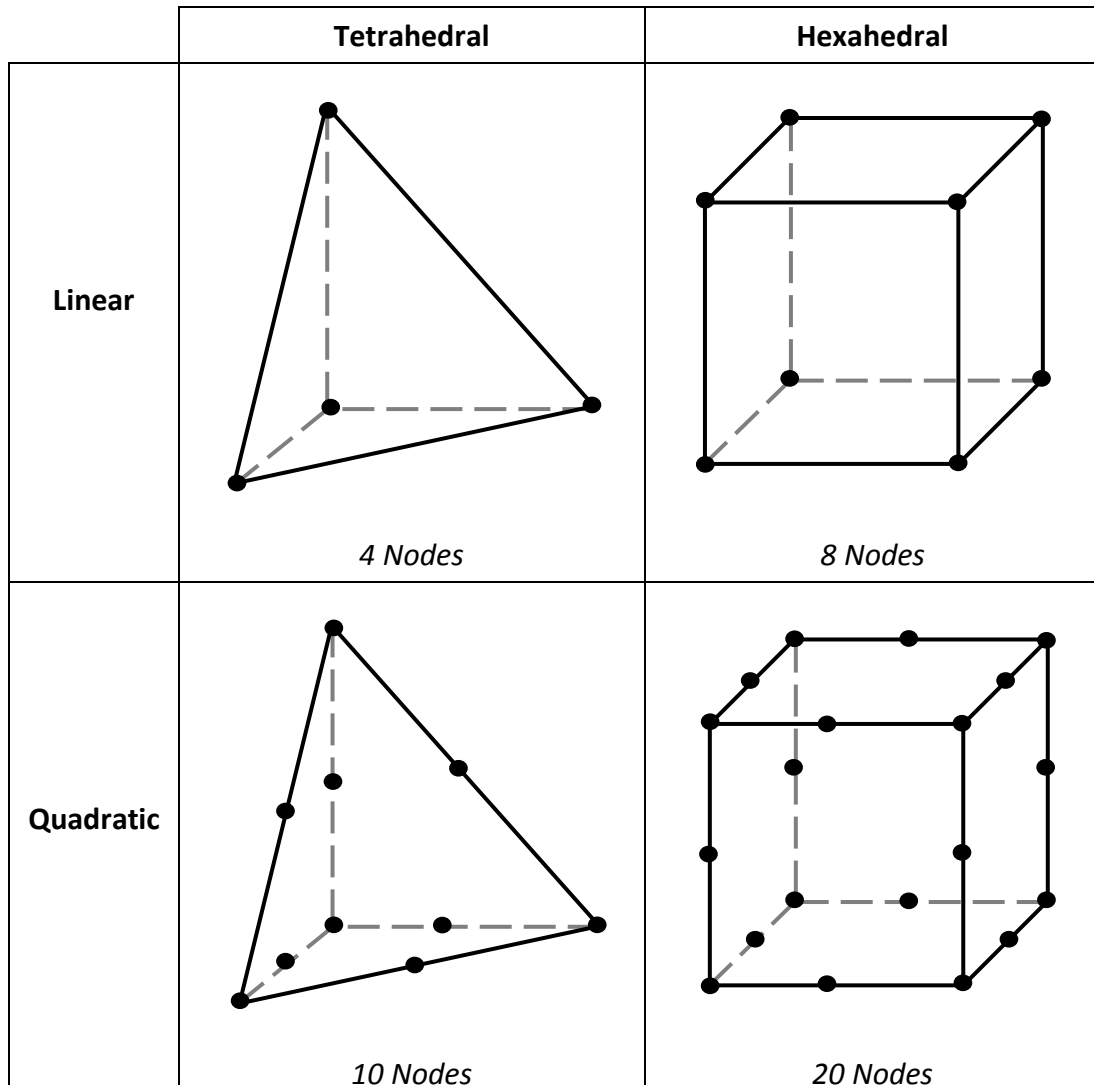


Figure 1.7: Elements options with associated nodes

Linear and quadratic tetrahedral and hexahedral elements utilized in finite element analysis are displayed with their respective nodal numbers.

The accuracy of the model is dependent on the valid representation of not only the geometry but also the material properties of the specimen. As such, the properties of known materials (*i.e.*, titanium) may be obtained from the literature; however, inhomogeneous material properties are unique to the specimen and, therefore, cannot be determined in this manner. As with specimen geometry, CT images may be utilized to determine material properties, since the Hounsfield units displayed on the CT are linearly correlated to the density of skeletal tissue (Taddei *et al.*, 2004). As the density of bone is related to its elastic modulus, material property-density relationships may be applied to the CT scans in order to assign inhomogeneous material properties to the bone model (Austman *et al.*, 2009).

A fully developed finite element model may be tested in a variety of scenarios and relevant strain data acquired post-processing. This may be accomplished through the selection and application of appropriate load and constraint data, such that the forces being applied are anatomically relevant. During processing, the resultant FEA will solve for nodal displacement and calculate the element stress based on these values. However, before any finite element results may be used, they must first be validated against experimentally obtained measures (*e.g.* strain gauges). Without validation, use of any model must be questioned.

1.6 Study Rationale

Surgical advancements have enabled the treatment of severely damaged or diseased distal ulnar joints through the removal of the damaged bone and insertion of a joint replacement component. However, the long-term functionality of these implants is currently unknown, and the potential for implant loosening must be considered. In the case of cemented implants, failure due to implant loosening may be instigated by excessive strain resulting in mechanical failure of the cement (Jasty *et al.*, 1991), or as a result of stress shielding (Maloney *et al.*, 1989). However, it is currently unknown how the level of bonding at the cement-implant interface may affect the onset of loosening or the stress shielding phenomenon. The purpose of the proposed research is to examine torsional and bending strains within the cement mantle, as well as in the surrounding bone, following distal ulnar arthroplasty as a function of bonded versus debonded interface conditions. Furthermore, a finite element model capable of analyzing bending strain with a variety of implant-cement interface conditions is developed. The ultimate goal of this research is to enhance the understanding of the role of the implant-cement interface conditions on strains in the cement mantle and their impact on stress shielding. The desire is that the information garnered through this research may then be used to optimize the design of distal ulnar implants, thereby reducing the need for replacement through costly and painful revision surgeries.

1.7 Objectives and Hypotheses

The objectives of this thesis are as follows:

1. to develop a strain gauge embedment methodology that will not compromise gauge functionality within the confines of the distal ulna,
2. to experimentally investigate the effect of distal ulnar implant-cement debonding on cortical bone strains and strains within the cement mantle as a function of loading conditions; and,
3. to expand the validation of a previously developed finite element model of the distal ulna to include cement strains, and determine if the debonded cement-implant interface may be modeled via a Coulomb frictional interaction.

The corresponding hypotheses were:

1. Bonded strain gauge embedment will be more functional than wafer embedment methods.
2. Debonding at the implant-cement interface will result in an increase in both cement and bone strains surrounding the implant compared to a bonded interface, while strains proximal to the implant will not change.
3. FEA results will agree with the experimental measurements of strain both within the cement mantle and on the surrounding bone surface, thereby indicating that cement-stem debonding may be accurately represented with a Coulomb frictional interaction.

1.8 Thesis Outline

This thesis was written in the integrated article format. With each of the previously mentioned objectives and hypotheses (Section 1.7) corresponding to a chapter in the thesis. Where, Chapter 2 describes a strain gauge embedment methodology that allows the measurement of strains within the constrained cement mantle surrounding an implant stem, without the use of an adhesive. Chapter 3 outlines an experimental study which examined the effect of implant-cement debonding on strains both within the cement mantle and on the cortical bone surface. Chapter 4 investigates the expansion of a previously developed finite element model of distal ulnar arthroplasty, to include cement strains and multiple cement-stem interface conditions. Chapter 5 summarizes the conclusions of this thesis, its overall significance, as well as potential future work related to these studies.

1.9 References

- ASTM, 2010a. Standard test method for constant amplitude of force controlled fatigue testing of acrylic bone cement materials, ASTM International, DOI: 10.1520/F2118-10.
- ASTM, 2010b. Standard specification for acrylic bone cement, ASTM International, DOI: 10.1520/F451-08.
- Ahmed, A.M., Raab, S., Miller, J.E., 1984. Metal/cement interface strength in cemented stem fixation. *Journal of Orthopaedic Research: official publication of the Orthopaedic Research Society* 2, 105–118.
- Ajovalasit, A., 2005. Embedded strain gauges : effect of the stress normal to the grid. *Strain* 95–103.
- Au, A.G., Liggins, A.B., Raso, V.J., Amirfazli, A., 2005. A parametric analysis of fixation post shape in tibial knee prostheses. *Medical Engineering & Physics* 27, 123–134.

- Austman, R.L., Milner, J.S., Holdsworth, D.W., Dunning, C.E., 2009. Development of a customized density–modulus relationship for use in subject-specific finite element models of the ulna. *Proceedings of the Institution of Mechanical Engineers, Part H: Journal of Engineering in Medicine* 223, 787–794.
- Babut, R., Brandt, A.M., 1977. Measurements of internal strains by nine-gauge devices. *Strain* 18–21.
- Baker, W.E., Dove, R.C., 1963. Construction and evaluation of a three-dimensional strain rosette. *Experimental Mechanics* 201–206.
- Bell, M., Hill, R., McMurtry, R., 1985. Ulnar impingement syndrome. *Journal of Bone and Joint Surgery* 67B, 126–129.
- Berg, E., 1976. Indications for and results with a Swanson distal ulnar prosthesis. *Southern Medical Journal* 69, 858–861.
- Brasier, I., Dove, R.C., 1961. Use of electrical-resistance strain elements in three-dimensional stress analysis the stress pattern in the model. *Experimental Mechanics* 186–191.
- Brekelmans, W., Poort, H., Slooff, T., 1972. A new method to analyse the mechanical behaviour of skeletal parts. *Acta Orthopaedica Scandinavica* 43, 301–317.
- Carter, P.B., Stuart, P.R., 2000. The Sauve-Kapandji procedure for post-traumatic disorders of the distal radio-ulnar joint. *The Journal of Bone and Joint Surgery. British Volume* 82, 1013–1018.
- Charnley, J., 1960. Anchorage of the femoral prosthesis to the shaft of the femer. *Journal of Bone and Joint Surgery* 42B, 28–30.
- Chidgey, L., 1995. The distal radioulnar joint: problems and solutions. *The Journal of the American Academy of Orthopaedic Surgeons* 3, 95–109.
- Chun, S., 1993. The ulnar impaction syndrome: Follow-up of ulnar shortening osteomy. *Journal of Hand Surgery* 18A, 46–53.
- Cooney III, W., Berger, R., 2005. Distal radioulnar joint implant arthroplasty. *Journal of the American Society for Surgery of the Hand* 5, 217–231.
- Cooney, W., 1993. Evaluation of chronic wrist pain by arthrography, arthroscopy, and arthrotomy. *Journal of Hand Surgery* 18A, 815–822.
- Cooney, W.P., Dobyns, J.H., Linscheid, R.L., 1980. Complications of colles' fractures. *The Journal of Bone and Joint Surgery. American Volume* 62, 613–619.

- Cristofolini, L., Juszczak, M., Taddei, F., Field, R.E., Rushton, N., Viceconti, M., 2009. Stress shielding and stress concentration of contemporary epiphyseal hip prostheses. *Proceedings of the Institution of Mechanical Engineers, Part H: Journal of Engineering in Medicine* 223, 27–44.
- Cristofolini, L., Viceconti, M., 2000. Development and validation of a technique for strain measurement inside polymethyl methacrylate. *Journal of Strain Analysis* 35, 21–33.
- Darcus, H.D., Salter, N., 1953. The amplitude of pronation and supination with the elbow flexed to a right angle. *Journal of Anatomy* 87, 169–184.
- Darrach, W., 1913. Partial excision of lower shaft of ulna for deformity following Colles's fracture. *Annals of Surgery* 57, 764–765.
- Davey, J.R., O'Connor, D.O., Burke, D.W., Harris, W.H., 1993. Femoral component offset, its effect on strain in bone-cement. *The Journal of Arthroplasty* 8, 23–26.
- DiMaio, F.R., 2002. The science of bone cement: a historical review. *Orthopedics* 25, 1399–1407.
- Dove, R.C., Brasier, R.I., Baker, W.E., 1962. Selection of gages for strain measurement at interior points. *Experimental Mechanics* 189–190.
- Draganich, L.F., Andriacchi, T.P., Galante, J.O., 1982. A technique for embedding strain gages within curing bone cement. *Journal of Biomechanics* 15, 789–790.
- Ekenstam, F., 1992. Anatomy of the distal radioulnar joint. *Clinical Orthopaedics and Related Research* 275, 14–18.
- Ekenstam, F., Hagert, C.G., 1985. Anatomical studies on the geometry and stability of the distal radio ulnar joint. *Scandinavian Journal of Plastic and Reconstructive Surgery* 19, 17–25.
- Ekenstam, F., Palmer, A., Glisson, R., 1984. The load on the radius and ulna in different positions of the wrist and forearm. *Acta Orthopaedica Scandinavica* 55, 363–365.
- Epelle, B., 1975. Measurement of strains in plain and perforated epoxy models by means of embedded strain gauges. *Strain* 17–22.
- Estok, D.M., Orr, T.E., Harris, W.H., 1997. Factors affecting cement strains near the tip of a cemented femoral component. *The Journal of Arthroplasty* 12, 40–48.
- Fisher, D., Tsang, A., Paydar, N., Milionis, S., Turner, C., 1997. Cement-mantle thickness affects cement strains in total hip replacement. *J. Biomechanics* 30, 1173–1177.

- Gaebler, C., McQueen, M.M., 2003. Ulnar procedures for post-traumatic disorders of the distal radioulnar joint. *Injury: International Journal of the Care of the Injured* 34, 47–59.
- Garcia-Elias, M., 2002. Failed ulnar head resection: prevention and treatment. *The Journal of Hand Surgery: Journal of the British Society for Surgery of the Hand* 27, 470–480.
- Garcia-Elias, M., 2007. Eclipse: partial ulnar head replacement for the isolated distal radio-ulnar joint arthrosis. *Techniques in Hand & Upper Extremity Surgery* 11, 121–128.
- George, M.S., Kiefhaber, T.R., Stern, P.J., 2004. The Sauvé-Kapandji procedure and the Darrach procedure for distal radio-ulnar joint dysfunction after Colles' fracture. *Journal of Hand Surgery (Br)* 29B, 608–613.
- Ginebra, M.-P., Gil, F.-J., Planell, J.-A., 2002. Acrylic bone cements: influence of time and environment on physical properties., in: Barbucci, R. (Ed.), *Integrated Biomaterials Science*. New York, pp. 569–588.
- Goncalves, D., 1974. Correction of disorders of the distal radio-ulnar joint by artificial pseudarthrosis of the ulna. *The Journal of Bone and Joint Surgery* 56B, 462–464.
- Gordon, K.D., Kedgley, A.E., Ferreira, L.M., King, G.J.W., Johnson, J. a, 2006. Design and implementation of an instrumented ulnar head prosthesis to measure loads in vitro. *Journal of Biomechanics* 39, 1335–1341.
- Haas, S., Brauer, G., Dickson, G., 1975. A characterization of polymethylmethacrylate bone cement. *The Journal of Bone and Joint Surgery* 57A, 380–391.
- Herbert, T.J., van Schoonhoven, J., 2007. Ulnar head replacement. *Techniques in Hand & Upper Extremity Surgery* 11, 98–108.
- Huiskes, R., Chao, E., 1983. A survey of finite element analysis in orthopedic biomechanics: the first decade. *Journal of Biomechanics* 16, 385–409.
- Jasty, M., Maloney, W., Bragdon, C., O'Connor, D., Haire, T., Harris, W., 1991. The initiation of failure in cemented femoral components of hip arthroplasties. *Society of Bone and Joint Surgery (Br)* 73B, 551–558.
- Jolly, S.L., Ferlic, D.C., Clayton, M.L., Dennis, D.A., Stringer, E.A., 1992. Swanson silicone arthroplasty of the wrist in rheumatoid arthritis: A long-term follow-up. *The Journal of Hand Surgery* 17, 142–149.
- King, G., 2007. E-CENTRIX ulnar head replacement surgical technique [Brochure]. Wright Medical Technology Inc.

- KLS Martin Group, 2007. Herbert ulnar head prosthesis [Brochure]. KLS Martin Group
- Lennon, A., 2003. The relationship between cement fatigue damage and implant surface finish in proximal femoral prostheses. *Medical Engineering & Physics* 25, 833–841.
- Levy, B., Berry, D., Pagnano, M., 2000. Long-term survivorship of cemented all-polyethylene acetabular components in patients >75 years of age. *The Journal of Arthroplasty* 15, 461–467.
- Lewis, G., 1997. Properties of acrylic bone cement: state of the art review. *Journal of Biomedical Materials Research* 38, 155–182.
- Lidgren, L., Bodelind, B., Möller, J., 1987. Bone cement improved by vacuum mixing and chilling. *Acta Orthopaedica Scandinavica* 58, 27–32.
- Little, E.G., 1982. Effects of self heating when using a continuous bridge voltage for strain gauging epoxy models. *Strain* 131–135.
- Little, E.G., 1984. Embedded strain gaging of plastic models methods of embedding strain gages. *Experimental Techniques* 19–22.
- Little, E.G., O’Keefe, D., 1989. An experimental technique for the investigation of three-dimensional stress in bone cement underlying a tibial plateau. *Proc Instn Mech Engrs* 203, 35–41.
- Little, E.G., Tocher, D., Donnell, P.O., 1990. Strain gauge reinforcement of plastics. *Strain* 91–98.
- Logan, D.L., 2002. *A First Course in the Finite Element Method*, Third. ed, *A First Course in the Finite Element Method: Third Method*. Thompson Learning, Pacific Grove.
- Loh, Y.C., Abbeele, K.V.A.N.D.E.N., Stanley, J.K., Trail, I.A., 1999. The Results of ulnar shortening for ulnar impaction syndrome. *Journal of Hand Surgery (British and European Volume)* 24B, 316–320.
- Maloney, W.J., Jasty, M., Burke, D.W., O’Connor, D.O., Zalenski, E.B., Bragdon, C., Harris, W.H., 1989. Biomechanical and histologic investigation of cemented total hip arthroplasties. *Clinical Orthopaedics and Related Research* 129–140.
- Mann, K.A., Bartel, D.L., Wright, T.M., Ingraffea, a R., 1991. Mechanical characteristics of the stem-cement interface. *Journal of Orthopaedic Research : official publication of the Orthopaedic Research Society* 9, 798–808.
- Masaoka, S., Longworth, S., Werner, F., Short, W., Green, J., 2002. Biomechanical Analysis of Two Ulnar Head Prostheses. *Journal of Hand Surgery* 27A, 845–853.

- McGee, M.A., Howie, D.W., Costi, K., Haynes, D.R., Wildenauer, C.I., Percy, M.J., Mclean, J.D., 2000. Implant retrieval studies of the wear and loosening of prosthetic joints : a review. *Society* 158–165.
- McHenry, D., 1943. A lattice analogy for the solution of stress problems. *Journal of Applied Mechanics* 21, 59–82.
- Nakamura, R., Tsunoda, K., Watanabe, K., Horii, E., Miura, T., 1992. The Sauvé-Kapandji procedure for chronic dislocation of the distal radio-ulnar joint with destruction of the articular surface. *The Journal of Hand Surgery: Journal of the British Society for Surgery of the Hand* 17, 127–132.
- Nuño, N., Avanzolini, G., 2002. Residual stresses at the stem-cement interface of an idealized cemented hip stem. *Journal of Biomechanics* 35, 849–852.
- Ozer, K., Scheker, L.R., 2006. Distal radioulnar joint problems and treatment options. *Orthopedics* 29, 38–49.
- O'Connor, D.O., Burke, D.W., Jasty, M., Sedlacek, R.C., Harris, W.H., 1996. In vitro measurement of strain in the bone cement surrounding the femoral component of total hip replacements during simulated gait and stair-climbing. *Journal of Orthopaedic Research : Official Publication of the Orthopaedic Research Society* 14, 769–777.
- Patrick, J., 1946. A study of supination and pronation, with especial reference to the treatment of forearm fractures. *Journal of Bone and Joint Surgery* 28, 737–748.
- Peterson, C., Maki, S., Wood, M., 1995. Clinical results of the one-bone forearm. *Journal of Hand Surgery* 20A, 609–618.
- Plamer, A.K., Werner, F.W., 1983. Biomechanics of the distal radioulnar joint. *Clinical Orthopaedics and Related Research* 187, 26–35.
- Polgar, K., Viceconti, M., Connor, J.J., 2001. A comparison between automatically generated linear and parabolic tetrahedra when used to mesh a human femur. *Proceedings of the Institution of Mechanical Engineers, Part H: Journal of Engineering in Medicine* 215, 85–94.
- Ramos, A., Simões, J. a, 2006. Tetrahedral versus hexahedral finite elements in numerical modelling of the proximal femur. *Medical Engineering & Physics* 28, 916–924.
- Ranawat, C.S., Ranawat, A.S., Rasquinha, V.J., 2004. Mastering the art of cemented femoral stem fixation. *The Journal of Arthroplasty* 19, 85–91.

- Rasquinha, V.J., Ranawat, C.S., 2004. Durability of the cemented femoral stem in patients. *Clinical Orthopaedics* 115–123.
- Ray, R.D., Johnson, R.J., Jameson, R.M., 1951. Rotation of the forearm. *Journal of Bone and Joint Surgery* 33-A, 993–996.
- Ritt, M., Stuart, P., Naggar, L., Beckenbaugh, R., 1994. The early history of arthroplasty of the wrist. *Journal of Hand Surgery (Br)* 19B, 778–782.
- Roidis, N.T., Gougoulas, N.E., Liakou, P.D., Malizos, K.N., 2007. Distal ulnar implant arthroplasty as a definitive treatment of a recurrent giant-cell tumor. *The Journal of Hand Surgery* 32, 1262–1266.
- Roysam, G., 1993. The distal radio-ulnar joint in Colles fractures. *Journal of Bone and Joint Surgery [Br]* 75B, 58–60.
- Sagerman, S., Seileriii, J., Fleming, L., Lockerman, E., 1992. Silicone rubber distal ulnar replacement arthroplasty. *The Journal of Hand Surgery: Journal of the British Society for Surgery of the Hand* 17, 689–693.
- Salter, N., Darcus, H.D., 1953. The amplitude of forearm and of humeral rotation. *Journal of Anatomy* 87, 407–418.
- Sanjukta, D. (Ed.), 2008. *Orthopedic bone cements*. Woodhead Publishing Ltd, Cambridge, England.
- Sauerbier, M., 2002. The dynamic radioulnar convergence of the Darrach procedure and the ulnar head hemiresection interposition arthroplasty: a biomechanical study. *The Journal of Hand Surgery: Journal of the British Society for Surgery of the Hand* 27, 307–316.
- Scheker, L.R., Severo, A., 2001. Ulnar shortening for the treatment of early post-traumatic osteoarthritis at the distal radioulnar joint. *Journal of Hand Surgery* 26, 41–44.
- Van Schoonhoven, J., Fernandez, D.L., Bowers, W.H., Herbert, T.J., 2000. Salvage of failed resection arthroplasties of the distal radioulnar joint using a new ulnar head prosthesis. *The Journal of Hand Surgery* 25, 438–446.
- Serdengecti, S., Hendrickson, J.A., Skjelbreia, L., 1962. Strain-gage technique for measuring internal strains in artificial solids. *Experimental Mechanics* 129–136.
- Shaaban, H., Pereira, C., Williams, R., Lees, V.C., 2008. The effect of elbow position on the range of supination and pronation of the forearm. *The Journal of Hand Surgery (European)* 33, 3–8.

- Simulia, 2012. Abaqus® Unified FEA [Brochure]. Dassault Systems
- Small Bone Innovations Inc, 2006. uHead™ Ulnar Implant System [Brochure]. Small Bone Innovations Inc.
- Stanley, D., Herbert, T., 1992. The swanson ulnar head prosthesis for post-traumatic disorders of the distal radio-ulnar joint. *The Journal of Hand Surgery: Journal of the British Society for Surgery of the Hand* 17, 682–688.
- Sugino, A., Ohtsuki, C., Miyazaki, T., 2008. In vivo response of bioactive PMMA-based bone cement modified with alkoxy silane and calcium acetate. *Journal of biomaterials applications* 23, 213–228.
- Sundfeldt, M., Carlsson, L.V., Johansson, C.B., Thomsen, P., Gretzer, C., 2006. Aseptic loosening, not only a question of wear: a review of different theories. *Acta Orthopaedica* 77, 177–197.
- Swanson, A., 1973. Implant arthroplasty for disabilities of the distal radioulnar joint. *Orthopedic Clinical Research (North American)* 4, 373–381.
- Taddei, F., Pancanti, A., Viceconti, M., 2004. An improved method for the automatic mapping of computed tomography numbers onto finite element models. *Medical Engineering & Physics* 26, 61–69.
- Taddei, F., Schileo, E., Helgason, B., Cristofolini, L., Viceconti, M., 2007. The material mapping strategy influences the accuracy of CT-based finite element models of bones: an evaluation against experimental measurements. *Medical engineering & physics* 29, 973–979.
- Trieb, K., 2008. Treatment of the wrist in rheumatoid arthritis. *The Journal of Hand Surgery* 33, 113–123.
- Verdonschot, N., Huiskes, R., 1996. Mechanical effects of stem cement interface characteristics in total hip replacement. *Clinical Orthopaedics and Related Research* 329, 326–336.
- Verdonschot, N., Huiskes, R., 1998. Surface roughness of debonded straight-tapered stems in cemented THA reduces subsidence but not cement damage. *Biomaterials* 19, 1773–1779.
- Vincent, K., Szabo, R., Agee, J., 1993. The Sauve-Kapandji procedure for reconstruction of the rheumatoid distal radioulnar joint. *Journal of Hand Surgery* 18A, 978–983.
- Webb, T., 2009. SIMULIA : A brief history [WWW Document]. Retrieved July 30, 2012, from Rhode Island Nexus. URL <http://rinexus.com/blog/2009/09/simulia>

- Weiler, P., Bogoch, E., 1995. Kinematics of the distal radioulnar joint in rheumatoid arthritis: an in vivo study using centre of mass analysis. *Journal of Hand Surgery* 20A, 937–943.
- Willis, A. a, Berger, R. a, Cooney, W.P., 2007. Arthroplasty of the distal radioulnar joint using a new ulnar head endoprosthesis: preliminary report. *The Journal of Hand Surgery* 32, 177–189.
- Yosibash, Z., Trabelsi, N., Milgrom, C., 2007. Reliable simulations of the human proximal femur by high-order finite element analysis validated by experimental observations. *Journal of Biomechanics* 40, 3688–3699.

Chapter 2 - Development and Validation of a Strain Gauge Embedment Methodology for Use with PMMA Bone Cement

OVERVIEW: It has been suggested that cement-stem debonding alters the transfer of load from an orthopaedic implant stem to the surrounding bone and thereby plays a role in stress shielding. The study outlined in this chapter aims to develop a strain gauge embedment technique capable of measuring strains within the cement mantle surrounding the implant stem, without compromising the integrity of the structure. The developed methodology will be used in subsequent studies to determine the impact of cement-stem debonding on load transfer patterns following distal ulnar arthroplasty.

2.1 Introduction

The lifelong functionality of upper-limb orthopedic implants is dependent upon the quality of implant fixation to the surrounding bone. For cemented implants, this linkage is achieved via a cement mantle; however, there are long-term complications associated with this method of fixation. Currently, the primary reasons for revision surgery and replacement of these devices is due to loosening or failure within the cement (Verdonschot and Huiskes, 1997a; McGee *et al.*, 2000; Lennon, 2003).

To better understand the potential causes of implant failure, it would be advantageous to determine the forces acting within the cement mantle itself. However, the mechanical measurement of forces acting within a solid body is quite challenging. The complexity of measuring the state of stress-strain within the mantle is exacerbated due to the limitations in measurement techniques available for this purpose. Most procedures are capable of accurately measuring strain on a free surface; however, for this application, embedment of the sensor (*i.e.*, strain gauge) within the cement is necessary. As such, it is important to qualify the functionality of the gauge under the adverse loading conditions present within cement, including increased temperature, moisture, pressure, and constrictive geometry.

Several strain gauge embedment procedures have previously been described in the literature, employing either a gauge carrier or bonding process to fixate the gauge within the cement mantle (Draganich *et al.*, 1982; Davey *et al.*, 1993; O'Connor *et al.*, 1996; Estok *et al.*, 1997; Fisher *et al.*, 1997; Wheeler *et al.*, 1997; Cristofolini and Viceconti, 2000; Ajovalasit, 2005; Cristofolini *et al.*, 2009). Gauge carrier studies use an adhesive to affix the strain gauge onto an isolated bone cement wafer prior to insertion into the canal, thereby providing a larger surface and easier access to properly orient the gauge (Davey *et al.*, 1993; O'Connor *et al.*, 1996; Estok *et al.*, 1997). In contrast, previous studies that have employed a bonding approach have utilized a two stage cementing process to affix the gauges within the mantle. First, a cement layer of known thickness is formed on the implant's surface and allowed to dry. Then the gauges are adhered to this layer using an adhesive (Fisher *et al.*, 1997; Wheeler *et al.*, 1997;

Cristofolini and Viceconti, 2000; Cristofolini *et al.*, 2009). The inclusion of an adhesive in both these techniques forms multiple interfaces adjacent to the gauge and discontinuities in the cement mantle. As well, neither methodology has been trialed within the tightly constrained mantle of an ulnar implant. Thus, the purpose of this study was to develop a gauge embedment technique that limited the number of interfaces around the gauge and was suitable for use within this restrictive region. Both the gauge carrier and bonding approaches were examined; however, due to early failures in generating a viable gauge carrier (Appendix 2) the research focus was directed towards developing a bonded gauge methodology that did not require the use of an adhesive.

2.2 Materials and Methods

Simplex P[®] bone cement (Stryker, Michigan, US) was mixed in an Optivac[®] Vacuum Mixing System (Biomet Inc, Warsaw, Indiana USA). When the Optivac[®] system is used, the powder and liquid cement components are combined in a cartridge, the cartridge is closed, and a 15-20 mmHg vacuum applied. The cement constituents are rapidly mixed, using the built-in plunger, for one minute, whereupon the cartridge is opened and cement poured into a syringe for dispensing. (A detailed description of the cementing technique is provided in Appendix 3.) Immediately following the mixing period, the cement is of a thick liquid consistency, but quickly becomes more viscous, hardening into a solid within 3-6 minutes at room temperature (Lewis, 1997). As it changes from liquid to solid, it passes through a “doughy phase” in which the cement exhibits adhesive properties (*i.e.*, it becomes tacky).

While the cement was still in its liquid state, it was applied to the surface of a smooth stainless steel stemmed implant (diameter of 5.8 mm). The location and thickness of application were controlled using a 0.5 mm template, which maintained a constant depth and area, ensuring localized cement application. As the cement moved into the doughy phase and reached the desired consistency, the mold was removed and a triaxial strain gauge (SGD-2/350-RY53, Omega Environmental, Quebec, Canada) was pressed onto the surface of the cement layer. (NOTE: A more detailed description of the gauging technique is outlined in Appendix 4.) After a period of approximately 20 minutes, the cement had dried sufficiently to proceed with implantation. This involved the feeding of the strain gauge wires through the bone canal, and exiting through a hole that had been drilled approximately 8 cm from the distal end of the bone. Cementing of the gauged implant into a Sawbone® third generation long bone (Pacific Research Laboratories Inc, Washington, USA) required a second package of vacuum mixed Simplex P®. Vacuum mixing is an important step in reducing the formation and limiting the presence of voids within the cement. The cement was then forced into the bone canal using a syringe, and the implant was carefully lowered into the canal. The gauge was wired into a Wheatstone bridge (quarter-bridge configuration). This configuration was obtained by connecting the wires to a data acquisition system (PXI-1050, National Instruments, Austin, TX, USA) through a strain gauge module (module SCXI-1314 and terminal block SCXI-1520).

After an eight hour curing period, the quarter bridge channels were calibrated and the unloaded strain output recorded at 1 Hz over a ten hour interval using a custom-written

LabVIEW® (National Instruments, Austin, TX) program. (Program details are provided in Appendix 5.) The cement was then left to cure for the remainder of the 24h period recommended by G. Lewis (1997). This choice of a prolonged curing period was selected since bone cement is susceptible to aftercure, where following the initial polymerization reaction, residual monomer gradually polymerizes over time altering the material properties of the cement (Lee *et al.*, 2002).

Post cure, the bone-cement-implant construct was positioned in a materials testing machine (Instron 8872, Canton, MA, USA) equipped with a 1,000 N load cell. Six different bending loads (5-30 N) were applied to the distal tip of the implant, held for 30 sec, and the load application repeated a total of three times. Load and displacement data from the Instron were simultaneously captured in LabVIEW®, along with the strain gauge output. Due to the variations in the mechanical behavior of bone cement over time (Lewis, 1997; Lee *et al.*, 2002), bending trials were repeated 48h and 7 days post embedment.

The strain response for each loading scenario was converted to principal strain using the equations listed in Section 1.4.1, after the unloaded sensor data was nulled to eliminate gauge offset. By analyzing the strain response throughout the initial ten hour unloaded period, the drift present in the system was monitored. The linearity of the strain response was verified, and for the 20 N load, Coefficients of Variation (CoVs) utilized to determine the repeatability within session, as well as, within and between days. Less than 5% variance was considered excellent and anything above 10% considered poor. Hysteresis was quantified by increasing and subsequently decreasing the bending load

between zero and 30 N over 15 second period. At 5 N intervals, the deviation between the loading and unloading curves was recorded, and the maximum deviation taken as the measure of the gauge's hysteresis.

Upon completion of testing, the specimen was disassembled and visually examined for the presence of voids or inconsistencies between the initial layer of cement applied to the stem (*i.e.*, gauge adhesion cement) and the Simplex P[®] forming the remainder of the canal. The area surrounding the gauge was also examined for voids, both around the gauge itself and between the gauge and Sawbone[®] canal wall.

2.3 Results

The signal from the embedded gauge was relatively stable after an initial settling period of approximately 2 hours. Prior to settling, fluctuations resulted in a drift of the principal strain of 49.6 $\mu\epsilon$ (standard deviation 8.2 $\mu\epsilon$). Over the remaining 8 hour recording period, further drift was limited to 8.7 $\mu\epsilon$ (standard deviation 3.9 $\mu\epsilon$) (Figure 2.1).

The strain gauge provided quality linear signals throughout the multiday testing protocol. The strain varied linearly with load ($R^2 \geq 0.99$) for all testing days, with marginally higher linearity during the first two testing days (Figure 2.2). The within session repeatability was acceptable with coefficients of variation between 7.8% and 8.7%. Within day and between day repeatability was excellent with 1.0% and 3.0% CoV, respectively (Table 2.1), and a minimal average hysteresis of 1.62 $\mu\epsilon$ was recorded. A compilation of all experimental principal strain data is available in Appendix 6.

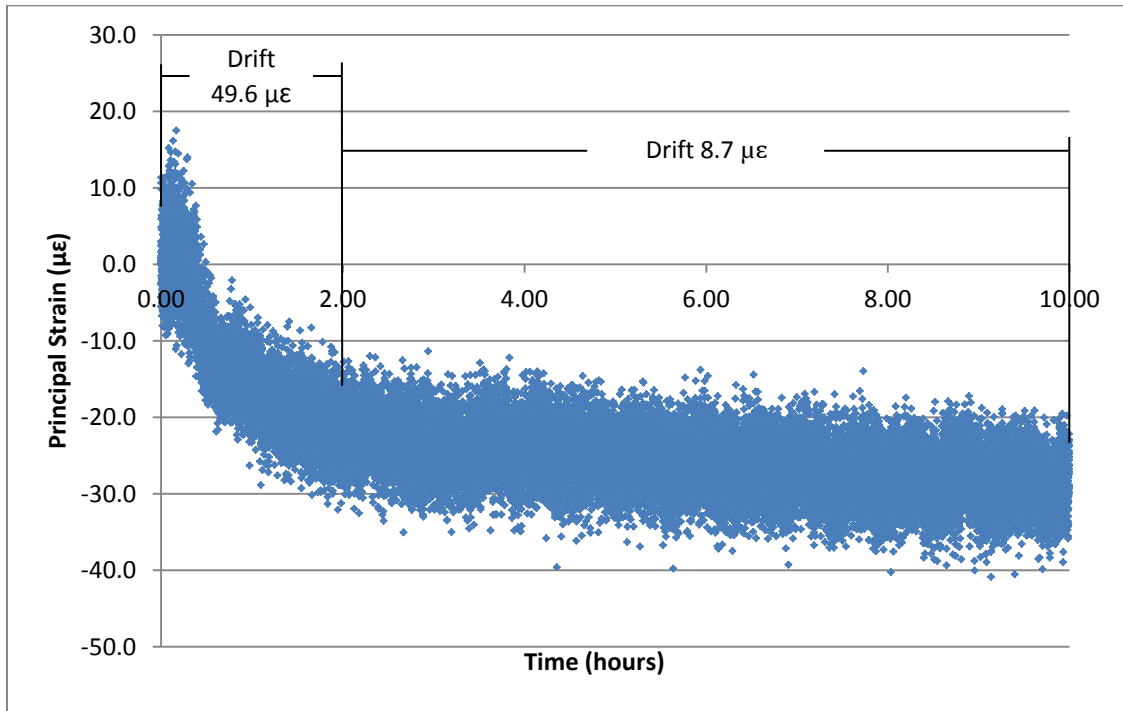


Figure 2.1: Drift of an embedded strain gauge

Principal strain of a triaxial rosette embedded in bone cement recorded over a ten hour period with a drift of $49.6 \mu\epsilon$ (standard deviation $8.2 \mu\epsilon$) over the first 2h and $8.7 \mu\epsilon$ (standard deviation $3.9 \mu\epsilon$) over the remaining 8h.

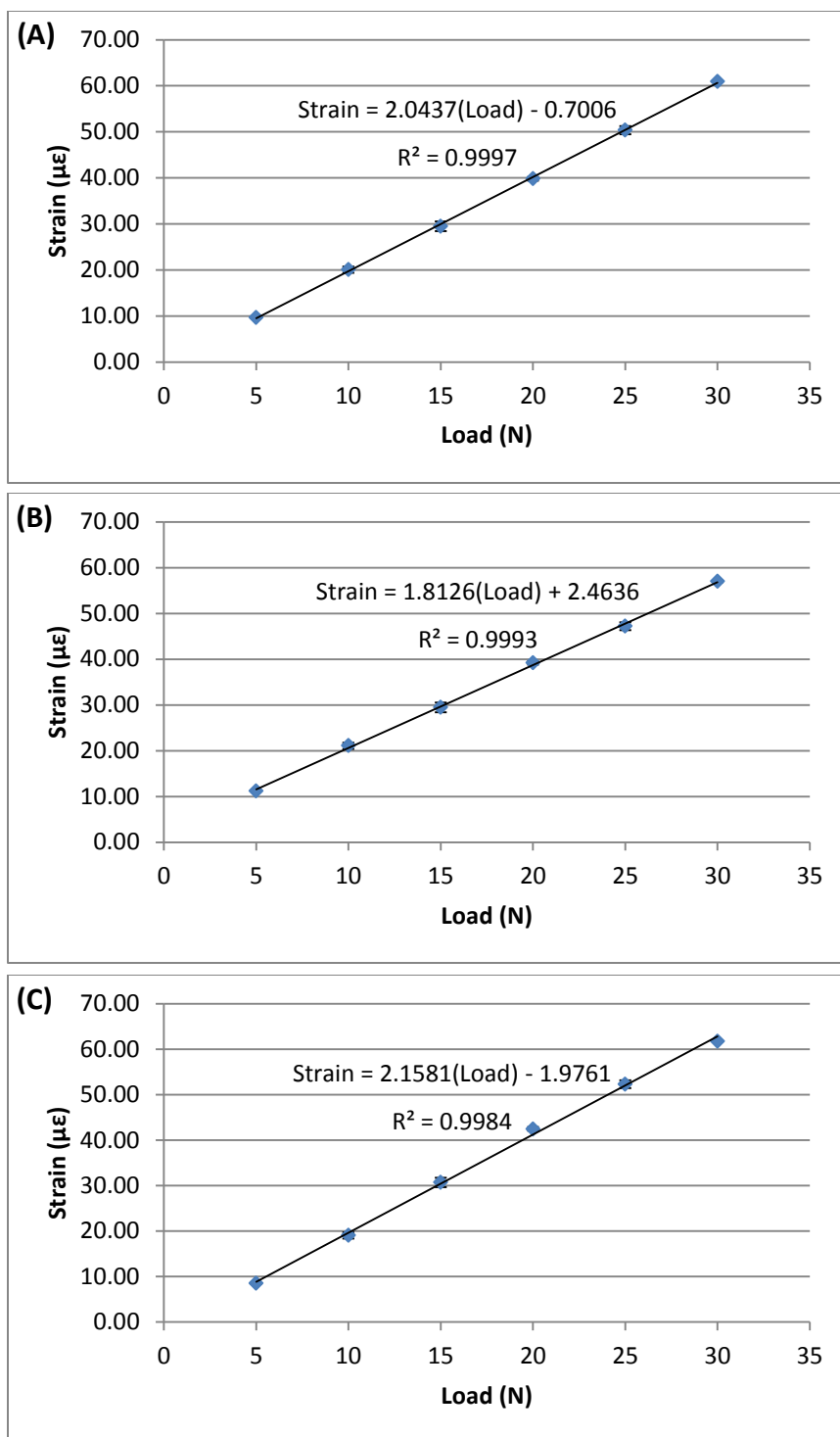


Figure 2.2: Linearity of strain response

Strain response from within the cement mantle in response to the application of 5-30 N bending loads **(A)** 24 h, **(B)** 48 h, and **(C)** 7 days post implantation in a Sawbone[®] model. Within day error bars are included on the 24 h graph **(A)**; however, due to the small standard deviation, they are difficult to visualize.

Table 2.1: Coefficients of variation within session, within day and between days

Coefficients of variation were calculated within session, within day and between days at 20 N applied bending loads.

Within Session Repeatability			
Session	Mean Strain ($\mu\epsilon$)	Standard Deviation ($\mu\epsilon$)	Coefficients of Variation (%)
1	40.4	3.3	8.3
2	39.6	3.4	8.6
3	39.5	3.4	8.6
Day 2	39.2	3.4	8.7
Day 7	42.5	3.3	7.8
Within Day Repeatability			
	39.8	0.4	1.0
Between Day Repeatability			
	40.2	1.2	3.0

Upon disassembly of the specimen, the cement used in gauging and implanting was examined and found to be successfully bonded. The area surrounding the gauge was inspected and no voids and cracks between boundaries were visually apparent.

2.4 Discussion

A reliable method of strain gauge embedment has been developed that limits the number of interfaces around the gauge and is suitable for use within constrained cement mantles. Despite the reduced mantle size and gauge inclusion 0.5 mm off the surface of the stem, the presence of gauges during implantation did not induce void formation.

Previously developed gauge embedment methodologies utilize an adhesive to bond the gauge to a fully cured section of PMMA bone cement prior to implantation (Fisher *et al.*, 1997; Wheeler *et al.*, 1997; Cristofolini and Viceconti, 2000; Cristofolini *et al.*, 2009). However, using the technique developed in this chapter, the strain gauge is bonded directly to the cement, excluding the use of adhesives and reducing the number of boundary layers within the mantle. The removal of a bonding adhesive eliminates the presence of sections of inconsistent material properties in the cement, which could potentially impact or alter strain transmission.

When a strain sensor is embedded in PMMA bone cement, the heat dispersion is reduced relative to the same sensor applied topically and exposed to air (*e.g.*, a gauge applied to the external bone surface). Therefore, time must be allotted to allow the sensor to reach thermal equilibrium owing to the heat generated by the sensor grid.

Due to the rapid and large drift two hours after gauge activation (49.6 $\mu\epsilon$, std dev 8.2 $\mu\epsilon$), as compared to the desired strain response during testing (Figure 2.2), experimental analyses performed during this period may not be accurate. Thermal equilibrium and sensor stability was reached two hours after gauge initialization; this finding is consistent with those found in literature (Cristofolini and Viceconti, 2000). Drift recorded after the initial two hour period was significantly reduced to 8.7 $\mu\epsilon$ (std dev 3.9 $\mu\epsilon$) over a ten hour interval. Though reduced, gauge readings taken at multiple instances over this period could be offset by drift; therefore, sensor calibration between trials is required to eliminate this offset.

Simplex P[®] bone cement is susceptible to diametral shrinkage, which over time could theoretically interfere with the cement-gauge bond (Davies and Harris, 1995). However, acceptable coefficients of variation were obtained within all sessions, indicating proper functioning of the strain gauges throughout the testing period. Bone cement is also susceptible to aftercure, where the gradual polymerization of residual monomer may affect the material properties of the cement (Lee *et al.*, 2002). As such, testing was repeated 24 h, 48 h and 7 days post mixing, and excellent between day coefficient of variation found. Based on these results, this methodology is acceptable for application in multiday testing protocols.

In summation, this experimental method provides a functional embedment technique capable of fixating strain gauges without the use of adhesives. This methodology will prove useful in the measurement of strains within the constrained mantle of an ulnar implant. In particular, gauge embedment is essential in determining the transfer of

strain from the area of load application on the implant head, to the cement mantle and distal bone; thus, enabling the measurement of changes in strain under different loading and cement-stem interface scenarios.

2.5 References

- Ajovalasit, A., 2005. Embedded strain gauges : effect of the stress normal to the grid. *Strain* 95–103.
- Cristofolini, L., Juszczak, M., Taddei, F., Field, R.E., Rushton, N., Viceconti, M., 2009. Stress shielding and stress concentration of contemporary epiphyseal hip prostheses. *Proceedings of the Institution of Mechanical Engineers, Part H: Journal of Engineering in Medicine* 223, 27–44.
- Cristofolini, L., Viceconti, M., 2000. Development and validation of a technique for strain measurement inside polymethyl methacrylate. *Journal of Strain Analysis* 35, 21–33.
- Davey, J.R., O'Connor, D.O., Burke, D.W., Harris, W.H., 1993. Femoral component offset, its effect on strain in bone-cement. *The Journal of Arthroplasty* 8, 23–26.
- Davies, J.P., Harris, W.H., 1995. Comparison of diametral shrinkage of centrifuged and uncentrifuge Simplex P® bone cement. *Journal of Applied Biomaterials* 6, 209–211.
- Draganich, L.F., Andriacchi, T.P., Galante, J.O., 1982. A technique for embedding strain gages within curing bone cement. *Journal of Biomechanics* 15, 789–790.
- Estok, D.M., Orr, T.E., Harris, W.H., 1997. Factors affecting cement strains near the tip of a cemented femoral component. *The Journal of Arthroplasty* 12, 40–48.
- Fisher, D., Tsang, A., Paydar, N., Millionis, S., Turner, C., 1997. Cement-mantle thickness affects cement strains in total hip replacement. *J. Biomechanics* 30, 1173–1177.
- Lee, A.J.C., Ling, R.S.M., Gheduzzi, S., Simon, J.-P., Renfro, R.J., 2002. Factors affecting the mechanical and viscoelastic properties of acrylic bone cement. *Journal of Materials Science: Materials in Medicine* 13, 723–733.
- Lennon, A., 2003. The relationship between cement fatigue damage and implant surface finish in proximal femoral prostheses. *Medical Engineering & Physics* 25, 833–841.
- Lewis, G., 1997. Properties of acrylic bone cement: state of the art review. *Journal of Biomedical Materials Research* 38, 155–182.

- McGee, M.A., Howie, D.W., Costi, K., Haynes, D.R., Wildenauer, C.I., Percy, M.J., Mclean, J.D., 2000. Implant retrieval studies of the wear and loosening of prosthetic joints : a review. *Society*, 158–165.
- O'Connor, D.O., Burke, D.W., Jasty, M., Sedlacek, R.C., Harris, W.H., 1996. In vitro measurement of strain in the bone cement surrounding the femoral component of total hip replacements during simulated gait and stair-climbing. *Journal of Orthopaedic Research : Official Publication of the Orthopaedic Research Society* 14, 769–777.
- Verdonschot, N., Huiskes, R., 1997. Cement debonding process of total hip arthroplasty stems. *Clinical Orthopaedics and Related Research* 336, 297–307.
- Wheeler, J.P.G., Miles, A.W., Clift, S.E., 1997. The influence of the stem-cement interface in total hip replacement--a comparison of experimental and finite element approaches. *Proceedings of the Institution of Mechanical Engineers, Part H: Journal of Engineering in Medicine* 211, 181–186.

Chapter 3 - Experimental Examination of the Effect of Implant Debonding on Load Transfer

OVERVIEW: Fixation of distal ulnar implants can impact load transfer through both the surrounding cement and bone. This study compares a bonded and debonded implant-cement interface in bending, torsion and combined loading, using strain gauges both within the cement mantle and on the exterior surface of the bone in cadaveric specimens. The results could have future implications for implant design.

3.1 Introduction

Damaged or severely arthritic distal radial ulnar joints may be treated using various surgical procedures (Darrach, 1913; Vincent *et al.*, 1993; Bain *et al.*, 1995; Ozer and Scheker, 2006). Of the existing options, only distal ulnar head arthroplasty preserves the anatomic relationship of the joint by replacing the ulnar head with a stemmed mechanical implant (Van Schoonhoven *et al.*, 2000; Sauerbier, 2002; KLS Martin Group, 2007). However, the long-term functionality of these prosthesis can be impacted by aseptic loosening, which is treated through complicated and costly revision surgery.

Debonding at the cement-stem interface has been hypothesized to contribute to early implant failure and has been shown to impact load transfer in multiple experimental and finite element studies of hip prosthesis (Crowninshield and Tolbert, 1983;

Verdonschot and Huiskes, 1996, 1997a, 1997b; Wheeler *et al.*, 1997; Verdonschot *et al.*, 1998). To the author's knowledge, no previous studies have examined the impact of interface fixation loss on load transmission surrounding distal ulnar implants. As such, the effect of debonding at the stem-cement interface, which could impact the transfer of load through the cement to the surrounding bone, is currently unknown. Quantifying these load changes (through monitoring strains) would be of interest in examining the effect of loss of interface fixation on the causative factors associated with aseptic loosening, including, mechanical failure of the cement and stress shielding resulting in bone loss (Sundfeldt *et al.*, 2006). In theory, a bonded implant would allow for greater load transfer through the cement mantle to the surrounding bone thereby reducing the effects of stress shielding.

The purpose of this study was to investigate the effect of cement-implant debonding on strains within the lateral cement mantle and distal ulnar bone under multiple loading conditions. The hypothesis was that strains within the cement mantle and surrounding bone would increase with debonding of the implant-cement interface; however, strains proximal to the implant would not be affected.

3.2 Materials and Methods

Eight fresh frozen cadaveric male ulnae (3 left, 5 right), with a mean age (\pm standard deviation) of 71 (\pm 8) years, were sectioned just distal to the coronoid process, thawed, and the proximal end cleaned of soft tissue (See Appendix 7 for specimen details). The distal ulnar head was removed and an intramedullary canal (7.9 mm diameter, 80 mm length from the cut distal surface) drilled by a fellowship trained surgeon. An additional

4.4 mm canal was drilled 80 mm from the cut distal edge through the lateral ulna. The proximal portion of each ulna was then cemented in a polyvinyl chloride (PVC) cylinder via a custom potting jig, and a laser level utilized to ensure alignment of the bone with the jig on both anterior-posterior and medial-lateral sides (Appendix 8, Figure A.6).

Two triaxial strain gauges (SGD-2/350-RY53, Omega Environmental, Quebec, Canada) were affixed with a 0.5 mm layer of Simplex P[®] bone cement (Stryker, Michigan, US), to an E-centrix[®] distal ulna implant (Wright Medical Technology, Tennessee, US), 1 cm and 4 cm from the distal end of the stem, using the methodology employed in Chapter 2 (Figure 3.1). Internal gauge positions were selected due to the predominant deviations in strain in the distal and proximal regions of the implant stem. As well, additional internal gauges were not added due to the size and mass of the wires. Key points on the implant were digitized both pre and post strain gauge fixation using a MicroScribe[®] (Revware, San Jose, California) to confirm gauge location and depth (Figure 3.2). Points of digitization are cataloged in Appendix 9.

Pilot studies indicated that breaking a cement-implant bond in a timely fashion would not be feasible. Therefore, this study was designed to first develop and test a debonded implant, following with the removal and recementing of the implant to create a bonded implant-stem interface. Several debonding agents were investigated, however it was determined that of the available options, petroleum jelly the only substance capable of inhibit bonding without compromising the cement mantle. (See Appendix 10 for release agent validation.)

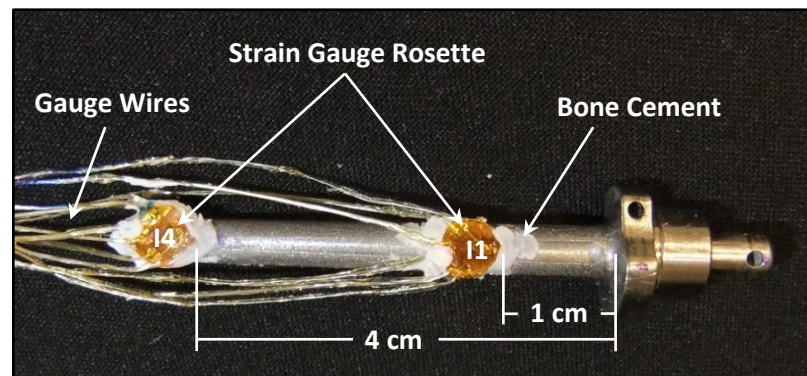


Figure 3.1: Internal gauge position and orientation

Internal gauges were attached to the Wright E-centrix implant with a 0.5 mm layer of Simplex P® bone cement. The proximal (I4) and distal (I1) strain gauges were positioned 4 cm and 1 cm respectively from the implant head. Omega Environmental model SGD-2/350-RY53 gauge rosettes were used, with short lead wires attached, external dimensions of 5.6 x 5.6 mm, and wire grid dimensions of 2.0 x 1.1 mm. The original lead wires were extended for testing using 32 gauge wires. However, the number of gauges was limited due to the bulk of the wires within the cement mantle.

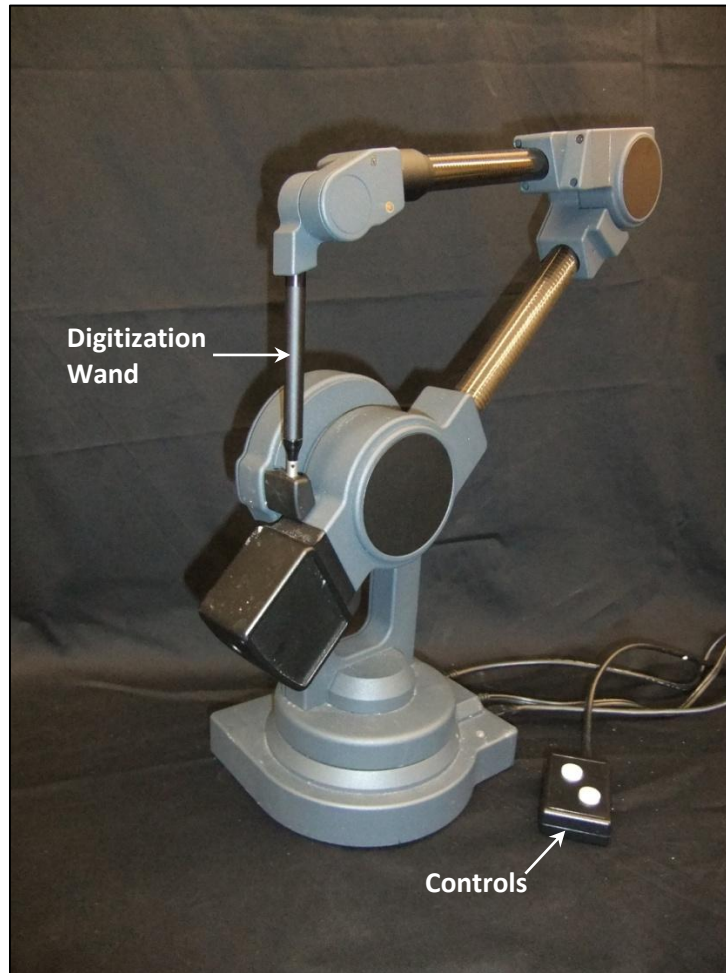


Figure 3.2: MicroScribe®

The MicroScribe® was used to digitize key points on the implant and bone both pre and post strain gauge fixation.

The implant was positioned and oriented with the gauges aligned along the lateral side of the distal ulna via a laser level and the gauge wires threaded through the canal and out the 4.4 mm lateral hole (Figure 3.3). The uncemented areas of the implant stem were coated with a layer of petroleum jelly to inhibit bonding. Using fluid vacuum mixed Simplex P[®] bone cement, pressurized with a syringe (Appendix 3), and consistent tension on the wires to prevent bunching, the E-centrix[®] distal ulna implant was inserted and cemented into the drilled intramedullary canal (as previously described in Section 2.2). The implanted ulna was then wrapped in a saline soaked towel, a thin layer of low density polyethylene (LDPE), and a LDPE bag for 24 h, to provide time for cement curing while maintaining bone moisture.

Post curing, the ulna was instrumented with five triaxial strain gauges (SGD-2/350-RY53) applied to the lateral external surface of the bone; one, two, four, five and ten centimeters from the distal end. A laser beam was projected on the bone surface throughout gauging to ensure gauge alignment along the long axis of the bone (Figure 3.4). The gauges were affixed using a previously developed gluing technique (Finlay *et al.*, 1982; Cordey and Gautier, 1999; Kim *et al.*, 2001; Dunham, 2005), further details of which are available in Appendix 11. When gauged, a MicroScribe[®] was used to digitize key points on the bone and potting fixture (Appendix 9).

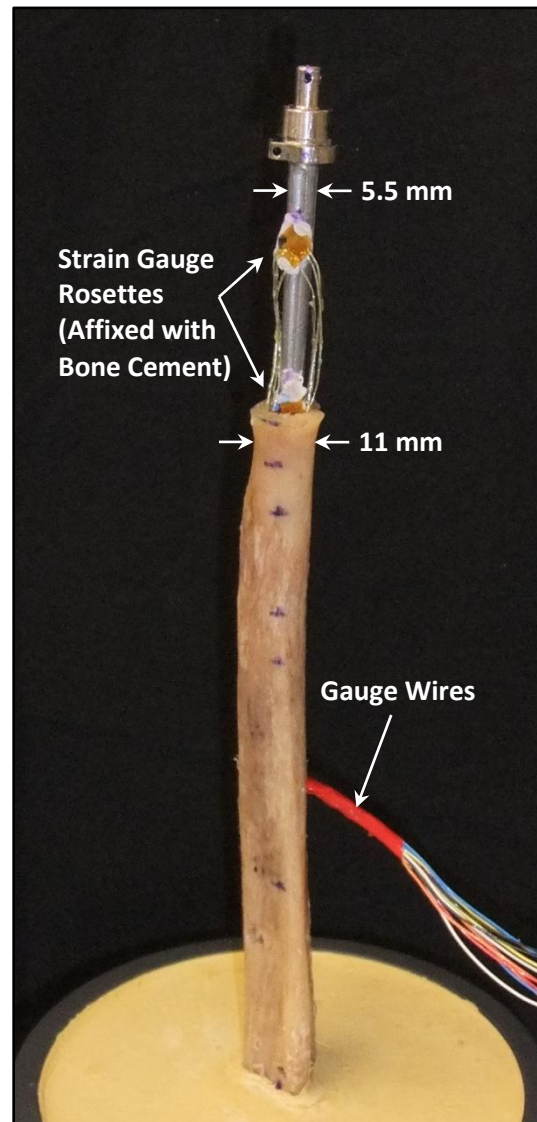


Figure 3.3: Implant oriented for embedment

Implant and internal gauges positioned and oriented in a cadaver ulna prior to cementing and implantation. Gauge wires are visible exiting the bone through a 4.4 mm proximal hole.

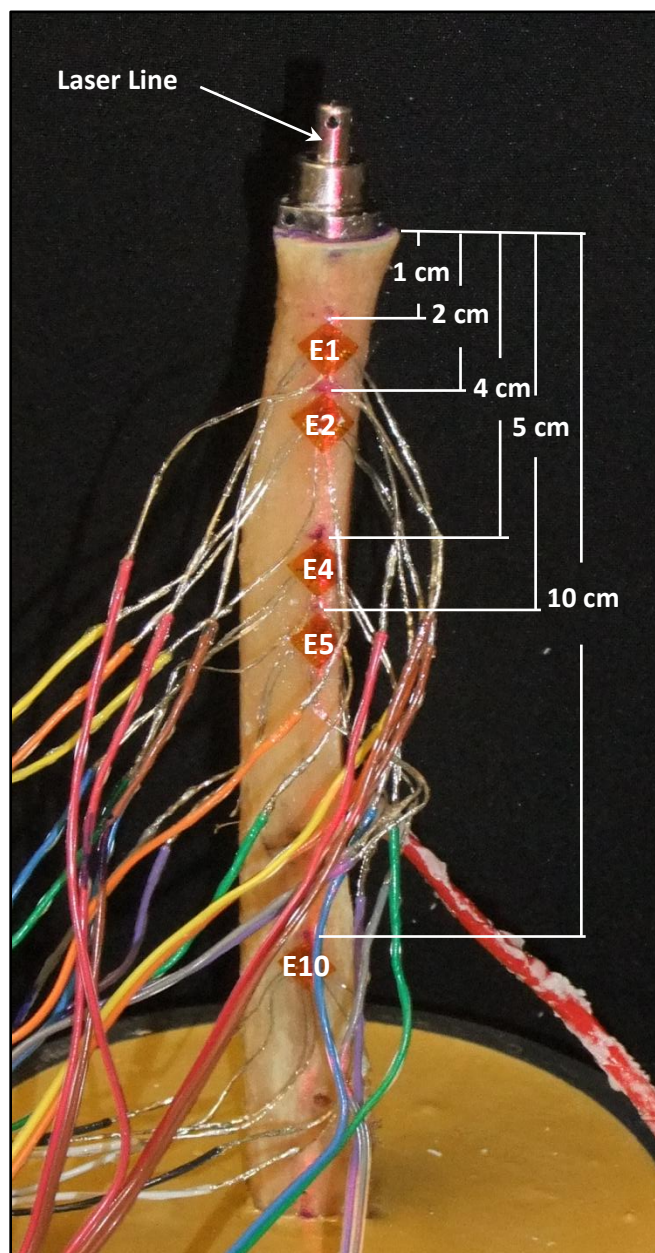


Figure 3.4: External gauge location and alignment

Triaxial gauges (E1, E2, E4, E5, and E10) were applied at set distances along the lateral side of the bone. A laser level was used to facilitate gauge alignment along the long axis of the bone.

The internal and external gauges were connected to a data acquisition system (SCXI 1520, National Instruments, Austin, TX, USA) through a strain gauge module, using a Wheatstone quarter-bridge configuration, and a 2.5 V excitation voltage. The strain response from the gauges, as well as the load and displacement data from the materials testing machine (Instron 8872, Canton, MA, USA) were recorded via a custom LabVIEW® (National Instruments, Austin, TX) program. See Appendix 5 for LabVIEW® program details.

The ulna was positioned in a materials testing machine with a 1,000 N load cell (Instron 8872, Canton, MA, USA) and secured via the PVC cylinder in a custom jig setup (Figure 3.5A). Prior to testing all gauges were connected and operated for at least two hours to allow the system to reach thermal equilibrium, in accordance with the findings of Chapter 2. Despite the application of petroleum jelly to the stem, bonding still occurred (although weakened). A debonded interface was obtained through the application of torsional loads until implant rotation of 7° (as recommended by a fellowship trained surgeon as the rotational point of definitive debonding) was obtained (Takaki, 2007). Using a 200 N load cell and the Instron®, six different bending loads (5-30 N) were sequentially applied to the lateral-side of the distal implant tip, thereby generating a moment about the anterior-posterior axis simulating the DRUJ reaction force during active unresisted forearm rotation (Gordon *et al.*, 2006).

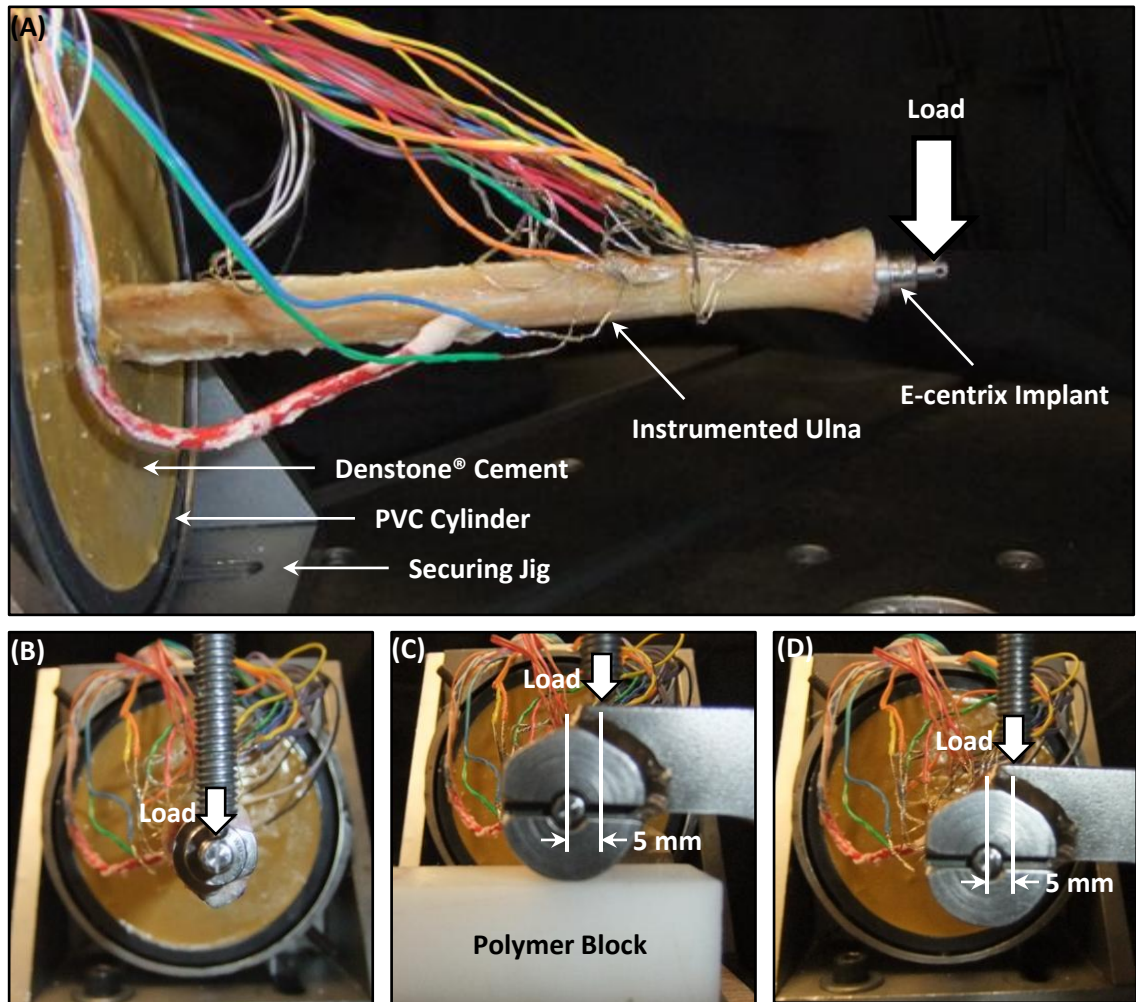


Figure 3.5: Experimental setup and points of load application

(A) Lateral view of the implant cement loading setup. The proximal portion of each gauged and implanted ulna was potted in a PVC cylinder and secured in a custom jig setup. Six different loads (5-30 N) were sequentially applied in (B) bending, (C) torsion, with a supporting polymer block to prevent bending, and (D) combined loading. (End on view) All loads were applied via an Instron® materials testing machine.

Similarly, six different loads (0.025-0.15 Nm) were sequentially applied five millimeters from center along a supported and unsupported torque arm to simulate torsional and combined loading, respectively, during active unresisted forearm rotation in accordance with the findings of Gordon *et al.* (2006). All loads were applied at load-controlled rate of 2 N/s, held for 30 sec, unloaded at 2 N/s and held for 10 sec to allow a cement relaxation period prior to application of the next load (Appendix 12). Overall the total loading period took approximately 6 min. As such, it is not expected that the drift of the internal gauges, noted in Section 2.4, would affect the gauge response during this short of an interval. Load orientation and points of application are displayed in Figure 3.5, and both bending and torsional free body diagrams are provided in Appendix 13.

Using combined axial (*i.e.*, pull out) and torsional loading the implant was removed from the bone (leaving the strain gauges behind in the mantle), the canal reamed (being careful not to damage the gauges or wires), and implant recemented using another package of vacuum mixed Simplex P[®] bone cement. The loading protocol was repeated 14-16 h post reimplantation, to allow time for the cement to cure. Post testing, debonding of the implant-cement interface was attempted through the application of torsional loads until 7° rotation of the implant-bone construct was obtained. Throughout testing, bone moisture was maintained through regular applications of deionized water. Deionized water was used as opposed to saline to avoid compromising the external gauges, due to sodium buildup on the gauges and gauge wires. A detailed testing protocol is provided in Appendix 9.

To eliminate gauge offset the unloaded strain response was nulled, and the resultant strain values for each loading scenario converted to principal strain using the equations listed in Section 1.4.1. One-way repeated measures ANOVAs ($\alpha = 0.05$) were performed on the bonded and debonded data for all gauges at 10, 20 and 30 N applied loads with bonding condition as the factor. Post-hoc Student-Newman-Keuls tests were used in all analyses, where a value of $p < 0.05$ was considered significant.

3.3 Results

The external gauges were fully bonded and functional throughout testing. Internal gauges were successfully embedded in the cement at an average depth of 0.52 mm (standard deviation ± 0.13) from the surface of the implant stem, based on measurements developed from MicroScribe® data. Of the internal gauges, one proximal gauge (I4) lost adhesion during stem implantation (specimen #10-06020), and one distal gauge (I1) failed during implant removal after the debonded and prior to the bonded trials (specimen #09-13055). Both defective gauges were disregarded prior to analysis.

Cement-stem debonding ($\geq 7^\circ$ rotation) of the initial compromised interface was successful in all ulnae ($n=8$) (Figure 3.6); however, when the specimen was torqued to seven degrees post rebonding, implant rotation was not observed (*i.e.*, motion generated through bone twist, and possible bone fracture). The loads necessary to reach seven degree rotation with a compromised (average load 2.8 Nm, std dev 0.8) interface, were significantly lower than those with a bonded (average load 4.9 Nm, std dev 1.2) interface condition ($p=0.003$).

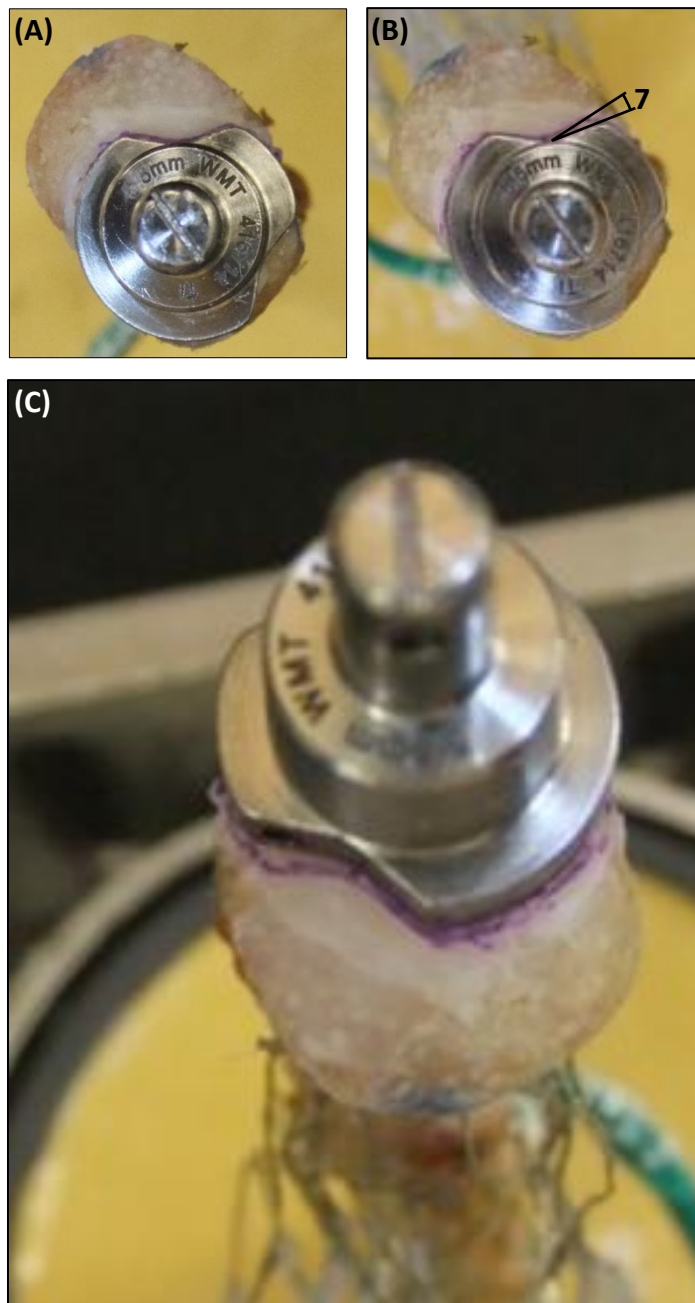


Figure 3.6: Implant orientation pre and post-ulna torsion to 7°

Implant stem orientation in cadaver distal ulna **(A)** at start, and **(B)** post cement-implant debonding. **(C)** Debonded implant orientation post 7° rotation with initial orientation outlined in purple.

The internal and external strain responses to a 20 N bending load are shown in Figure 3.7B. Variations in bonding conditions at the implant-cement interface did not influence internal or proximal-external strains. External strains one and two centimeters from the distal surface of the bone were increased with bonding of the implant-cement interface ($p_{E1}, p_{E2} < 0.001$). A similar gauge response was noted under combined loading, with bonding of the implant-cement interface resulting in increases in strain at E1 ($p < 0.001$) and E2 ($p < 0.001$) (Figure 3.8B). Increases in strain were noted in the bonded scenario in gauges E1 ($p = 0.002$), E2 ($p < 0.001$) and I4 ($p = 0.048$) with application of 0.1 Nm torsional loads. Deviations in strain between the bonded and debonded scenario for the remaining external and internal gauges were not significant (Figure 3.9B).

Variations in strain response were consistent at alternate loads (10 and 30 N) in bending (Figure 3.7A&C) and combined loading scenarios (Figure 3.8A&C). Likewise, under torsion there was no variation in gauge response, with the exception of E4 (Figure 3.9). Under higher torsional loads (0.15 Nm), the bonded interface resulted in higher strains than debonded at E4 ($p = 0.013$). A compilation of all experimentally determined principal strain data is available in Appendix 14.

3.4 Discussion

Long-term maintenance of an implant-cement bond cannot be assured throughout the life of an implant (McGee *et al.*, 2000). As such, several studies have investigated the effect of cement-stem interface debonding on cement strains in the proximal femur.

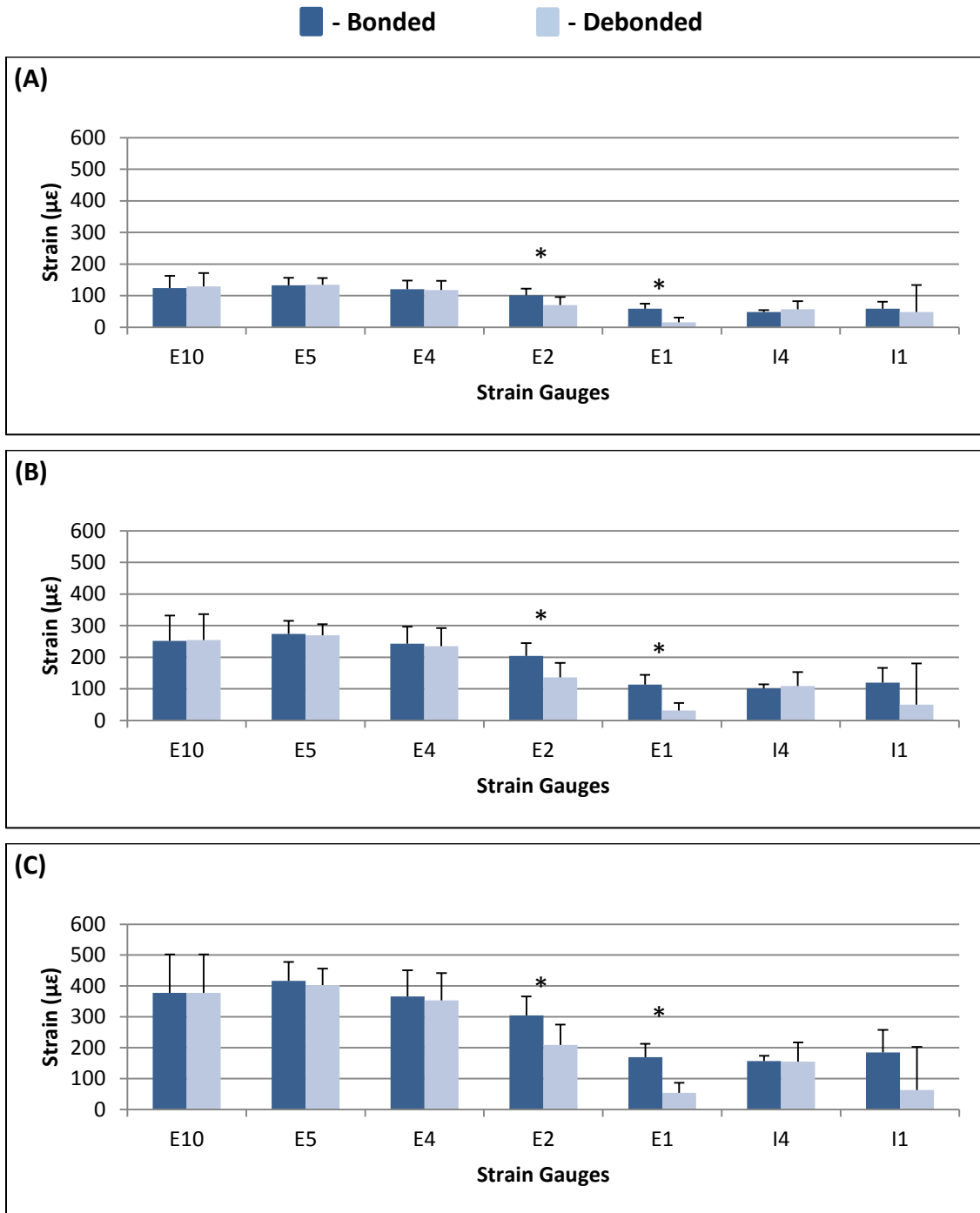


Figure 3.7: Mean and standard deviation between specimens in bending

Microstrain data in response to the application of **(A)** 10 N, **(B)** 20 N, and **(C)** 30 N bending loads. Significance ($p < 0.05$) is denoted with an asterisk (*).

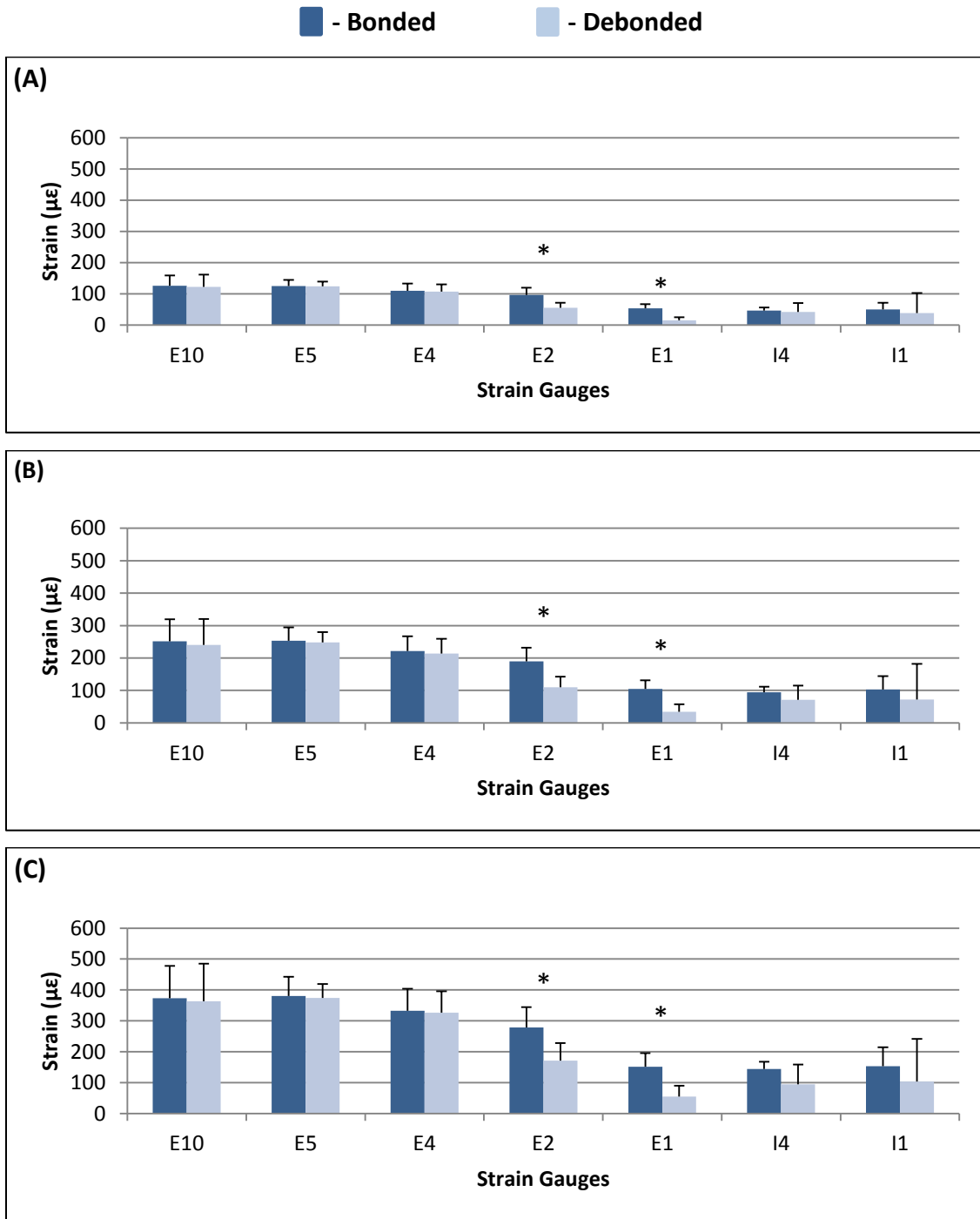


Figure 3.8: Mean and standard deviation between specimens in combined loading

Microstrain data in response to the application of combined loads, **(A)** 10 N bending and 0.05 Nm torque, **(B)** 20 N bending and 0.10 Nm torque, and **(C)** 30 N bending and 0.15 Nm torque. Significance ($p < 0.05$) is denoted with an asterisk (*).

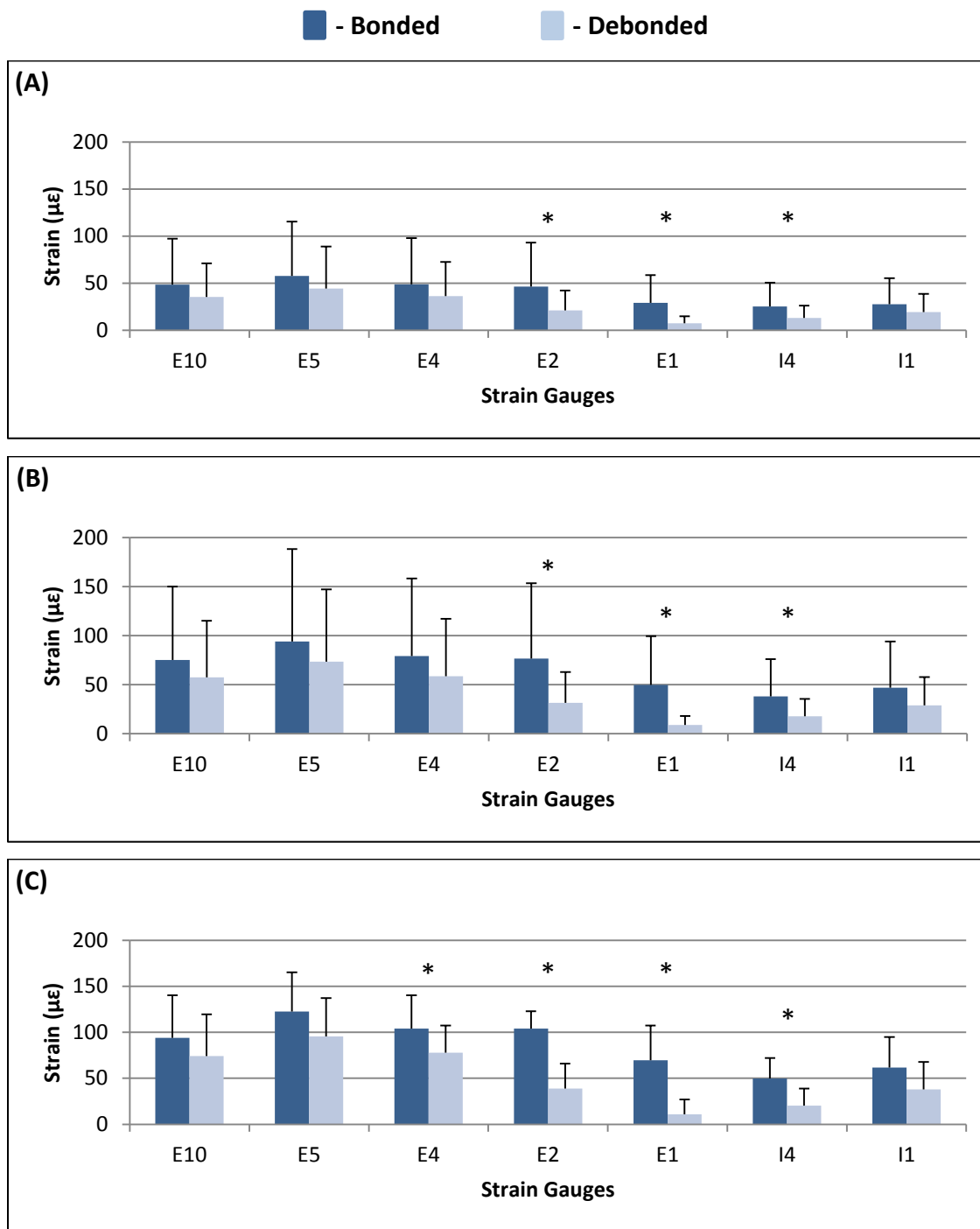


Figure 3.9: Mean and standard deviation between specimens in torsion

Microstrain data in response to the application of **(A)** 0.05 Nm, **(B)** 0.10 Nm, and **(C)** 0.15 Nm torsional moments. Significance ($p < 0.05$) is denoted with an asterisk (*).

These studies suggest that when loads are applied parallel to the long axis of the femur and the implant stem debonded, strains within the cement mantle increase between two to four times those found with a bonded stem (Crowninshield and Tolbert, 1983; Mann *et al.*, 1995; Verdonschot and Huiskes, 1997a, 1997b; Wheeler *et al.*, 1997). Other studies have indicated that the increase in strain found in the debonded cement mantle may be partially negated by increasing interface friction through the inclusion of axial grooves or increased surface roughness in the implant stem design (Verdonschot and Huiskes, 1996; Verdonschot *et al.*, 1998).

To the author's knowledge, no previous studies have directly compared the effect of implant-cement debonding on strains within the cement mantle of an ulnar implant. This is challenging work due to the size constraints of the bone and canal. Also, since the loads received by the distal ulna are much smaller and the direction of loading dissimilar from those found in the femur (Gordon *et al.*, 2006), variants in strain observed in femoral studies may not pertain to those of the upper limbs.

In the cement mantle, significant decreases in strain were noted in the proximal mantle and reduced strain in the distal mantle under torsional loading conditions. The decrease in strain within the cement may be explained through the surface geometry of the E-centrix® implant, which is both fluted and roughened. This results in a high interface friction, thereby reducing the load transfer from the stem to the surrounding cement.

The lack of significance in the distal internal gauge should be treated with caution. In the distal region inconsistencies within the cement were more prevalent, owing to the potential for void formation during implant insertion, due to inconsistencies in the

cadaver bone. There is therefore a greater degree of deviation in the resulting data between specimens, which could negate otherwise significant results. As such, additional specimens would be required to reach significance at the distal internal gauge.

Previous studies have investigated strains on the external surface of the distal ulna under both bonded and debonded cement-implant interface conditions. Austman *et al.* (2008) showed that in the distal ulna stem-cement interface, debonding of a threaded implant under bending did not impact lateral bone strains. This outcome was observed in the proximal gauges utilized in this study, but distally, strains decreased with interface debonding. As the inter-study discrepancy is only noted in external gauges directly overlaying the implant stem, this deviation in results may be attributed to the variations in stem geometry between the straight threaded stem utilized by Austman *et al.* (2008) and the tapered, fluted and roughened commercial stem utilized in this study.

A decrease in the distal bone strain between the bonded and debonded implant-cement interface was observed in all loading scenarios. Such a decrease in strain could be an indicator for stress shielding and resulting bone resorption. This would be consistent with the results found in current short-term clinical reviews of ulnar prosthesis, where evidence of bone resorption (potentially as a result of stress shielding) was found in the distal region of the ulna (Willis *et al.*, 2007).

Decreases in strain with debonding were observed in the most distal portion of the ulna; however, at higher torsional loads, a decrease in strain was also noted in the bone directly exterior to the proximal end of the stem. One possible explanation is to

consider the shear modulus of both the cement and bone. At low loads, the strains will be relatively close in magnitude, owing to the linearity of the stress strain curve; however, as the loads increase, the resulting strains will also deviate. The applied torsional loads of 0.05 – 0.15 Nm were determined based on a prior study by Gordon *et al.* (2006), which found average DRUJ loads in the neutral position during unrestrained forearm rotation fell within this range (Gordon *et al.*, 2006). As such, debonding load variations on the ulna at the proximal end of the stem may not be seen during the majority of normal forearm rotation; however, during the higher forces which could potentially be incurred during activities of daily living, this deviation may be significant.

Although multiple factors may contribute to distal ulnar implant failure, the purpose of this study was to focus on the impact that implant-cement debonding has on strains (and thereby stresses) in the bone and cement mantle. This study is limited due to the utilization of elderly cadaveric bone, the measurement of strains at discrete locations in both the bone and cement, and the potential for variation in cement mantle properties due to the embedment of mechanical gauges. Furthermore, as the cement-implant interface is normally degraded through long durations of cyclic loading and exposure to bodily fluids (Crowninshield and Tolbert, 1983), the utilization of a release agent and multistage bonding process did not provide a strictly realistic model. These may be addressed, in part, through the development of a validated finite element model (FEM) to examine these conditions.

Distal ulnar head arthroplasty can greatly improve the quality of life for individuals afflicted with both chronic disorders and severe traumatic injuries to the distal

radioulnar joint. Through greater understanding of the load transfer pathways, implant designs may be adapted to improve clinical outcomes. As such, the results of this study suggest that debonding of the implant cement interface reduces strains both within the cement and within the surrounding bone, which suggests that compromising the implant-cement interface, may lead to stress shielding and ultimately implant failure.

3.5 References

- Austman, R.L., Quenneville, C.E., Beaton, B.J.B., King, G.J.W., Gordon, K.D., Dunning, C.E., 2008. Development of a testing methodology to quantify bone load transfer patterns for multiple stemmed implants in a single bone with an application in the distal ulna. *Journal of Biomechanical Engineering* 130, 024502.
- Bain, G., Pugh, D., MacDermid, J., Roth, J., 1995. Matched hemiresection interposition arthroplasty of the distal radioulnar joint. *Journal of Hand Surgery* 20A, 944–950.
- Cordey, J., Gautier, E., 1999. Strain gauges used in the mechanical testing of bones. Part II: “In vitro” and “in vivo” technique. *Injury* 30A, 14–20.
- Crowninshield, R.D., Tolbert, J.R., 1983. Cemented strain measurement surrounding loose and well-fixed femoral component stems. *Journal of Biomedical Materials Research* 17, 819–828.
- Darrach, W., 1913. Partial excision of lower shaft of ulna for deformity following colles’s fracture. *Annals of Surgery* 57, 764–765.
- Dunham, C.E., 2005. Biomedical assessments of synthetic and cadaveric distal humeri for laboratory-based investigations [M.E.Sc. Thesis]. The University of Western Ontario
- Finlay, J.B., Bourno, R.B., McLean, J., 1982. A Technique for the in vitro measurement of principal strains in the human tibia. *Journal of Biomechanics* 15, 723–739.
- Gordon, K.D., Kedgley, A.E., Ferreira, L.M., King, G.J.W., Johnson, J.A., 2006. Design and implementation of an instrumented ulnar head prosthesis to measure loads in vitro. *Journal of Biomechanics* 39, 1335–1341.
- KLS Martin Group, 2007. Herbert ulnar head prosthesis [Brochure]. KLS Martin Group

- Kim, Y., Kim, J.S., Cho, S.H., 2001. Strain distribution in the proximal human femur: An in vitro comparison in the intact femur and after insertion of reference and experimental femoral stems. *The Journal of Bone and Joint Surgery (Br)* 83, 295–301.
- Mann, K.A., Bartel, D.L., Wright, T.M., Burstein, a H., 1995. Coulomb frictional interfaces in modeling cemented total hip replacements: a more realistic model. *Journal of Biomechanics* 28, 1067–1078.
- McGee, M.A., Howie, D.W., Costi, K., Haynes, D.R., Wildenauer, C.I., Pearcy, M.J., Mclean, J.D., 2000. Implant retrieval studies of the wear and loosening of prosthetic joints : a review. *Society* 158–165.
- Ozer, K., Scheker, L.R., 2006. Distal radioulnar joint problems and treatment options. *Orthopedics* 29, 38–49.
- Sauerbier, M., 2002. The dynamic radioulnar convergence of the Darrach procedure and the ulnar head hemiresection interposition arthroplasty: a biomechanical study. *The Journal of Hand Surgery: Journal of the British Society for Surgery of the Hand* 27, 307–316.
- Takaki, S.E., 2007. The Effect of Cross-sectional and Longitudinal Intramedullary Stem Shape on the Stability of Cemented Implants [M.E.Sc. Thesis]. The University of Western Ontario
- Van Schoonhoven, J., Fernandez, D.L., Bowers, W.H., Herbert, T.J., 2000. Salvage of failed resection arthroplasties of the distal radioulnar joint using a new ulnar head prosthesis. *The Journal of Hand Surgery* 25, 438–446.
- Sundfeldt, M., Carlsson, L.V., Johansson, C.B., Thomsen, P., Gretzer, C., 2006. Aseptic loosening, not only a question of wear: a review of different theories. *Acta Orthopaedica* 77, 177–197.
- Verdonschot, N., Huiskes, R., 1996. Mechanical effects of stem cement interface characteristics in total hip replacement. *Clinical Orthopaedics and Related Research* 329, 326–336.
- Verdonschot, N., Huiskes, R., 1997a. The effects of cement-stem debonding in THA on the long-term failure probability of cement. *Journal of Biomechanics* 30, 795–802.
- Verdonschot, N., Huiskes, R., 1997b. Cement debonding process of total hip arthroplasty stems. *Clinical Orthopaedics and Related Research* 336, 297–307.
- Verdonschot, N., Tanck, E., Huiskes, R., 1998. Effects of prosthesis surface roughness on the failure process of cemented hip implants after stem-cement debonding. *Journal of Biomedical Materials Research* 42, 554–559.

- Vincent, K., Szabo, R., Agee, J., 1993. The Sauve-Kapandji procedure for reconstruction of the rheumatoid distal radioulnar joint. *Journal of Hand Surgery* 18A, 978–983.
- Wheeler, J.P.G., Miles, A.W., Clift, S.E., 1997. The influence of the stem-cement interface in total hip replacement--a comparison of experimental and finite element approaches. *Proceedings of the Institution of Mechanical Engineers, Part H: Journal of Engineering in Medicine* 211, 181–186.
- Willis, A.A., Berger, R.A., Cooney, W.P., 2007. Arthroplasty of the distal radioulnar joint using a new ulnar head endoprosthesis: preliminary report. *The Journal of Hand Surgery* 32, 177–189.

Chapter 4 - Finite Element Examination of the Effect of Implant Debonding on Load Transfer

OVERVIEW: *Finite element models enable the testing of multiple biomechanical scenarios in a time and resource effective fashion; however, the quality of the data obtained in this manner is only as accurate as the model itself. As such, this study expands the capabilities of a previously developed and validated finite element model of distal ulnar arthroplasty, to include the addition of cement strains and variable cement-stem interface conditions.*

4.1 Introduction

The development of finite element (FE) models capable of accurately quantifying the mechanical behavior of biological tissues and components can be advantageous to the field of orthopedic biomechanics. Such models may be used to test a wide array of implant designs and conditions in a more cost-effective and timely manner than could be accomplished via *in vitro* testing. However, prior to their widespread use, such models must be validated to ensure their ability to mimic the results from the *in vitro* (or *in vivo*) studies they are designed to represent. In the case of models designed to quantify the behavior of cemented distal ulnar joint replacement systems, this includes

accurately representing strains within the cement mantle for both bonded and debonded cement-stem interface conditions.

Multiple FEM studies have successfully modeled the cement-implant interface of femoral implants and quantified the surrounding cement strains (Mann *et al.*, 1991, 1995; Verdonschot and Huiskes, 1996; Wheeler *et al.*, 1997; Ramaniraka and Rakotomanana, 2000; Nuño and Amabili, 2002). The majority of such studies have determined that the smooth debonded femoral stem-cement interface may be accurately represented using the Coulomb friction model. Coulomb friction assumes that atomically close contact only occurs over a small fraction of the contact surface, and relates the stress that may be transferred along the interface in shear to the stress transferred normal to the interface, by the coefficient of friction (Mann *et al.*, 1991). Each element in the frictional region may be sticking (Equation 5), slipping (Equation 6), or open (Equation 7).

$$\tau < F_f \sigma_n \quad \text{Equation 5}$$

$$\tau = F_f \sigma_n \quad \text{Equation 6}$$

$$\sigma_n = 0 \quad \text{Equation 7}$$

Where: τ = Shear stress
 F_f = Coefficient of friction
 σ_n = Stress normal to the interface

Unlike finite element models of the femur, models of the distal ulna have been limited to the examination of bone surface strains under bonded cement-stem interface conditions. As such, the purpose of this study is to advance a distal ulnar model previously developed by Austman *et al.* (2009) to incorporate strains within the cement mantle, and to determine the functionality of a Coulomb frictional interaction in modeling a debonded cement-implant interface.

4.2 Materials and Methods

The eight specimen's experimentally tested in Chapter 3 were scanned using a micro CT scanner with 152 μm voxel spacing (eXplore Ultra, GE Healthcare, London, Canada) to capture bone geometry and density information. The scans were completed after the proximal end of each specimen was potted in the PVC cylinder and the intramedullary canals drilled (see Section 3.2), but prior to implant embedment. One specimen (specimen number 09-12057) was selected for modeling, as its exhibited strain results most closely matched the average strain data computed from the eight tested specimens (Table 4.1).

To enable the creation of a three dimensional model, the micro-CT files obtained from the scan (.vff format) were converted to DICOM (Digital Imaging and Communications in Medicine) using Microview (GE Healthcare, London, Ontario). The files were then imported into MIMICS[®] (Materialise, Leuven, Belgium), where the software's thresholding features were used to isolate the bone's exterior and interior canal geometry.

Table 4.1: Difference between independent and averaged gauge response

The percent differences between the experimentally determined specimen and average strain in response to a 20 N bending load are displayed. Results were calculated across both bonded and debonded conditions, and averaged for all internal and external gauges. The average percentage difference was also calculated across all gauges for each specimen, and the lowest average percentage difference highlighted in yellow.

	E1 (%)	E2 (%)	E4 (%)	E5 (%)	E10 (%)	I1 (%)	I4 (%)	Average (%)
09-12057	-28.4	14.3	21.3	-10.1	-41.4	26.7	23.7	0.9
09-13055	Eliminated due to incomplete gauge set							
10-01004	36.8	29.2	33.3	6.3	51.3	-4.3	13.1	23.7
10-06020	Eliminated due to incomplete gauge set							
11-03022	-32.2	-36.4	8.9	8.2	-8.1	217.3	-40.2	16.8
11-03026	-74.2	20.0	9.7	3.0	-26.5	-272.6	-25.9	-52.4
11-03045	-31.6	32.5	-38.3	26.9	-11.0	27.0	7.6	1.9
11-03057	18.9	-33.7	10.8	-22.3	-25.4	28.7	8.2	-2.1

This enabled a three dimensional shell to be formed for each component (*i.e.*, interior and exterior) and exported as two separate IGES files for further analysis.

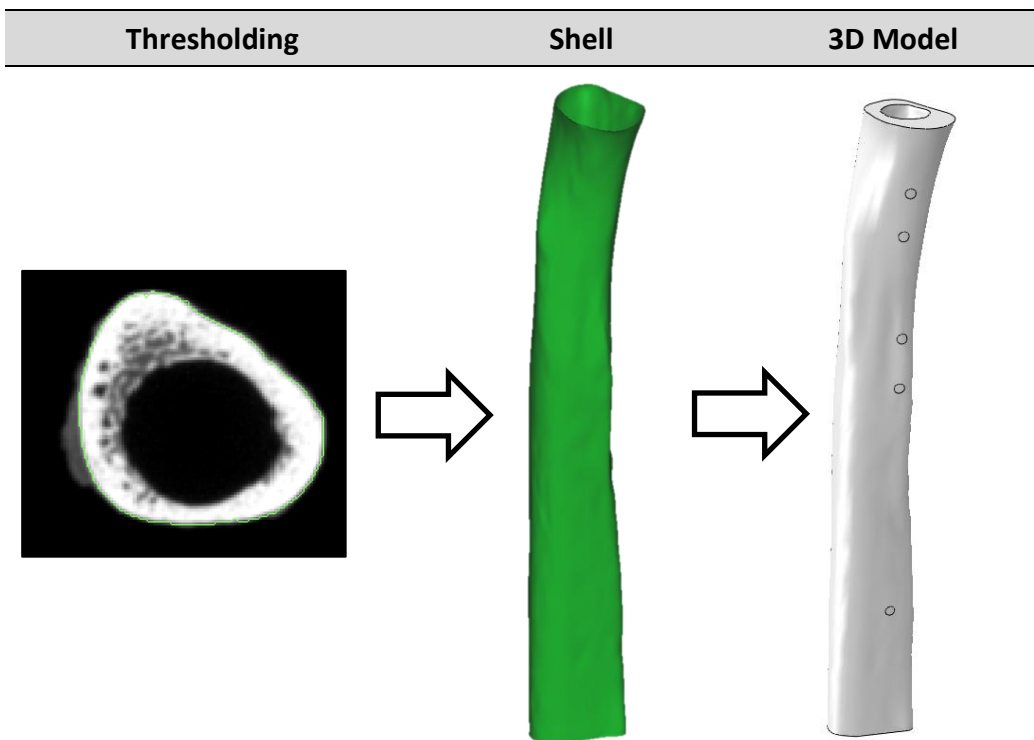
In Abaqus® (Simulia, Providence, Rhode Island, USA) the shells were converted to three dimensional models of the bone and associated cement canal. During the experimental specimen development, the internal bone canal was filled with cement prior to implant insertion (Section 3.2). Therefore, the cement mantle was developed by converting the shell of the internal bone canal into a three dimensional model, from which the volume of the implant stem was subtracted. Model development is depicted in Table 4.2. For the stem, a CAD model of the Wright E-centrix® implant was obtained directly from the manufacturer, and imported into the cement and bone assembly.

Validation of the model required comparing the finite element strains from the model to those captured by the strain gauges during experimental testing (Chapter 3). Therefore, the locations of the internal and external gauges were determined in the model based on the MicroScribe® coordinates collected for each gauge location relative to bone (external gauge) and implant (internal gauge) coordinate systems (Section 3.2). The bone and implant coordinate systems were recreated in Abaqus® and, based on the gauge coordinates, two millimeter circular “gauge regions” were identified at all internal and external gauge locations. The two millimeter radius was selected based on the active region of the experimental triaxial strain gauges.

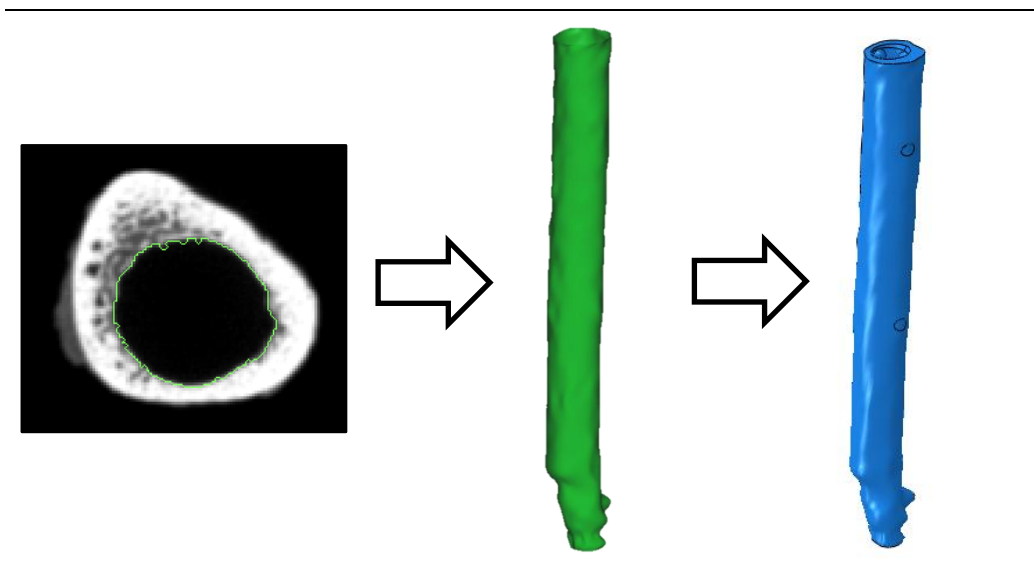
Table 4.2: Development of bone and cement model

The conversion of micro-CT files into 3D models occurred in three stages. Initially thresholding (green line) in MIMICS® was used to isolate the bone's exterior and interior canal geometry. Then a shell was formed for each component, which was exported into Abaqus® and converted into a 3D model.

Bone Model Development



Cement Model Development



Each component of the model was meshed with a 0.75 mm global mesh, and 0.30 mm local mesh at the gauge locations. Four independent meshes were generated for the bone (265,924 elements), cement (124,366 elements), implant (43,788 elements), and for a joined implant bone construct (167,286 elements). Previous studies of the ulna have validated the use of 0.75 mm global mesh (Austman *et al.*, 2008). However, as a smaller mesh size may increase FE accuracy, an additional model was developed with 0.50 mm global, and 0.20 mm local meshes, to compare to the effectiveness of the larger mesh.

To apply subject-specific bone material properties to the model, the ulnar bone mesh and original micro-CT files were imported into custom-written MapFE software (Robarts Research, London, Ontario). Using the density-modulus relationship developed by Austman *et al.* (2009), and provided in Equation 8, this software assigned an elastic modulus (E) to each voxel based on the associated attenuation coefficients in the original micro-CT scans. The mesh was then imported back into Abaqus®.

$$E = 8346(\rho_{\text{density}})^{1.5} \quad \text{Equation 8}$$

Where: E = elastic modulus (MPa)

ρ_{density} = apparent density (g/cm^3)

Homogeneous material properties were applied to both the implant stem and bone cement. According to the manufacturer's product guidelines, the Wright E-centrix® implant stem was made of titanium with an elastic modulus of 110 GPa. Based on

experimental results, determined from cement samples prepared concurrently with the specimen and tested in bending (Appendix 9), an elastic modulus of 2.1 GPa was calculated for the bone cement. Poisson's ratio was valued at 0.3 for all materials, in accordance with values reported in the literature (Mann *et al.*, 1991, 1995; Wheeler *et al.*, 1997).

Mirroring the experimental setup for bending loads only, a 20 N force was applied to the distal tip of the implant head, and the proximal bone surface was fully constrained. In the bonded model, the stem-cement interface was represented as a single surface of nodes, thereby creating a perfect bond. However, in the debonded model, the cement-implant interface was modeled separately for each surface. A detailed developmental methodology is available in Appendix 15.

In consistence with the frictional interaction determined by previous femoral studies, a Coulomb frictional model was selected for the debonded implant-cement interface. In Abaqus®, Coulomb interface friction (Equation 5 - Equation 7) is represented using the penalty interaction. In this case, the coefficient of friction and maximum elastic slip may be defined by the user; however, the shear stress and stress normal to the interface are calculated for each element by the software. The current debonded models were developed with a 0.25 frictional coefficient, as recommended in previous studies for a smooth femoral stem-cement debonded interface (Mann *et al.*, 1991). The maximum elastic slip rate was varied from the standard 0.5% to 1.0%, in order to determine its impact of the resulting strains. A model with a higher coefficient of friction of 0.85 was also developed to account for the roughened ulnar implant.

To compare the results obtained from the finite element model to those determined experimentally, the average maximum principal strain for each of the “gauge regions” was determined. The root mean squared errors (RMSE) were calculated between the model and experimental results for each gauge as a measure of error magnitude, and Bland-Altman plots were constructed to detect systemic errors or bias in the results.

4.3 Results

The large (0.75 global, 0.30 local) and small (0.50 global, 0.20 local) mesh sizes were compared through a quantitative comparison of the microstrain at all internal and external gauges in both bonded and debonded scenarios. When the debonded scenario was tested with a Coulomb friction interaction (0.25 coefficient of friction, and 0.5% slip) and small mesh size, it required a processor with 260 GB random access memory (RAM) to run. Due to the heavy computational requirements, Abaqus® technical support ran the small mesh debonded model, and returned the results for analysis. All other models were run in-house. Similar strain outputs were noted for both the bonded and debonded models, indicating that use of the larger mesh was reasonable (Figure 4.1).

A comparison between finite element and experimental results is depicted in Figure 4.2, associated root mean square errors listed in Table 4.3, and Bland-Altman plots displayed in Figure 4.3. The internal strain gauges were successfully incorporated into the bonded model (RMSE 19.3 $\mu\epsilon$).

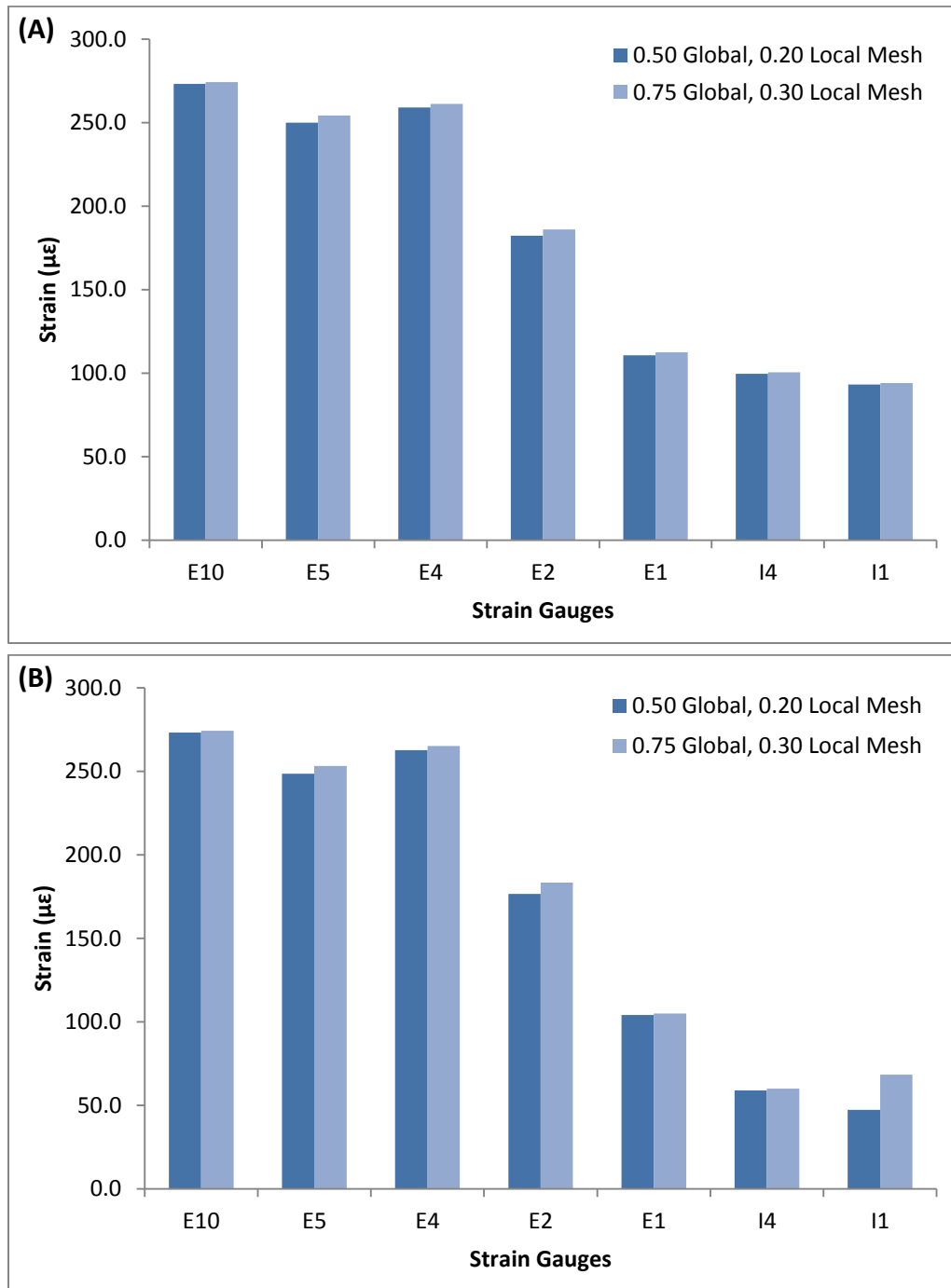


Figure 4.1: Strain output using large and small meshes

Comparison of microstrain output at both internal and external gauge output locations for the large (0.75 global, 0.30 local) and small (0.50 global, 0.20 local) meshes. Results were compared in both the, **(A)** bonded model, and **(B)** debonded model using a Coulomb friction interaction with a 0.25 coefficient of friction and 0.5% slip.

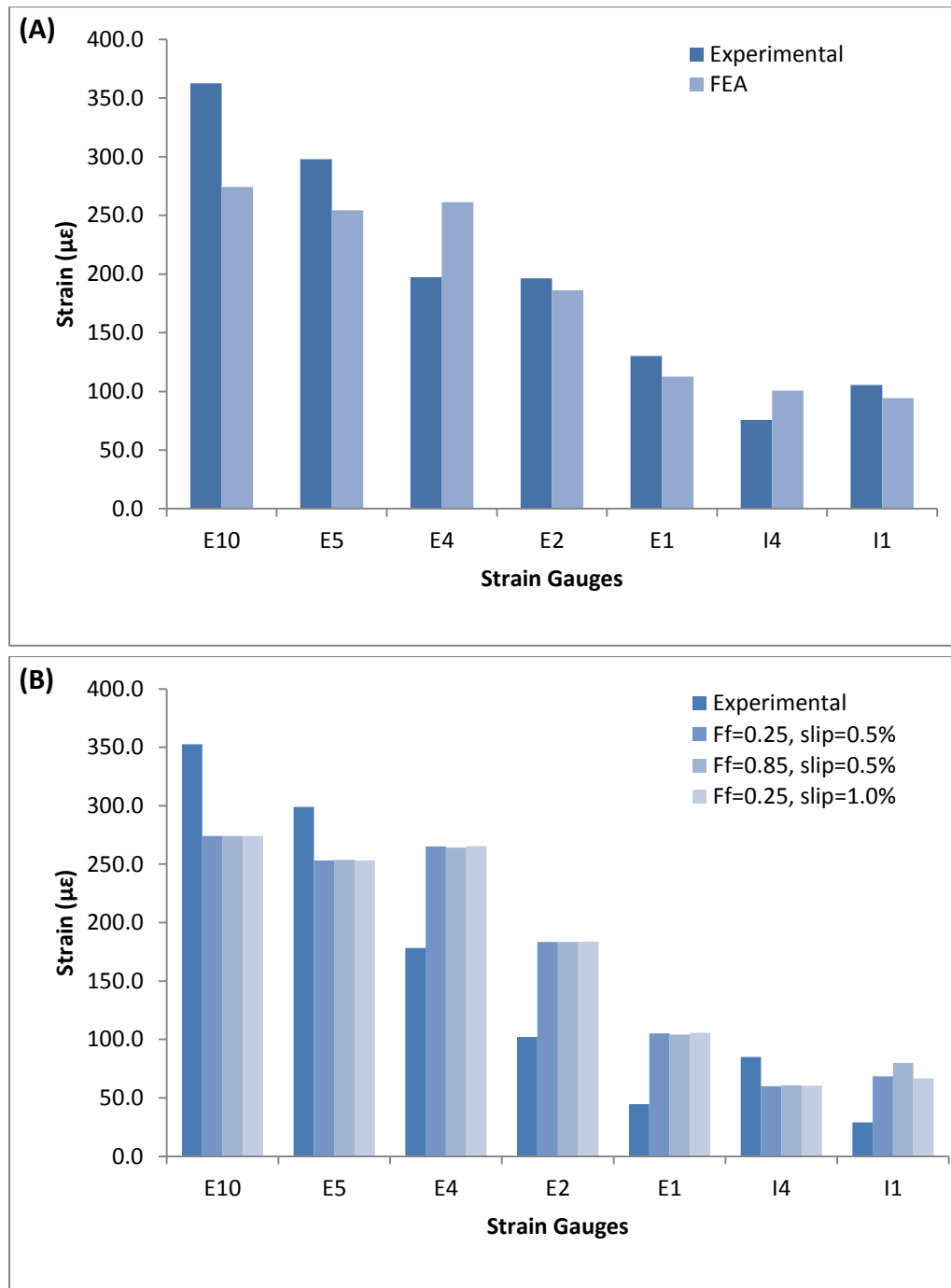


Figure 4.2: Strain output of experimental and FE models

Microstrain output for (A) bonded, and (B) debonded data. The bars within each grouping represent the experimental and finite element data. Multiple debonded interface conditions are represented, including modifications to the interaction property, friction coefficient (F_f), and slip.

Table 4.3: RMSE for bonded and debonded conditions

The root mean squared error between experimental and finite element strains all of internal and external gauges, and average RMSE for each bonding scenario are listed.

Bonding Scenario	Interface Characteristics	Gauges		
		External ($\mu\epsilon$)	Internal ($\mu\epsilon$)	All ($\mu\epsilon$)
Bonded	NA	53.3	19.3	46.2
Debonded	Coulomb ($F_f=0.25$, slip=0.5%)	72.2	33.0	63.5
	Coulomb ($F_f=0.85$, slip=0.5%)	71.8	39.8	64.3
	Coulomb ($F_f=0.25$, slip=1.0%)	72.5	31.7	63.5

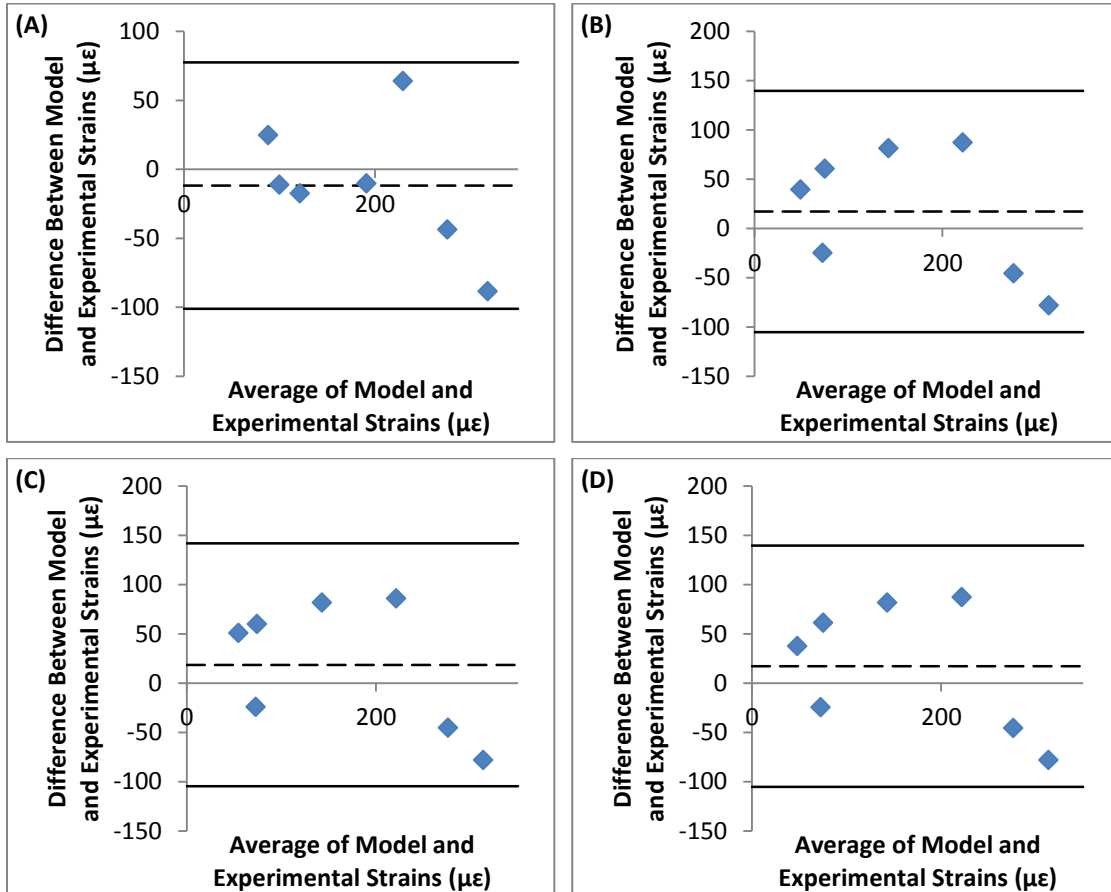


Figure 4.3: Bland-Altman plots for each interface condition

Bland-Altman plots for model outputs compared to experimental strains, for each interface condition. **(A)** bonded, debonded Coulomb interaction with **(B)** frictional coefficient of 0.25 and 0.5% slip, **(C)** frictional coefficient of 0.85 and 0.5% slip, and **(D)** frictional coefficient of 0.25 and 1.0% slip. The mean difference (dashed line) and confidence intervals of two standard deviation (solid lines) are displayed.

RMSE was relatively static between debonded interface conditions for the entire gauge set; however, slight variations were recorded for the internal and external gauges. The Bland-Altman plots were also relatively consistent between debonded interface conditions; however, a marginally lower standard deviation of $61.20 \mu\epsilon$ was recorded when a 0.25 frictional coefficient and 0.5% slip were used.

4.4 Discussion

The development of a subject specific finite element model requires care during multiple steps of the development process to ensure the accuracy of the final simulation. Optimally, a convergence study may be conducted to determine the most favorable mesh where the model is constructed using repeatedly smaller meshes until the change in the resultant strain energy is below 5% for all gauge locations. However, as the inhomogeneous material application to the bone and the computation of smaller mesh sizes both required outsourcing, a complete convergence study could not be conducted. However, in applying the mesh to the model, large (0.75 mm global, 0.30 mm local) and small (0.75 mm global, 0.30 mm local) elements were applied and tested in bonded and debonded (Coulomb friction, 0.25 coefficient of friction, and 0.5% slip) conditions to verify model functionality. At all internal and external gauge locations, marginal changes in strain were noted between mesh sizes, with the exception of the debonded internal-distal gauge, where a slight increase in strain was recorded in the larger mesh. However, in incorporating nonlinearity into the model through debonding the cement-stem interface, the computational requirements significantly increase, such that Abaqus® technical support recommended a processor with greater than 260 GB of

random access memory (RAM) to operate the model within an acceptable timeframe, and as a result, the model could not be run in-house. As the inconsistency was small and isolated to the distal-interior gauge and the available processors were unable to meet RAM requirements, the large mesh was utilized for further assessments.

Previous findings by Austman *et al.* (2009) indicated that the utilization of the density-modulus relationship provided in Equation 8 would offer superior correlation to experimental results, as compared to other equations available in the literature. Based on the Bland-Altman plots, the bias error is equivalent, and confidence interval marginally larger than that found by Austman *et al.* (2009). The average RMSE determined for the external gauges in the bonded model (53.3 $\mu\epsilon$) is slightly higher than the average RMSE expected for this equation, but within the specimen range (6.7 – 60.3 $\mu\epsilon$) noted by Austman *et al.* (2009). The increased confidence interval and RMSE may be attributed to the external proximal (E10) and middle (E4) strain gauges, which displayed higher deviation between model and experimental values. The external proximal deviation may result from inconsistencies in this region of the cadaver bone (such as microcracks), which may not have been completely imaged by the micro-CT, thereby resulting in the improper assignment of material properties. In addition, the variation in strain at the external-middle gauge (E4) may be attributed to inconsistencies in the cement or bone in this transitional region around the distal tip of the implant.

Through cement segmentation and isolation of the nodes at the internal strain gauge locations, the embedded strain gauges were successfully incorporated into the bonded

model. The small root mean squared error of $19.3 \mu\epsilon$ indicates that the model is able to accurately simulate the experimentally determined internal strain response.

Previous studies conducted on the distal femur have investigated the effect of implant-cement debonding on the strains in the surrounding cement and bone (Mann *et al.*, 1991, 1995; Verdonschot and Huiskes, 1996; Wheeler *et al.*, 1997; Nuño and Amabili, 2002). These studies utilized simplified stem geometries without significant external variants in the stem surface (*e.g.*, fluting, grooves, etc.), and suggest that when loads are applied parallel to the long axis of the femur, the debonded interface may be represented as a Coulomb frictional interaction. Coefficients of friction between 0.25-0.35 were determined to optimally recreate the debonded response in these scenarios (Mann *et al.*, 1991).

Utilization of the Coulomb interaction to model the debonded and fluted distal ulnar stem-cement interface in bending did not induce the same change in strain observed between experimentally bonded and debonded scenarios. Though variations in the frictional coefficient and maximum elastic slip rate were trialed, they induced minimal deviations in calculated strain. When the frictional coefficient was increased to better simulate the roughened implant stem, the RMSE and standard deviation (Bland-Altman plots) also increased. Based on these results, Coulomb frictional interactions may not be the best representation of the complex bonding scenario present at the distal ulnar implant-cement interface.

As has been done by others, this study employed Coulomb friction. Other friction models, such as Lagrange interaction, are available in Abaqus®. The Lagrange

interaction prevents any motion between contact surfaces; as opposed to the Coulomb (penalty) interaction, which only limited motion between surfaces to the user defined elastic slip. The Lagrange interaction was trialed in the current study, but the run did not complete due to lack of computational power. Future studies are required to determine whether such modifications to the interaction properties will better predict debonded strains.

In summation, despite the computational limitations of the current study, this finite element methodology effectively incorporates and validates areas of internal strain measurement into a specimen specific distal ulnar model. It was also determined that the Coulomb frictional interaction previously validated for the femoral stem-cement interface, was inapplicable to the distal ulna. Further studies are needed to examine alternate frictional interactions in order to successfully replicate debonded experimental results in a finite element model.

4.5 References

- Austman, R.L., Milner, J.S., Holdsworth, D.W., Dunning, C.E., 2008. The effect of the density-modulus relationship selected to apply material properties in a finite element model of long bone. *Journal of Biomechanics* 41, 3171–3176.
- Austman, R.L., Milner, J.S., Holdsworth, D.W., Dunning, C.E., 2009. Development of a customized density–modulus relationship for use in subject-specific finite element models of the ulna. *Proceedings of the Institution of Mechanical Engineers, Part H: Journal of Engineering in Medicine* 223, 787–794.
- Mann, K.A., Bartel, D.L., Wright, T.M., Burstein, a H., 1995. Coulomb frictional interfaces in modeling cemented total hip replacements: a more realistic model. *Journal of Biomechanics* 28, 1067–1078.

- Mann, K.A., Bartel, D.L., Wright, T.M., Inghraffa, a R., 1991. Mechanical characteristics of the stem-cement interface. *Journal of Orthopaedic Research : official publication of the Orthopaedic Research Society* 9, 798–808.
- Nuño, N., Amabili, M., 2002. Modelling debonded stem-cement interface for hip implants: effect of residual stresses. *Clinical Biomechanics* 17, 41–48.
- Ramaniraka, N.A., Rakotomanana, L.R., 2000. Roughness of the cement-bone surface. *The Journal of Bone and Joint Surgery* 82B, 297–303.
- Verdonschot, N., Huiskes, R., 1996. Mechanical effects of stem cement interface characteristics in total hip replacement. *Clinical Orthopaedics and Related Research* 329, 326–336.
- Wheeler, J.P.G., Miles, A.W., Clift, S.E., 1997. The influence of the stem-cement interface in total hip replacement--a comparison of experimental and finite element approaches. *Proceedings of the Institution of Mechanical Engineers, Part H: Journal of Engineering in Medicine* 211, 181–186.

Chapter 5 - Summary and Conclusions

***OVERVIEW:** This chapter provides a summary of the research findings, and reexamines the original objective and hypothesis as outlined in Chapter 1. The strengths and limitations of the studies are reviewed and potential areas of further enquiry and continued research addressed.*

5.1 Summary

Arthroplasty can provide a viable treatment option for otherwise painful and debilitating disorders of the distal radioulnar joint (DRUJ). As this is a relatively new procedure, current knowledge related to the transfer of load through the implant and its surroundings is limited, but has been hypothesized to be impacted by the degree of bonding at the cement-implant interface. As such, the objective of this body of work was to improve understanding of the role of the implant-cement interface conditions on strains in the cement mantle and ultimately their impact on stress shielding and implant loosening.

Development of a strain gauge embedment methodology was the subject of Chapter 2. A bonding method was established that utilized Simplex P[®] to adhere strain gauges a set distance from the implant stem, prior to embedment within a cement mantle. The functionality of the embedded gauge was determined by examining the drift, linearity,

hysteresis, and repeatability of the gauge output, as well as, visually inspecting the cement bond. Once thermal equilibrium was reached, the gauge was determined to have minimal drift, a linear and repeatable response, and no visually evident cement defects at or around the embedded gauge. This confirms the initial hypothesis, that strain gauges embedded using the bonded methodologies are more functional than those implanted via wafer embedment methods.

Using the gauge embedment methodology outlined in Chapter 2 and a previously developed technique to adhere strain gauges to bone, Chapter 3 examined the impact of cement-stem debonding on strain transfer under multiple loading conditions. Bending loads (5-30 N), torsional (0.025-0.15 Nm), and combined (5-30 N bending loads and 0.025-0.15 Nm torsion) moments, were used to determine the impact of strains at discrete locations within the cement and on the bone. Under bending and combined loading, variations in bonding conditions at the implant-cement interface did not influence internal or proximal-external strains. External distal strains on the bone surface were decreased with debonding of the implant-cement interface. In torsion, decreases in strain under interface debonding were observed at all loads in the proximal cement mantle and distal ulna; however, at higher torsional loads, a decrease in strain was also noted in the bone directly exterior to the proximal end of the stem. This, in part, confirms the second hypothesis, that debonding at the implant-cement interface will not affect strains on the proximal surface of the bone, and disproves it, in that debonding at the implant-cement interface decreases both cement and bone strains surrounding the implant.

The next step of this research was to advance a previously developed distal ulnar model (Austman *et al.*, 2009), to incorporate strains within the cement mantle, and to determine if a debonded distal ulnar cement-implant interface may be modeled via a Coulomb frictional interaction. Using a micro-CT and commercially available software, a model was developed of one of the distal ulna (specimen number 09-12057) tested in Chapter 3. The gauge locations were located on the model and bonded and debonded simulations were run at 20 N bending loads. In the debonded simulations, a Coulomb frictional interaction was applied to the implant-cement interface. The internal strain gauges were successfully applied and validated in the distal ulnar model. However, the Coulomb frictional interaction was determined inappropriate in representing the complex cement-stem debonded interface. This partially confirms the final hypothesis, in that finite element results do agree with experimental results for the bonded model. However, the hypothesis is also partially refuted, as agreement was not reached between the finite element and experimental debonded strains, most likely due to the inefficiency of the Coulomb frictional interaction in modeling the debonded cement-implant interface.

5.2 Strengths and Limitations

Study strengths and limitations have already been addressed in their associated chapters; however, additional details and general themes remain to be discussed. The most significant limitations derive from restrictions in the accurate representation of the subject population, and *in vivo* loading conditions. The use of cadaveric specimens, as representative of *in vivo* conditions is limited. Furthermore all specimens were male,

and elderly (mean age 71 years). Since distal ulnar replacements are frequently conducted in the elderly, this may be considered representative of the patient population. However, care should be taken in when applying these results to female, young, or active patients.

Additional limitations were present due to simplifications in loading protocol. With the testing setup employed, the proximal ulna was assumed to be fully secured and all loading was performed in the neutral position. In reality, loading would occur throughout the arc of forearm rotation. Furthermore, the applied loads were drawn from the literature, but represent unresisted forearm motion. Loads borne by the ulna during more strenuous activities would be expected to be much larger. However, by restricting the protocol to known load values, overrepresentation of the impact of debonding and potential Type II errors are avoided.

It is possible that the wires from the embedded strain gauges produced a reinforcing effect in the cement mantle. In the experimental setup, the lead wires are threaded through the cement mantle of the specimen, and exit through a proximal hole in the bone. A proximal exit point was selected to avoid compromising the implant collar-cadaver bone contact. However, the presence of lead wires throughout the cement mantle could reinforce the construct, thereby, reducing the strain response. To mitigate this error, thin diameter wires were used and spread throughout the mantle, as recommended by Little *et al.* (1990).

Although this study addressed changes in bone strain, these values are only applicable immediately after debonding. *In vivo*, bone is capable of remodeling to accommodate

applied loads, with bone resorption occurring in areas of low strain, and growth in higher strain regions. Over time it would be expected that the material properties of the bone and, therefore, the strain values would change. Such variation would be particularly evident in the distal region where the greatest deviations in strain were noted.

The final issue pertaining to the studies' results is the variance between clinical and statistical relevance. The impact of variations in load on crack formation within bone cement *in vivo*, and bone remodeling is currently unknown. As such, the presence of increased strain during the bonding scenario does not necessarily imply that damage may be induced to the cement mantle and, reduced bone loading post, cement-stem debonding, does not necessarily imply clinically significant bone resorption. Likewise, the inverse may be true where the absence of statistical significance may not correlate with the absence of clinical significance. As such, caution must be taken when interpreting the statistical significance of data.

5.3 Future Directions

The research conducted throughout this thesis has provided a fundamental understanding of the impact distal ulnar cement-stem interface conditions have on strain in the surrounding cement and bone. However, there are still multiple areas of interest relating to the impact of varying interface conditions. As well, the preliminary research, including the development of a functional gauge embedment technique, lends itself to potential future work.

For the purpose of this study, internal strains were measured on the lateral cement mantle. However, previous femoral studies have found variations in strain in different implant planes (Crowninshield and Tolbert, 1983). Further research examining strains in different planes, locations, alternate forearm positions (*i.e.* supination and pronation), and with different interface properties (*i.e.* partial bond, friction, etc.), would further increase understanding of the impact of cement-stem interface conditions on strains in the surrounding cement and ulna.

A finite element model was adapted to incorporate strains within the cement mantle; however, there are still opportunities for further development. Continued testing and validation of alternate contact properties is necessary to expand the applicability of the model to incorporate debonded distal ulnar implants. Furthermore, a model capable of simulating debonded scenarios could be adapted to incorporate various cement-stem interface conditions, and be used in determining the impact of multiple implant interface characteristics on debonding.

In addition to furthering research concerning implant-cement interface conditions, the gauge embedment technique and finite element model could also be utilized to study the impact of various implant designs on strains within the cement mantle. Commercial implants currently use a fluted and tapered stem with a roughened finish. However, future research could be conducted to determine the impact alternate stem topologies and surface finishes have on implant debonding, and strain optimization within the cement mantle.

5.4 Overall Significance

In conclusion, this work has contributed to the knowledge of strain distribution both within the cement mantle and surrounding distal ulna as a function of bonded versus debonded cement-stem interface conditions. Furthermore, an experimental strain gauge embedment technique and finite element model has been developed that may be utilized in a variety of future studies, both in continuing research regarding the cement-stem interface, and in studying implant design characteristics. It is hoped that information garnered through this thesis may be used to optimize the design of distal ulnar implants, thereby reducing the need for replacement through costly and painful revision surgeries.

5.5 References

- Austman, R.L., Milner, J.S., Holdsworth, D.W., Dunning, C.E., 2009. Development of a customized density–modulus relationship for use in subject-specific finite element models of the ulna. *Proceedings of the Institution of Mechanical Engineers, Part H: Journal of Engineering in Medicine* 223, 787–794.
- Crowninshield, R.D., Tolbert, J.R., 1983. Cemented strain measurement surrounding loose and well-fixed femoral component stems. *Journal of Biomedical Materials Research* 17, 819–828.
- Little, E.G., Tocher, D., Donnell, P.O., 1990. Strain gauge reinforcement of plastics. *Strain* 91–98.

Appendices

Appendix 1 – Glossary of Terms

This appendix contains a definitions of terminology used throughout this thesis to assist the lay reader.

anatomical position – body upright, with arms to the side of the body and palms and hands facing forward

anterior – Situated towards the front of the body

arthroplasty – Surgical joint replacement or reconstruction

attenuation coefficient – degree of reduction in pixel intensity (as it pertains to micro-computed tomography (μ CT) images)

congenital disorders – defects present from birth

coronoid process – a triangular protrusion projecting from the anterior proximal portion of the ulna

cosmesis – the preservation or restoration of the body from disfigurement

distal – situated away from the midline of the body along a limb

ectopic calcification – the depositing of calcium salts on tissue

femur – the most proximal bone in the leg, articulates with the tibia distally (at the knee) and the pelvis proximally (at the hip)

finite elements – small interconnected segments of a larger part, used in FEA

Hounsfield units – an interval of the quantitative scale used in describing radiodensity

humerus – bone located in the upper arm, between the elbow and the shoulder

intramedullary canal – the internal, marrow-filled cavity found in long bones

lateral – located away from the midline of the body

medial – located toward the midline of the body

neutral position – during forearm rotation, the point midway between pronation and supination

node – point at which two or more finite elements meet, used in FEA

posterior – situated towards the back of the body

pronation – rotation of the forearm such that the palm of the hand faces downward

prosthesis – an artificial body part

proximal – situated toward the midline of the body along a limb

radius – one of the two long bones of the forearm (the other being the ulna) between the wrist and elbow, located laterally when in anatomical position

resection – to surgically remove all or part of a tissue, structure, or organ

resorbable – a substance that can be biologically assimilated

rheumatoid arthritis – a chronic and progressive inflammatory disease

sigmoid notch – an indentation on distal radius in which the ulnar head rotates

supination – rotation of the forearm such that the palm of the hand faces upward

stress shielding – a reduction in bone density due to the removal of normal bone stresses

synovial joint – a freely moving joint comprised of articular cartilage covered bony surfaces surrounded by lubricating synovial fluid contained within a joint capsule

synovitis – synovial membrane inflammation

ulna – one of the two long bones of the forearm (the other being the radius) between the wrist and elbow, located medially when in anatomical position; articulates with the humerus proximally (at the elbow) and the radius distally

Appendix 2 – Preliminary Testing of Gauge Carrier for Internal Strain Gauge Embedment

The following pilot trials were performed to determine the feasibility of using strain gauges encapsulated in a cement carrier prior to internal gauge embedment. The proposed method would encompassed a strain gauge in a thin wafer of cement and utilize the wafer to stabilize the gauge during implantation.

Trial 1 – Wafer Formation

Three methods of wafer formation were trialed utilizing Denstone® (Modern Materials, Niagara-on-the-Lake, ON, Canada) as a cementing medium and five simulated gauges per group. Simulated gauges were comprised of a thin layer of cellulose tape cut to 1 cm square with two 3 x 0.3 cm strands left on one side to simulate the gauge wires.

Method 1: Using a folded plastic gauge cover, fill the cover with semi-solid Denstone®, and centralize the simulated gauge within the cement. Compress the cover utilizing a heavy weight. Allow to cure for 5 min, when cured remove the gauge cover as well as any excess cement. Allow to air dry until the cement is fully hardened.

Results – The cover was difficult to remove resulting in fracturing of the cement and increased pressure on the wires. Due to cement damage no valid wafers were formed.

Method 2: Using two 3x3 cm pieces of LDPE and a small quantity (approximately 3 mL) of semi-solid Denstone[®], layer the materials as LDPE-Denstone[®]-simulated gauge-Denstone[®]-LDPE. Compress the construct using a heavy weight. Allow to cure for 5 min, when cured peel off the LDPE and remove excess cement as required. Allow to air dry until the cement is fully hardened.

Results – The LDPE sheets were easily separated from the Denstone[®]; however, the wafers formed using this method displayed an irregular geometry and the cement covering the simulated gauges was susceptible to fracture during removal of the excess cement. Wafer thickness was greater than desired in several of the samples (Wafer thickness: 0.96 – 1.26 mm).

Method 3: Paint a smooth layer of Denstone[®] onto each simulated gauge. Using two 3x3 cm pieces of LDPE and a small quantity (approximately 3 mL) of semi-liquid Denstone[®], layer the materials as LDPE-Denstone[®]-simulated gauge-Denstone[®]-LDPE. Compress the construct using a heavy weight. Allow to cure for 5 min, when cured peel off the LDPE and remove excess cement as required.

Results – The LDPE sheets were easily separated from the Denstone[®], and the wafers formed were of an acceptable thickness. An irregular

geometry was noted on all gauges; however the wafer could be cut to desired shape as required (Wafer thickness: 0.5 – 1.0 mm).

Trial 2 – Functionality of Encapsulated Gauge in Denstone®

Methods

The specimen developed in this study was comprised of a Vishay C2A-13-125WW-350 general purpose stacked strain gauge rosette (Vishay Intertechnology Inc., Malvern, Pensylvania, USA) embedded into Denstone® golden cement (Modern Materials, Niagara-on-the-lake, ON, Canada). To prepare and protect the strain gauge rosette prior to implantation, it was encapsulated in a thin wafer of cement utilizing embedment Method 3 as outlined in Trial 1 – Wafer Formation. Throughout the encapsulation process care was taken not to damage the attached wires.

Utilizing a custom designed setup, a hollow cylinder was constructed and the encapsulated gauge was embedded within the cylinder. To properly model the desired geometry, the cylinder was constructed in a three stage process. In the first stage, the lower two thirds of the cylinder were formed by filling the mold with cement and allowing the cement to harden until capable of supporting the gauge. Using tweezers, the strain gauge was carefully pressed into the cement until the top of the gauge was flush. The final stage of the construction process was completed by filling the remaining third of the cylinder mold with cement and allowing one hour to cure. The sample was then carefully removed from the mold and allowed to cure for an additional 23 hours

prior to testing. All Denstone® was prepared using a 5:2 cement to water ratio, and hand mixed for five minutes to ensure product consistency and uniformity.

The strain gauge was wired as a quarter Wheatstone bridge via a NI SCXI 1314 terminal block (National Instruments, Austin, TX) and given +5V DC excitation voltage. Bending loads were applied using an Instron 8872 Fatigue Testing System with 10,000 N load cell (High Wycombe, Bucks, UK). Bending loads between 100 and 1,000 N were applied, and the effects of drift, repeatability, hysteresis, and gauge accuracy examined.

Results

Drift

To determine the magnitude and maximum drift the embedded gauges were balanced and unloaded readings were recorded over a three hour period. A consistent drift to a maximum deviation of 26.4 $\mu\epsilon$ was noted over the first two hours. However, the drift stabilized, with an increase in drift to a maximum of 1.9 $\mu\epsilon$ (standard deviation 3.2 $\mu\epsilon$) between two and three hours.

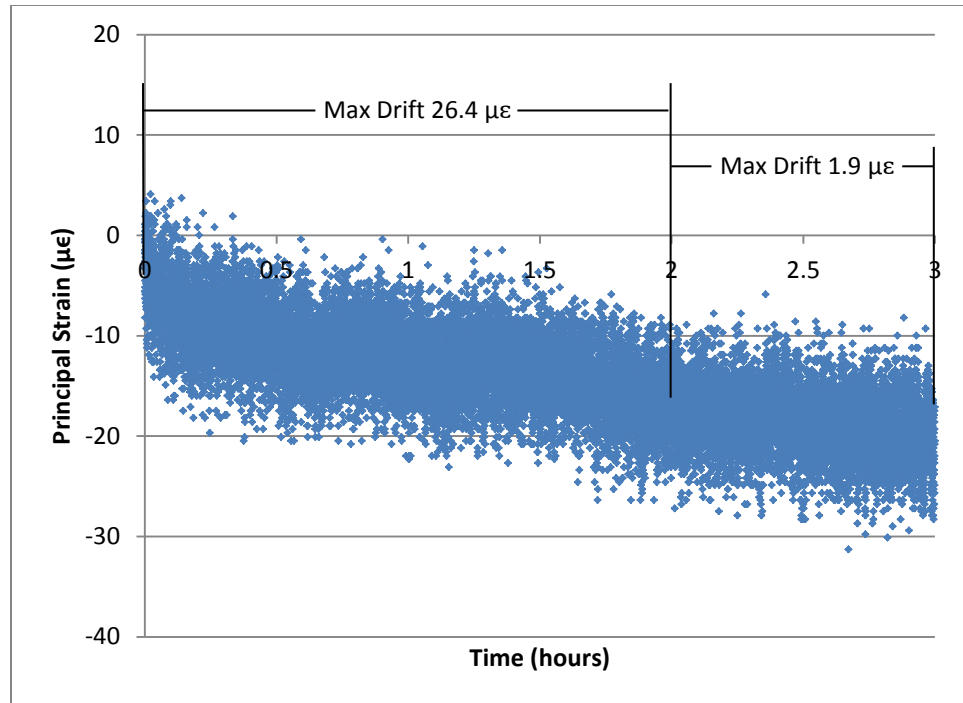


Figure A.1: Drift of an encapsulated strain gauge

Principal strain for a triaxial rosette embedded in Denstone®, recorded over a three hour period with a maximum drift of 26.4 $\mu\epsilon$ over the first two hours and a subsequent drift of 1.9 $\mu\epsilon$ (standard deviation 3.2 $\mu\epsilon$) over the final hour.

Repeatability

Gauge repeatability during bending load application was measured by applying loads of 100 N, 500 N and 1,000 N three times and determining the standard deviation in strain between trials at each load. For all loads the standard deviation in strain was below 0.5 $\mu\epsilon$.

Hysteresis

Hysteresis of the gauge was recorded by generating two sets of linear curves, by increasing and subsequently decreasing the load between zero and 1,000 N over 30 second intervals. At predetermined loads the deviation between these lines was

recorded, and the maximum deviation utilized to quantify the gage's hysteresis. A maximum hysteresis error of $3.23 \mu\epsilon$ was recorded.

Accuracy

Accuracy was determined by recording the gauge outputs at maintained 100 N, 200 N, 500 N, 750 N and 1,000 N loads. The resultant gauge outputs shown in Table A.1 were compared to calculated strain values determined from Instron displacement measurements.

Table A.1: Accuracy of encapsulated gauge throughout load application range

Load	100 N	200 N	500 N	750 N	1,000 N	Average
Error (%)	22.2	29.5	36.3	36.8	39.7	32.9

Discussion and Conclusions

Overall gauge performance regarding repeatability and hysteresis were acceptable given the limitations of the gauge used. The Drift may be a factor of gauge heating during initial activation and may be negated by allowing a 3h heating period prior to testing. The deviation in strain gauge accuracy is predominantly accredited to gauge angulation during embedment. However, this shows a major limitation in the encapsulated embedment methodology, as the wafer susceptible to misalignment during the embedment process. Securing the wafer wires may aid in alleviating the issue.

Trial 3 – Functionality of Encapsulated Gauge in PMMA Bone Cement (Simplex P®)

A triaxial strain gauge (SGD-2/350-RY53, Omega Environmental, Quebec, Canada) was prepared in a thin wafer of bone cement utilizing embedment Method 3 as outlined in Trial 1 – Wafer Formation. Though wafer formation was successful, the edges of the wafer were damaging to the gauge wires. Despite repeated attempts to resolder the gauge wires, the thin Simplex P® wafer edges repeatedly severed the wires during the embedment process resulting in loss of gauge functionality. As a thicker wafer would not be acceptable for future embedment into the cement mantle of an ulnar implant, further testing of gauge carriers was not pursued.

Appendix 3 – Cementing Technique

The following procedure was utilized to cement a gauged distal ulnar implant in a cadaver ulna using Simplex P® bone cement. This procedure was used in Chapters 2 and 3.

- (1) Place one package of Simplex P® bone cement in a refrigeration unit and allow to chill overnight.
- (2) Connect an Optivac® Vacuum Mixing System with long cartridge (Biomet Inc, Warsaw, Indiana USA) to a 15-20 mmHg vacuum pump, and using a funnel to control flow empty one packet of Simplex P® powder into the cartridge.
- (3) Completely empty the accompanying vial of monomer into the cartridge and immediately screw closed the cartridge head.
- (4) Allow 10 seconds for a vacuum to form within the unit. Then move the plunger in a rapid downward-twisting motion to mix the cement. Ensure that the plunger makes full contact with both ends of the unit during mixing and no residual powder is allowed to remain along the bottom. Mix vigorously for 60 seconds.
- (5) Quickly unscrew the cartridge head and pour the fluid cement into a 60 mL syringe.
- (6) Remove excess air from the syringe.

Appendix 4 – Internal Strain Gauge Application Technique

The following procedure was used to affix strain gauges to an implant with 0.5 mm layer of Simplex P® bone cement. This procedure is utilized solely for the adherence of the internal strain gauges.

Before beginning, prepare a gauging baseplate (Figure A.2) capable of orienting the implant in the desired position.

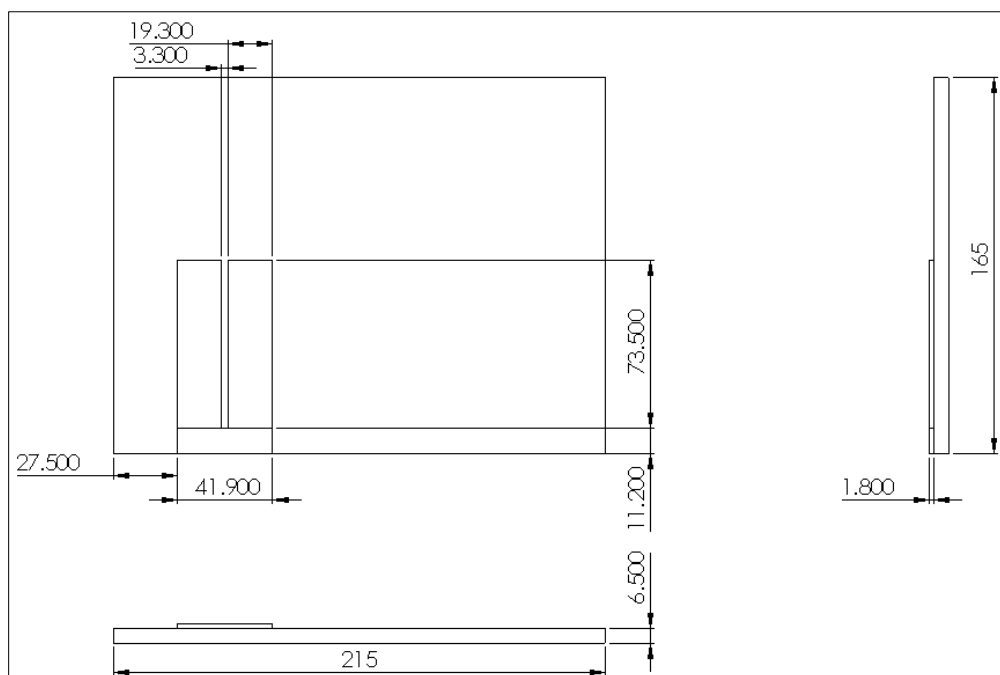


Figure A.2: Gauging baseplate

The detailed and dimensioned drawing of the gauging baseplate used for implant alignment and gauge fixation was created in Solidworks (Dassault Systemes, Concord, Massachusetts, USA). The base was machined from stainless steel and details constructed from adhesive backed paper. All dimensions are in millimeters.

Create a torque limiter to prevent implant rotation, a 0.5 mm thick polymer clay mold with cutouts 1 mm larger than the gauge at the desired gauge locations, and a compression tool with cutout depths equal to the desired cement thickness plus the thickness of the gauge. These tools are displayed in Figure A.3.

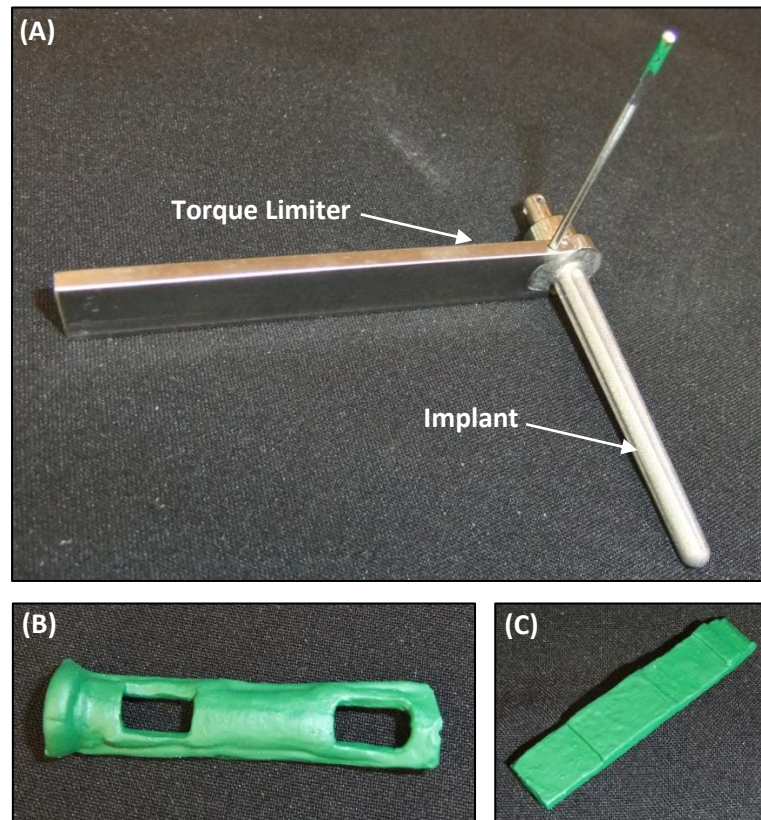


Figure A.3: Required tools for strain gauge fixation

Tools necessary to affix a strain gauge to an implant stem with a 0.5 mm layer of Simplex P[®] bone cement: (A) torque limiter affixed to implant, (B) polymer clay mold, and (C) compression tool

- (1) Gently sand the back of the gauges with 400 grit sandpaper, and wipe with a clean cotton swab to remove particulate.
- (2) Clean the surface of the implant with acetone, rinse with water and pat dry with paper towel.

- (3) Attach the torque limiter to the implant as shown in Figure A.3(A). Using a permanent marker and a caliper mark the desired gauge locations on the implant.
- (4) Orient the implant via the torque limiter in the baseplate notch and align the gauges to the desired gauge locations. Secure the gauge wires to fix the gauges in the desired locations and remove the implant. Take care not to disturb the gauge alignment during implant removal.
- (5) Place the mold onto the implant ensuring that there is a snug fit between the implant and the mold, some positioning may be required.
- (6) Vacuum mix chilled Simplex P[®] bone cement at a pressure between 15-20 mmHg allowing 10 seconds after closing the vacuum mixing chamber for a vacuum to form. Mix vigorously for one minute using a plunging and rotational movement.
- (7) Pour the cement into a syringe and wait until the cement becomes viscous (20-30 sec).
- (8) Using viscous Simplex P[®] bone cement fill the voids in the polymer mold until level with mold.
- (9) When the cement becomes tacky quickly remove the mold and return the implant to its outlined position on the template. Using the compression tool press the gauges down onto the implant, take care that excess cement does not interfere with the positioning of the compression tool.
- (10) Remove excess cement from the implant, wires and gauging tools.
- (11) Validate that gauge functionality and adherence to the implant.

Appendix 5 – Strain Data Collection Program

The front panel of the LabVIEW program written and utilized to collect the strain, load, and displacement data for the experimental studies outlined in Chapters 2 and 3 is shown in Figure A.4. The programming details are shown in Figure A.5.

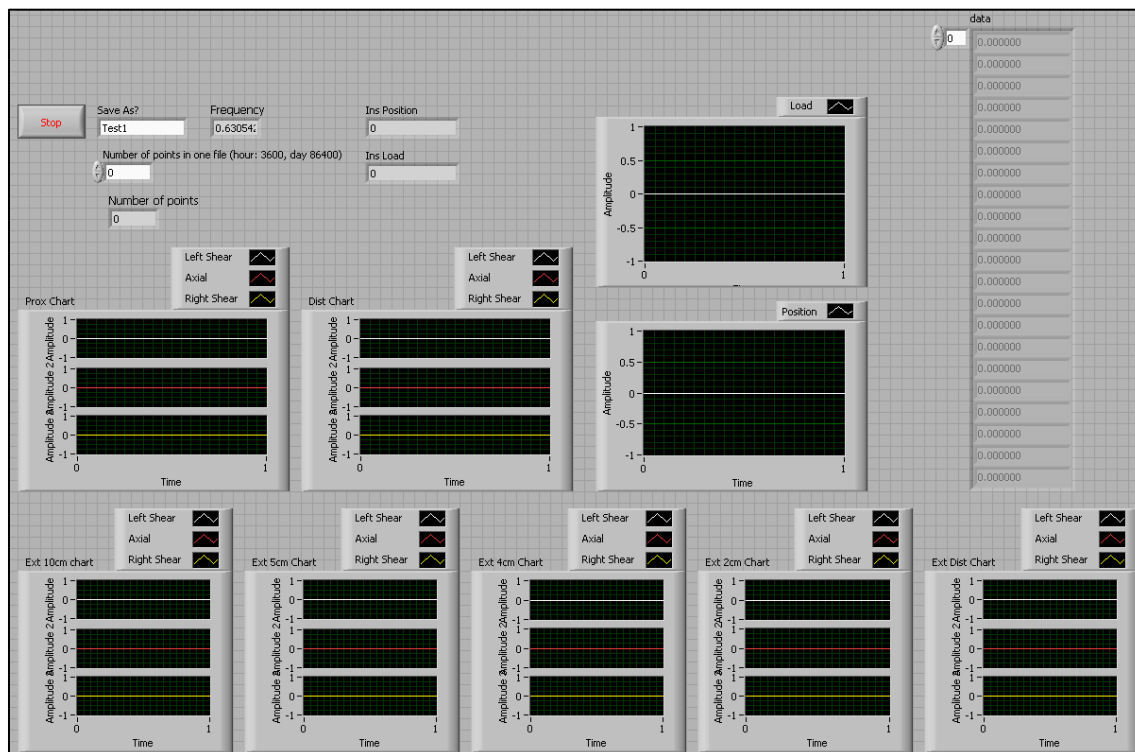


Figure A.4: LabVIEW program front panel

This custom designed LabVIEW program was utilized for strain, load, and displacement data collection

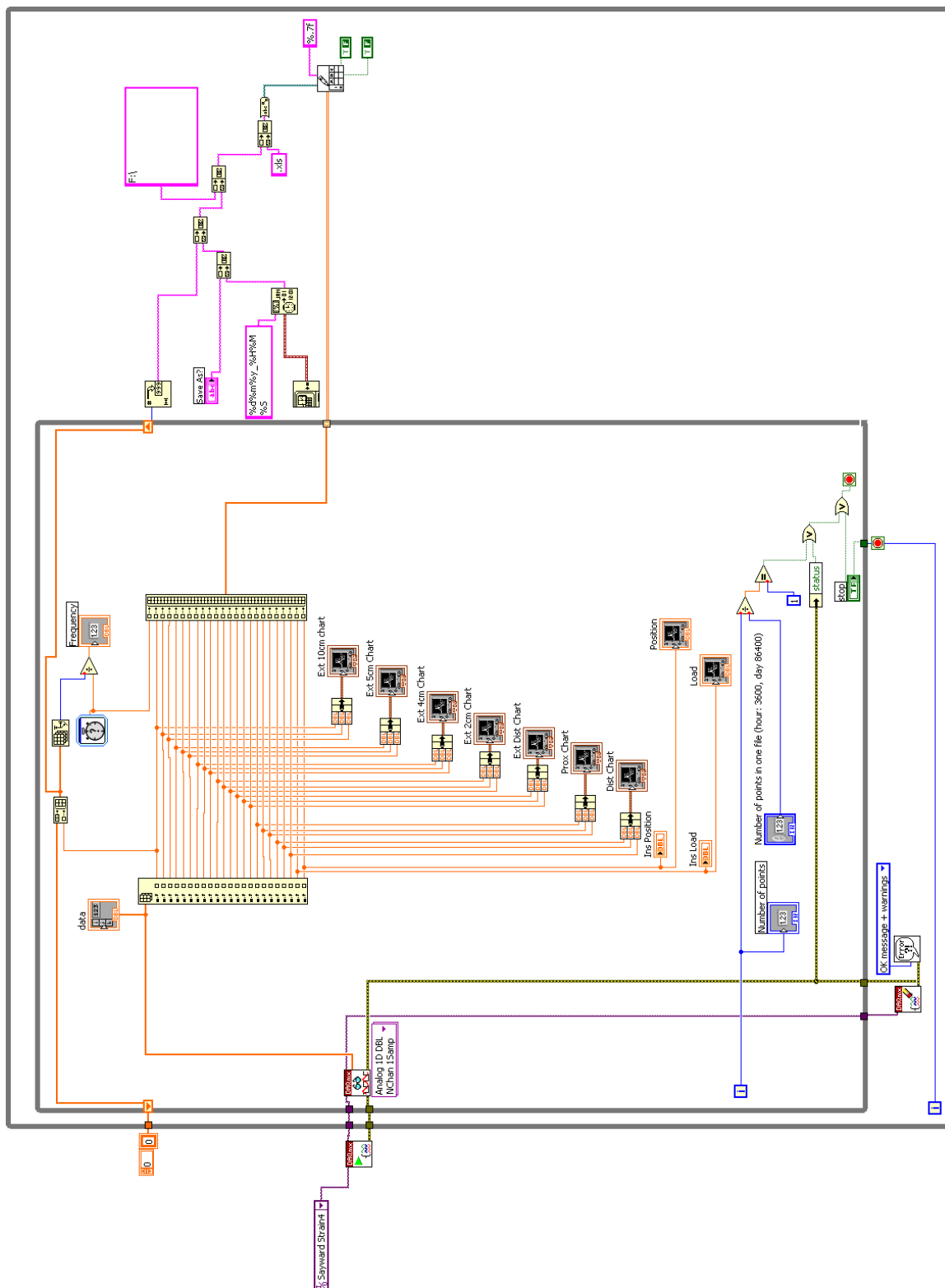


Figure A.5: LabVIEW program back panel

This custom designed LabVIEW program was utilized for strain, load, and displacement data collection

Appendix 6 – Gauge Embedment Pilot Study Strain Data

This appendix contains the tabulated and graphically represented processed strain data that was presented in summation in Chapter 2. The strain values are presented in units of microstrain ($\mu\epsilon$), and load values in newton (N).

Hysteresis

Table A.2: Hysteresis for strain gauge embedment pilot study

Load (N)	Increasing ($\mu\epsilon$)	Decreasing ($\mu\epsilon$)	Difference ($\mu\epsilon$)
5	10.58	10.37	0.21
10	18.26	20.01	1.75
15	31.45	31.17	0.28
20	40.04	42.49	2.45
25	51.17	53.74	2.57
30	62.86	60.38	2.48
<i>Average</i>			1.62
<i>Max</i>			2.57

Repeatability and Linearity

Table A.3: Average recorded principal strain by load and testing day

Load (N)	Day 1 ($\mu\epsilon$)	Day 2 ($\mu\epsilon$)	Day 7 ($\mu\epsilon$)
5	9.66	11.19	8.51
10	20.07	21.08	19.04
15	29.51	29.45	30.70
20	39.82	39.17	42.46
25	50.36	47.21	52.30
30	60.95	57.00	61.73

Table A.4: Standard deviation of recorded principal strain

Load (N)	Inner Trial Standard Deviation			Inter-trial Standard Deviation (Day 1) ($\mu\epsilon$)	Inter-day Standard Deviation ($\mu\epsilon$)
	Day 1 ($\mu\epsilon$)	Day 2 ($\mu\epsilon$)	Day 7 ($\mu\epsilon$)		
5	3.36	3.41	3.21	0.14	1.10
10	3.42	3.24	3.32	0.67	0.83
15	3.34	3.29	3.50	1.04	0.58
20	3.39	3.40	3.31	0.40	1.42
25	3.36	3.43	3.34	0.85	2.10
30	3.71	3.40	3.49	0.20	2.07
<i>Average</i>	<i>3.43</i>	<i>3.36</i>	<i>3.36</i>	<i>0.55</i>	<i>1.35</i>

Appendix 7 – Detailed Specimen Information

The specimen number, arm, age and functional internal gauges of each experimentally tested ulna are provided. All specimens are from male subjects.

Specimen Number	Arm	Age	Functional Internal Gauges
11-03022	Left	75	I1, I4
10-01004	Left	69	I1, I4
11-03026	Left	79	I1, I4
09-12057	Right	81	I1, I4
09-13055	Right	73	I4
10-06020	Right	57	I1
11-03045	Right	75	I1, I4
11-03057	Right	59	I1, I4

Appendix 8 – Fixture Utilized in the Ulnar Fixation Process

The fixture utilized to pot the proximal portion of each cadaveric ulna in a PVC cylinder, showing the laser level line that was utilized to ensure alignment of the bone with the jig both anterior-posteriorly and medial-laterally.

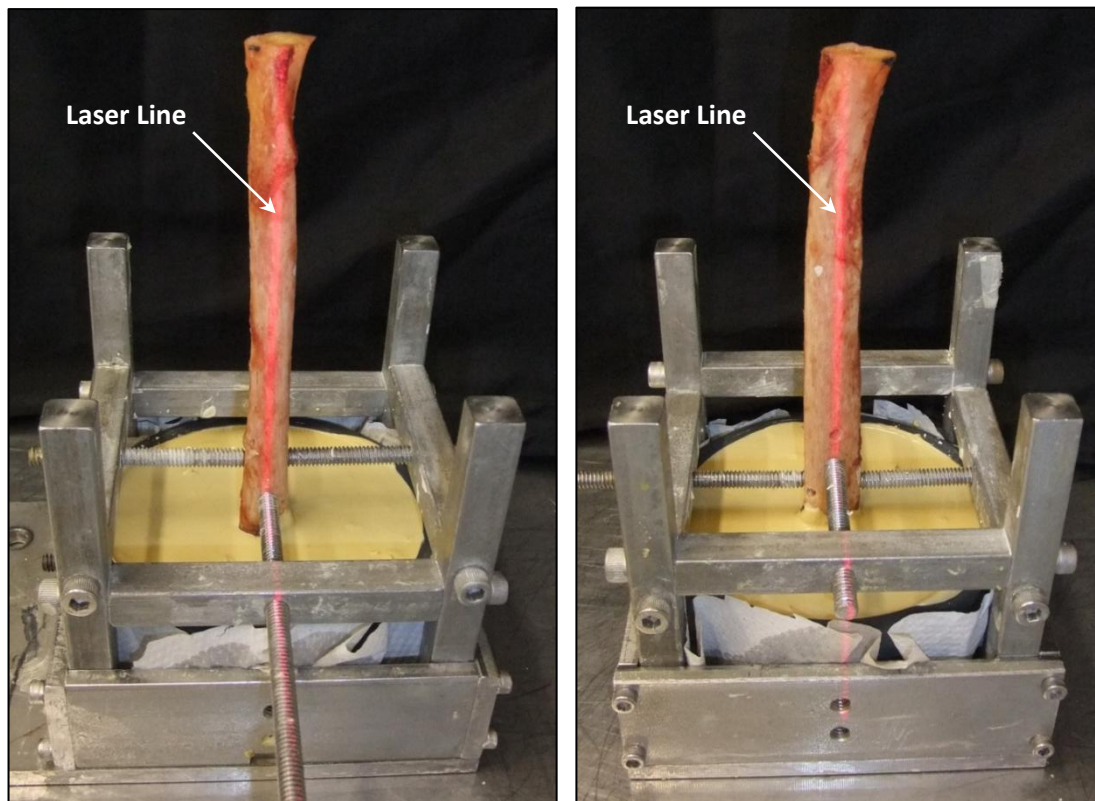


Figure A.6: Specimen number 09-12057 in potting fixture
Fixture utilized for cementing bones into a PVC cylinder with Denstone® cement (Modern Materials, Niagara-on-the-lake, ON, Canada)

Appendix 9 – Cement-Stem Bonded/Debonded Interface Testing Procedure

The following detailed experimental procedure was used in cement-implant interface testing as discussed in Chapters 3. Throughout testing the specimen was kept moist through the application of deionized water. All digitization was accomplished using a MicroScribe® (Revware, San Jose, California) and during testing strain data were recorded via custom LabView software outlined in Appendix 5.

Testing Preparation (Specimen # _____)

Cement

- (1) Place 4 bags of cement in the freezer (3 for testing, 1 backup)

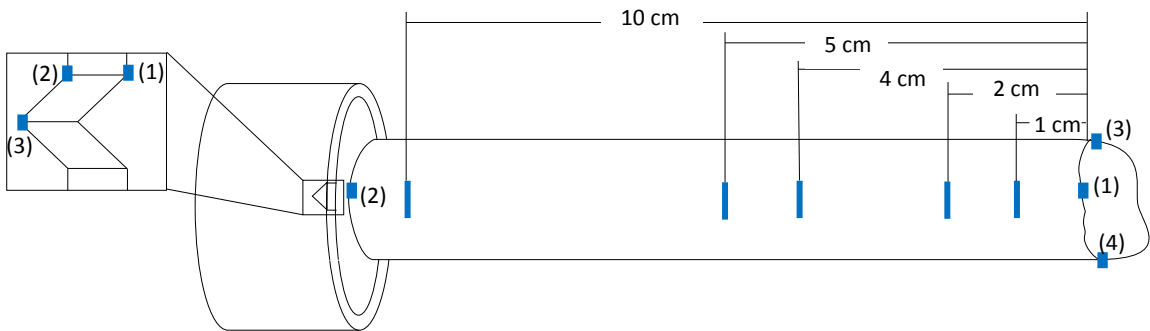
MicroScribe®

- (1) Open “MicroScribe New Bones” Excel program on computer
- (2) Setup MicroScribe®
- (3) Press button to home the MicroScribe® and complete one test point to ensure that the device is working

Specimen

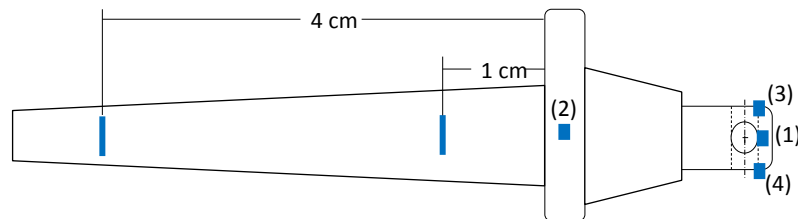
- (1) Select one ulna from the freezer for testing

- (2) Mark the coordinate system and distal gauge ends on the stem (areas to be identified outlined in blue below)



Implant

- (1) Mark the coordinate system and distal gauge ends on the stem (areas to be identified outlined in blue below)



Internal Gauges

- (1) Solder 32 gauge lead wires to the 1" gauge connectors and coat wires in polyurethane
- (2) Verify gauge function
- (3) Using the implant and gauge markings as a guide carefully align the gauges on gauging baseplate
- (4) Verify gauge function
- (5) Verify gauge placement

External Gauges

- (1) Using 30 strand ribbon wire, solder long lead wires to the 1" gauge connectors on 5 gauges and coat wires in polyurethane
- (2) Verify gauge function

Testing (Specimen # _____)

Day 1

- (1) Remove specimen and saline soaked towel from freezer
- (2) Digitize pre-instrumented bone, wrap in saline soaked paper towel
- (3) Digitize Pre-gauged implant
- (4) Cement Gauges on implant as outlined in Appendix 4.
- (5) Allow 20min for the cement to harden.
- (6) Digitize post-gauged implant
- (7) Using a caliper measure gauge depth and width



- (8) Verify internal gauge functionality and wrap the wire ends together with tape
- (9) Thread the internal gauge wires through the bone while supporting the implant to ensure pressure is not placed on the gauge-cement bond. Unwrap the wire ends.
- (10) Using 18 strand ribbon wire, solder long wires to the gauge leads and coat connection in polyurethane. Verify gauge function and leave gauges operational to monitor variations in strain.
- (11) Coat the implant stem in Vaseline and implant head in carnauba wax. Make sure not to get any debonding agent on the gauges or gauge wires.
- (12) Prepare a batch of Simplex P® bone cement, as outlined in Appendix 3.
- (13) Using the cement filled syringe, fill the cadaver bone until cement is level with the distal end and visibly flowing from the wire exit hole. Plunge the ulna with a small diameter (<5 mm) wooden dowel to remove air pockets and refill with bone cement.
- (14) Supporting the gauged implant, gently but firmly direct the implant into the cement filled canal. Maintain consistent pressure on the wires to prevent bunching inside the bone. Monitor the internal gauge response to ensure that the gauges are not compromised in the cementing process.
- (15) If at any point during implant insertion the level of bone cement within the canal decreases, use residual cement in the syringe to fill the canal until it is level with the cut edge of the distal ulna.
- (16) Once the implant is in place and internal gauges verified as operational remove excess cement from the bone and around the implant head.
- (17) Using the same cement batch, form two sample blocks using the custom 10 x 80 mm mold.

- (18) Allow 20 min for the cement to harden.
- (19) Verify gauge function and coat the gauge wires where they exit the bone with M-bond epoxy. Wrap the wires in plastic wrap and secure at both ends with electrical tape.
- (20) Mark around the implant head to denote its starting position and take a photo of the initial implant head orientation.
- (21) Wrap the bone in a saline soaked towel, and plastic wrap. Wrap the two sample cement blocks in paper towel moistened with deionized water. Place entire setup in a plastic bag, with the two sample cement blocks.
- (22) Begin the "Sayward Strain 4.0" LabView program and record variations in strain overnight at 1 Hz.

Day 2

- (23) 24 h after implant embedment, verify internal gauge function
- (24) Bond 5 external gauges to the bone
- (25) Digitize bone and Implant
- (26) Test the **Semi-debonded** implant and record variations in strain at 10 Hz in:
 - Bending
 - Torque_5mm
 - Combined_5mm
- (27) Torque implant to 7° using a 100 mm torque arm (axial displacement of 12.4 mm)
Starting Position = _____ Ending Position = _____
- (28) Take a photo of the implant head orientation.
- (29) Return implant to starting orientation and digitize the debonded implant.
- (30) Test the **debonded** implant and record variations in strain at 10 Hz in:
 - Bending
 - Torque_5mm
 - Combined_5mm
- (31) Using a combination of axial and rotational loading carefully remove the implant.
- (32) Gently remove excess Vaseline from both the stem and canal using rolled paper towel. Use medical files and small drill bits to carefully increase the canal diameter until the implant is able to freely rotate within the canal.
- (33) Return implant to the bone in its starting orientation and digitize implant and bone setup.

- (34) Test the **fully debonded** implant and record variations in strain at 10 Hz in:
- Bending
 - Torque_5mm
 - Combined_5mm
- (35) Implant the stem in the ulna, while monitoring gauge activity and verifying implant orientation using a laser level. Make certain cement does not contact any of the external gauges and excess cement is removed from around the implant head.
- (36) Test the first of the cement samples in bending.
- (37) 20 min post-implant embedment, gently wrap the bone, taking care to avoid the gauges, in paper towel moistened with deionized water. Also wrap the remaining cement block in moistened paper towel. Place specimen and cement block in a plastic bag. Record variations in strain overnight at 1 Hz.

Day 3

- (38) 14-16 h after implant embedment, verify gauge functionality and take a photo of the implant head orientation.
- (39) Test the **bonded** implant and record variations in strain at 10 Hz in:
- Bending
 - Torque_5mm
 - Combined_5mm
- (40) Torque specimen to 7° using a 100 mm torque arm (axial displacement of 12.4 mm)
Starting Position = _____ Ending Position = _____
- (41) Take a photo of the implant head orientation.
- (42) Return implant to starting orientation. Digitize semi-bonded implant.
- (43) Test the **semi-bonded** implant and record variations in strain at 10 Hz in:
- Bending
 - Torque_5mm
 - Combined_5mm
- (44) Using a combination of axial and rotational loading carefully remove the implant.
*Note: **CAUTION!** When the bone fractures the fragments are sharp.*
- (45) Test the second cement sample in bending.
- (46) Clean and sanitize all work surfaces. Dispose of biologic and bio contaminated material in the appropriate manner.

Appendix 10 – Debonding Agent Validation

The following pilot study was used to select and validate the functionality of a cement-implant debonding agent. Testing was performed using cylindrical stemmed implants (8.0 mm diameter) in an 18.8 mm square cement mantle with a cement potting depth of 20.0 mm.

The torsional loads required to debond (rotate a cemented ulnar implant 7°) can be damaging to the surrounding cadaver bone when applied over a short duration. To test the characteristics of a debonded interface it is therefore necessary to compromise the implant-cement interface prior to implant embedment. As such, the purpose of this pilot study is to validate the functionality of several release agents and select the optimal material for inclusion in implant interface conditions testing.

Materials and Methods

A total of six cobalt chrome stemmed implants with a cylindrical cross sectional diameter of 8.0 mm were utilized in this study. Four implants were coated with unique debonding agents: mineral oil (Johnson & Johnson, New Jersey, USA), mold release/conditioner (Castin' Craft, Environmental Technology Inc, Fields Landing, USA), petroleum jelly (Vaseline, New Jersey, USA), or carnauba wax (104 High Temp Mold Release Wax, TR Mold Release, Los Angeles, USA). The fifth implant was coated with both mineral oil and petroleum jelly and the sixth stem tested sans debonding agent.

Using a custom jig, specimens were embedded in a square 18.8 mm vacuum mixed Simplex P[®] bone cement mantle constrained within an aluminum tube. The stem was centralized within the fixture and the cement depth constrained to 20.0 mm via a custom fit Delrin[®] (DuPont, Delaware, U.S) centralizing block.

Specimens were tested in a biaxial materials testing machine (Instron 8872, Canton, MA, USA), and torsional loads applied cyclically from 0-10 Nm at 1 Nm increments, with 100 cycles per increment. Data was collected at 1.5 Hz and debonding (7° rotation) loads recorded. A manual axial stem pullout was used to validate the mobility of the stem post debonding.

Results

Debonding was successfully achieved for the mineral oil, petroleum jelly, carnauba wax and mineral oil/petroleum jelly coated implants. Both the implant coated in mold release/conditioner and the uncoated implant failed to debond. The torsional loads at which interface failure occurred are displayed in Table A.5.

Table A.5: Debonding characteristics of release agent coated implants

Debonding Agent	Torsional load at Debonding (Nm)	Axial Stem Pullout
Mineral Oil	1.27	Failed
Mold Release/Conditioner	>10.00	Failed
Petroleum Jelly	0.43	Successful
Carnauba Wax	0.29	Successful
Mineral Oil/Petroleum Jelly	0.78	Failed
None	>10.00	Failed

Manual axial stem pullout was successful in the petroleum jelly, and carnauba wax coated stems, with both stems fully lifting from the cement mantle. Axial movement was not obtained in any of the other specimens.

Discussion and Conclusions

Release agents capable of greatly reducing the torsional loads at debonding are preferable for inclusion in implant interface conditions testing. As such, the mold release/conditioner was immediately discarded as a viable coating agent. The failure of the mineral oil and mineral oil/petroleum jelly coated stems in axial stem pullout also excluded them from future utilization. Both the petroleum jelly and carnauba wax were viable options for inclusion in future testing, however the carnauba wax flaked during embedment resulting in particulate formation within the cement. As the presence of particulates could compromise cement integrity carnauba wax was also disregarded as a potential debonding agent. Petroleum jelly was therefore selected as the release agent for use in compromising the implant-cement interface prior to implant embedment.

Appendix 11 – External Strain Gauge Application Technique

The following procedure was used to affix strain gauges to bone, using a previously developed gluing technique (Finlay et al., 1982; Cordey and Gautier, 1999; Kim et al., 2001), which was further modified in the Jack McBain Biomechanical Testing Laboratory (Dunham, 2005). The M-prep neutralizer, M-boned catalyst, M-boned 200 adhesive, M-Coat A polyurethane coating and strain gauge installation tape were all purchased from Viashay Micro-Measuremetns (Raleigh, NC, USA).

- (1) Remove any excess tissue from the surface of the bone where the gauge is to be positioned
- (2) Rub the bone with an alcohol pad to degrease and sand with 400 grit sandpaper. Repeat 2 times.
- (3) Apply M-prep neutralizer and scrub with a cotton tipped applicator. Wipe dry with a single wipe of a clean cotton swab.
- (4) Apply a thin layer of catalyst and let dry for 1 min.
- (5) Add 2 drops of M-bond adhesive to the area and using a piece of gauge installation tape press into a thin layer using finger pressure. Hold for 1 min.
- (6) Wait 5 minutes.

- (7) Remove the tape and smooth the surface with sandpaper.
- (8) Apply M-prep neutralizer and scrub with a cotton tipped applicator. Wipe dry with a single wipe of a clean cotton swab.
- (9) Align strain gauge on a piece of gauge installation tape.
- (10) Apply a thin layer of catalyst to the bone and gage, let dry for 1 min.
- (11) Apply one drop of M-bond adhesive to the bone.
- (12) Align gauge and slowly rotate tape while pressing down on gauge. Using figure pressure hold gauge in place for one minute.
- (13) Remove tape by peeling back a sharp angle. Wait 5 min.
- (14) Apply M-coat polyurethane coating.

References

- Cordey, J., Gautier, E., 1999. Strain gauges used in the mechanical testing of bones. Part II: "In vitro" and "in vivo" technique. *Injury* 30, A14–20.
- Dunham, C.E., 2005. Biomedical assessments of synthetic and cadaveric distal humeri for laboratory-based investigations [M.E.Sc. Thesis]. The University of Western Ontario
- Finlay, J.B., Bourno, R.B., McLean, J., 1982. A Technique for the in vitro measurement of principal strains in the human tibia. *Journal of Biomechanics* 15, 723–739.
- Kim, Y., Kim, J.S., Cho, S.H., 2001. Strain distribution in the proximal human femur: An in vitro comparison in the intact femur and after insertion of reference and experimental femoral stems. *The Journal of Bone and Joint Surgery (Br)* 83, 295–301.

Appendix 12 – Loading Protocol

The loading protocol utilized in Chapter 2 and 3 is shown in Figure A.7.

Note that there is an initial period sans loading during which the unloaded strain response of the gauges may be collected. Between measured loads a 0.5 N relaxation period is provided, during this period loading is greatly reduced, but not fully eliminated, to prevent the Instron® from impacting the sample during load application.

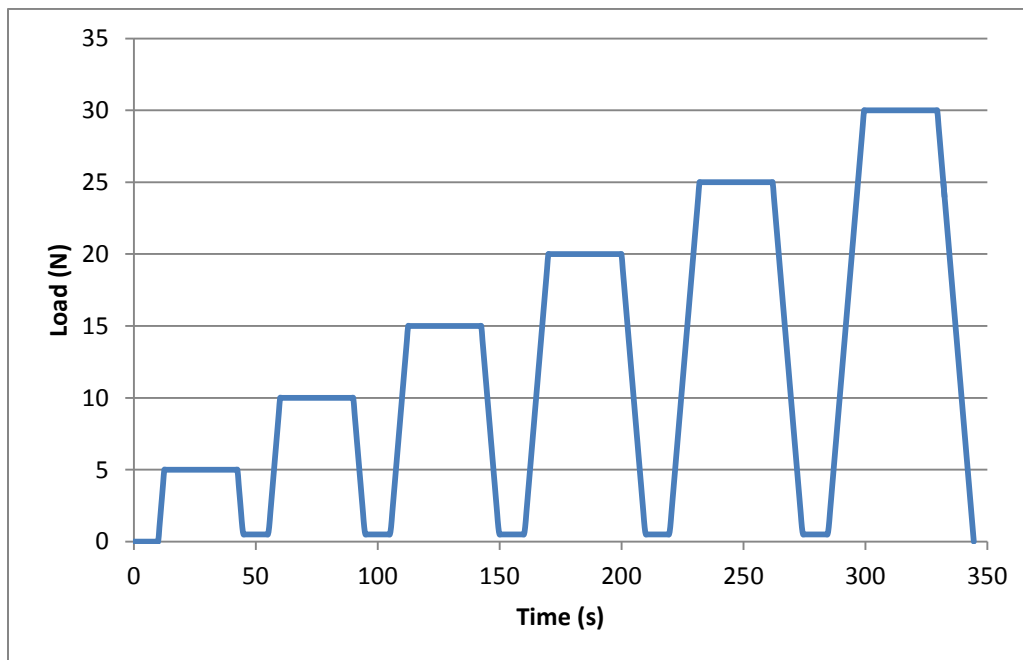


Figure A.7: Experimental loading protocol

This experimental loading protocol was applied directly to the implant head to simulate bending loads (5-30 N) and 0.5 mm from center along a torque arm to generate torsional and combined loads (0.025-0.15 Nm).

Appendix 13 – Free Body Diagram of Ulna with Loads

This appendix contains a free body diagram of the instrumented ulna with both bending and torsional loads applied.

Diagram 1 – Bending

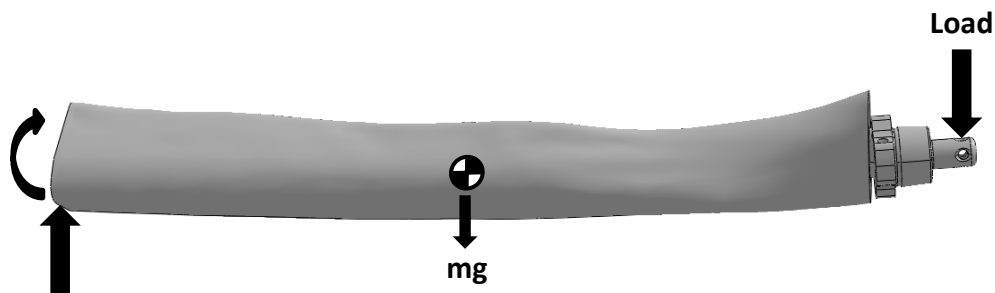


Diagram 2 – Torsion



Appendix 14 – Experimentally Derived Principal Strain Data

This appendix contains the tabulated processed strain data that was presented in part or summation in Chapter 3. The strain values are presented in units of microstrain ($\mu\epsilon$).

Strain Data for Loads Applied in Bending**Table A.6: Principal strain in specimen 11-03022 under bending load application**

Condition	Load (N)	Gauge						
		E10 (µε)	E10 (µε)	E10 (µε)	E10 (µε)	E10 (µε)	E10 (µε)	E10 (µε)
Bonded	5	58.1	60.8	49.1	51.5	26.8	24.3	26.6
	10	136.5	124.6	110.5	121.3	60.4	51.1	67.7
	15	204.3	187.1	163.2	187.5	87.8	78.9	107.0
	20	276.4	252.9	219.7	255.0	114.8	107.3	152.3
	25	357.2	328.7	283.2	331.1	144.5	140.9	202.6
	30	403.1	373.1	320.4	379.2	153.1	166.5	241.0
Semi-bonded	5	67.4	52.1	51.4	55.0	21.7	21.3	29.6
	10	150.6	127.1	115.6	132.9	45.0	59.9	82.4
	15	221.3	189.1	170.5	199.3	61.0	92.8	125.7
	20	291.8	248.9	226.2	263.6	75.9	125.8	166.2
	25	368.5	313.8	285.9	332.2	96.2	160.6	206.5
	30	426.2	374.8	333.3	395.2	105.7	196.8	234.2
Fully Debonded	5	48.4	42.6	37.6	32.6	11.0	15.5	16.0
	10	118.6	100.0	95.2	86.2	29.1	49.0	39.4
	15	185.6	158.0	149.9	141.6	48.2	76.6	58.4
	20	251.2	214.5	204.8	197.1	68.6	101.3	75.4
	25	346.3	295.3	282.8	278.4	95.0	129.3	94.4
	30	401.6	349.7	332.3	331.5	109.9	157.3	105.0
Semi-debonded	5	50.5	37.4	40.0	36.0	3.8	19.4	45.3
	10	130.8	109.8	105.9	87.9	17.6	53.2	101.8
	15	193.0	166.3	158.3	130.1	29.4	81.6	144.3
	20	248.0	220.0	203.2	166.4	42.1	108.2	181.5
	25	331.7	293.8	270.2	220.9	62.2	143.8	229.8
	30	376.8	346.1	308.3	252.1	73.5	172.2	250.6
Debonded	5	67.3	58.3	51.7	41.8	25.2	49.2	29.5
	10	144.4	125.9	113.1	98.7	32.7	104.8	-59.5
	15	209.6	183.4	165.6	147.1	40.3	149.0	-130.9
	20	270.3	244.9	215.1	200.7	51.2	190.4	-180.1
	25	348.7	313.7	277.0	267.8	68.3	240.5	-181.0
	30	399.4	362.9	319.9	312.6	77.9	276.3	-178.3

Table A.7: Principal strain in specimen 10-01004 under bending load application

Condition	Load (N)	Gauge						
		E10 ($\mu\epsilon$)	E10 ($\mu\epsilon$)	E10 ($\mu\epsilon$)	E10 ($\mu\epsilon$)	E10 ($\mu\epsilon$)	E10 ($\mu\epsilon$)	E10 ($\mu\epsilon$)
Bonded	5	32.6	56.3	40.4	31.5	22.4	29.0	15.4
	10	68.2	124.3	84.5	68.9	40.8	59.0	30.5
	15	102.1	200.9	128.5	108.1	59.3	89.6	45.2
	20	132.0	273.0	170.6	142.8	75.6	118.6	59.6
	25	174.8	346.0	216.9	180.5	94.5	148.3	75.4
	30	194.4	417.8	258.4	208.7	110.8	175.6	91.2
Semi-bonded	5	60.7	74.3	48.6	43.1	19.2	31.6	14.0
	10	117.8	146.9	94.1	83.4	34.5	60.0	28.2
	15	172.4	219.8	139.2	119.3	49.3	85.2	42.8
	20	223.2	290.1	183.5	154.5	61.4	110.3	57.5
	25	278.7	361.4	228.7	191.9	73.1	136.1	72.5
	30	314.0	433.6	269.7	222.0	83.9	161.3	87.2
Fully Debonded	5	29.6	51.3	43.0	5.4	5.1	34.6	39.0
	10	58.6	115.2	85.2	17.2	14.9	43.3	48.0
	15	86.1	176.1	126.9	35.3	23.7	65.3	54.9
	20	114.0	239.7	167.9	55.5	31.7	96.9	61.7
	25	143.9	300.5	211.1	76.0	38.9	123.1	68.4
	30	170.1	360.4	251.4	92.9	46.4	156.0	76.8
Semi-debonded	5	32.5	67.1	41.0	39.1	9.8	31.1	58.9
	10	66.1	131.2	79.9	73.4	17.7	51.5	105.7
	15	100.3	190.9	119.5	101.8	26.0	64.6	148.2
	20	131.8	257.7	157.2	137.0	35.6	84.1	197.5
	25	165.3	320.3	195.9	171.5	45.0	98.9	240.0
	30	193.4	382.2	231.9	200.0	53.2	108.0	276.9
Debonded	5	26.3	48.3	31.3	23.2	4.1	17.8	24.1
	10	55.5	107.6	70.5	48.6	6.5	34.1	51.3
	15	85.7	170.2	110.0	71.9	12.0	46.9	67.1
	20	114.3	235.6	148.0	97.4	18.7	61.7	79.0
	25	145.1	297.4	188.0	123.5	26.0	79.2	89.8
	30	170.8	363.9	224.0	145.8	33.7	97.2	98.7

Table A.8: Principal strain in specimen 11-03026 under bending load application

Condition	Load (N)	Gauge						
		E10 ($\mu\epsilon$)	E10 ($\mu\epsilon$)	E10 ($\mu\epsilon$)	E10 ($\mu\epsilon$)	E10 ($\mu\epsilon$)	E10 ($\mu\epsilon$)	E10 ($\mu\epsilon$)
Bonded	5	58.0	48.5	41.9	32.3	30.4	23.7	58.1
	10	140.2	114.5	98.9	73.0	57.9	48.7	86.5
	15	227.5	184.5	159.0	114.1	88.3	75.3	130.0
	20	312.6	253.5	218.4	158.2	116.6	104.0	169.4
	25	401.3	323.0	279.4	200.0	146.2	131.2	217.1
	30	488.2	395.5	341.1	245.6	176.5	161.6	263.4
Semi-bonded	5	66.9	44.5	37.1	33.0	31.9	21.9	179.8
	10	148.6	112.1	93.2	74.7	57.7	47.4	332.5
	15	232.0	176.0	151.3	109.6	83.8	72.9	487.5
	20	317.8	246.5	211.4	146.2	111.9	100.8	537.9
	25	405.6	318.4	273.4	183.5	139.4	128.4	582.9
	30	491.2	393.2	334.0	215.3	170.5	160.0	628.9
Fully Debonded	5	78.3	71.6	38.5	24.4	11.2	24.1	18.9
	10	163.3	143.8	88.6	47.7	25.5	54.9	68.1
	15	248.8	211.9	140.6	69.7	40.0	79.6	287.5
	20	332.3	284.6	194.9	85.0	49.2	101.1	96.9
	25	418.3	353.6	251.8	100.0	59.8	121.6	84.2
	30	503.5	422.6	311.2	113.5	72.3	148.8	399.2
Semi-debonded	5	72.1	54.9	45.3	30.9	16.2	8.9	73.7
	10	156.4	122.7	106.4	70.1	37.4	21.1	176.9
	15	240.6	191.4	167.3	103.1	55.9	36.7	284.8
	20	327.2	263.4	229.3	134.3	75.0	55.4	397.0
	25	411.2	333.9	290.1	167.3	91.0	76.1	510.1
	30	496.9	400.9	350.7	191.4	109.9	96.5	616.3
Debonded	5	75.8	67.6	51.0	32.2	29.0	34.0	152.1
	10	161.1	137.3	105.4	59.7	48.7	88.4	239.6
	15	243.9	200.5	158.2	86.9	65.5	129.8	277.7
	20	327.5	272.6	212.6	112.1	77.0	162.8	300.4
	25	414.1	339.6	269.6	143.8	90.3	191.9	314.0
	30	498.3	405.6	326.4	177.3	101.9	219.3	331.0

Table A.9: Principal strain in specimen 09-12057 under bending load application

Condition	Load (N)	Gauge						
		E10 ($\mu\epsilon$)	E10 ($\mu\epsilon$)	E10 ($\mu\epsilon$)	E10 ($\mu\epsilon$)	E10 ($\mu\epsilon$)	E10 ($\mu\epsilon$)	E10 ($\mu\epsilon$)
Bonded	5	93.4	75.9	50.9	53.8	35.0	18.2	28.4
	10	183.5	144.8	98.7	102.6	65.8	37.0	53.4
	15	271.7	224.2	147.9	151.8	98.1	57.0	78.3
	20	362.6	298.0	197.4	196.4	130.1	75.8	105.5
	25	454.9	381.6	249.6	249.6	164.0	99.1	134.2
	30	547.1	457.4	297.1	296.3	195.8	123.8	164.4
Semi-bonded	5	92.0	82.7	50.0	54.7	27.3	22.1	34.0
	10	182.4	161.7	103.1	100.6	51.4	41.5	71.8
	15	273.6	237.1	154.3	140.8	73.6	62.4	113.6
	20	364.5	316.1	205.1	183.6	96.3	86.6	153.7
	25	455.6	396.0	256.5	226.7	119.0	111.5	190.6
	30	547.9	467.7	302.9	265.3	140.5	137.5	226.4
Fully Debonded	5	87.2	79.5	58.5	22.0	25.2	8.2	11.8
	10	174.4	153.0	109.1	46.1	47.5	12.0	18.6
	15	262.0	231.2	160.0	75.6	69.0	16.2	29.6
	20	351.3	311.6	212.6	107.7	89.8	25.0	40.7
	25	443.1	394.7	266.7	142.8	108.6	21.3	48.5
	30	535.2	469.7	316.6	171.3	128.0	11.7	60.5
Semi-debonded	5	86.9	85.5	52.7	55.8	35.6	16.3	40.5
	10	174.8	160.0	101.9	103.6	65.9	30.5	82.6
	15	265.1	240.7	150.9	153.1	97.1	46.6	130.0
	20	353.2	323.2	198.5	201.8	128.2	64.0	179.4
	25	443.6	399.7	248.5	246.9	158.3	80.0	224.4
	30	531.7	478.0	292.9	289.6	188.3	96.8	269.8
Debonded	5	94.9	77.9	44.5	38.6	6.5	21.8	17.7
	10	180.2	150.9	89.2	44.6	15.0	46.1	25.9
	15	266.2	224.9	134.2	71.0	29.1	66.7	28.4
	20	352.5	298.9	178.2	102.0	44.5	84.9	29.1
	25	437.2	371.0	224.3	137.2	61.7	100.3	29.9
	30	523.3	450.0	270.6	183.0	81.2	111.2	31.8

Table A.10: Principal strain in specimen 09-13055 under bending load application

Condition	Load (N)	Gauge						
		E10 ($\mu\epsilon$)	E10 ($\mu\epsilon$)	E10 ($\mu\epsilon$)	E10 ($\mu\epsilon$)	E10 ($\mu\epsilon$)	E10 ($\mu\epsilon$)	E10 ($\mu\epsilon$)
Bonded	5	36.6	72.2	73.1	63.3	16.9	25.5	
	10	70.2	143.1	144.2	126.6	32.6	45.3	
	15	102.4	215.9	216.8	190.9	48.7	68.4	
	20	134.1	286.6	291.2	248.9	63.8	90.5	
	25	169.9	357.4	366.4	306.7	79.4	112.7	
	30	193.6	434.2	441.4	368.4	93.1	136.2	
Semi-bonded	5	43.6	75.2	75.3	53.7	16.0	23.5	
	10	83.0	155.4	151.7	112.2	31.6	46.0	
	15	118.9	232.2	224.6	169.0	46.2	68.7	
	20	156.7	307.6	299.0	222.7	60.2	90.5	
	25	196.7	383.0	372.3	279.8	74.6	114.8	
	30	225.3	458.9	447.9	333.6	87.7	136.5	
Fully Debonded	5	36.5	73.3	56.5	11.2	7.8	12.3	
	10	74.0	145.8	123.5	19.3	10.9	22.6	
	15	110.4	216.1	192.6	36.7	15.9	33.3	
	20	144.9	288.2	264.2	63.2	18.9	45.3	
	25	184.6	363.5	336.7	91.2	23.9	56.4	
	30	211.2	437.4	407.7	121.5	27.1	69.2	
Semi-debonded	5	39.6	73.7	66.7	45.2	-0.7	21.3	17.6
	10	71.6	133.0	136.6	72.6	-0.3	42.3	3.5
	15	101.7	201.9	207.9	101.4	2.0	63.5	17.1
	20	131.2	269.2	280.4	132.4	5.7	85.5	22.6
	25	164.5	334.2	352.4	162.0	10.2	106.4	27.2
	30	187.1	400.7	426.2	195.4	15.0	129.5	34.4
Debonded	5	34.2	64.9	69.5	48.7	3.2	25.9	137.5
	10	71.9	131.6	138.9	81.3	1.8	45.5	233.9
	15	104.0	200.9	208.8	110.5	1.8	68.6	262.2
	20	137.4	269.2	277.7	134.9	5.6	91.3	259.5
	25	174.8	338.0	347.8	163.5	12.6	113.9	254.5
	30	202.1	401.4	418.5	190.5	19.6	134.3	248.5

Table A.11: Principal strain in specimen 10-06020 under bending load application

Condition	Load (N)	Gauge						
		E10 ($\mu\epsilon$)	E10 ($\mu\epsilon$)	E10 ($\mu\epsilon$)	E10 ($\mu\epsilon$)	E10 ($\mu\epsilon$)	E10 ($\mu\epsilon$)	E10 ($\mu\epsilon$)
Bonded	5	50.4	78.8	79.8	55.2	25.2		32.4
	10	102.8	157.7	157.2	111.2	49.5		66.9
	15	153.4	232.8	233.6	167.4	72.2		98.7
	20	204.3	309.7	311.8	222.0	96.2		135.2
	25	256.5	387.4	390.3	278.1	123.0		170.5
	30	305.4	468.8	471.5	335.3	184.0		206.0
Semi-bonded	5	59.8	70.4	78.6	52.3	24.6		35.9
	10	113.5	150.1	153.7	108.2	43.7		73.2
	15	169.2	230.6	232.6	161.4	62.1		114.8
	20	226.8	316.8	317.5	215.1	79.8		164.4
	25	283.3	401.2	399.7	268.5	97.3		209.4
	30	334.1	474.9	476.7	319.0	111.3		246.7
Fully Debonded	5	50.9	83.9	74.7	25.1	13.4		45.4
	10	105.8	161.8	151.8	53.7	19.2		77.1
	15	160.1	240.6	230.0	82.4	23.7		110.3
	20	215.3	316.6	309.1	110.9	25.8		143.5
	25	269.2	397.5	387.0	142.6	31.5		179.9
	30	322.9	476.0	470.1	174.0	33.2		217.5
Semi-debonded	5	56.3	68.6	78.8	54.2	-0.6		26.0
	10	112.6	139.8	150.3	106.0	-3.7		49.5
	15	167.3	213.0	222.6	158.3	-5.0		72.5
	20	221.2	281.6	292.8	207.2	-5.3		93.4
	25	277.2	349.9	365.0	254.5	-5.6		116.1
	30	329.4	421.1	439.2	303.0	-3.0		130.4
Debonded	5	57.7	70.7	73.6	45.6	6.0		36.2
	10	114.5	144.5	145.7	87.1	6.3		51.5
	15	169.7	215.6	217.9	127.6	3.5		58.3
	20	226.2	284.5	291.9	165.6	6.0		65.9
	25	281.1	361.1	364.6	209.5	9.5		75.2
	30	334.9	435.4	440.5	249.6	15.2		83.3

Table A.12: Principal strain in specimen 11-03045 under bending load application

Condition	Load (N)	Gauge						
		E10 ($\mu\epsilon$)	E10 ($\mu\epsilon$)	E10 ($\mu\epsilon$)	E10 ($\mu\epsilon$)	E10 ($\mu\epsilon$)	E10 ($\mu\epsilon$)	E10 ($\mu\epsilon$)
Bonded	5	67.4	44.3	80.5	44.1	40.8	25.2	38.4
	10	140.1	87.2	161.7	85.7	82.1	48.6	80.8
	15	208.1	138.8	243.0	130.3	119.2	79.7	125.3
	20	276.7	183.7	325.6	167.3	154.9	106.3	168.9
	25	347.4	237.4	410.5	208.8	190.5	136.3	212.6
	30	409.9	287.7	496.3	239.5	223.3	164.6	256.8
Semi-bonded	5	74.2	56.2	83.0	44.3	36.0	34.8	34.7
	10	150.0	103.9	168.9	82.7	70.2	67.8	77.1
	15	224.4	157.2	255.0	123.8	102.4	108.9	123.1
	20	298.0	209.7	344.2	161.5	134.4	150.3	170.2
	25	371.8	264.8	431.8	201.2	164.6	195.4	217.3
	30	440.6	316.3	524.5	232.6	194.9	244.3	266.0
Fully Debonded	5	75.3	71.5	100.7	28.7	23.2	37.9	40.4
	10	146.8	136.4	201.1	53.5	56.7	72.6	53.0
	15	218.2	207.7	303.3	82.6	96.8	110.2	91.7
	20	289.9	277.6	406.2	112.3	141.0	145.5	118.9
	25	361.0	346.8	507.7	142.0	182.5	180.7	141.3
	30	423.6	411.7	611.1	169.8	226.9	215.9	158.2
Semi-debonded	5	74.7	48.5	82.1	42.8	14.4	24.3	30.5
	10	148.0	95.0	164.8	69.9	22.5	40.1	37.9
	15	217.6	145.6	248.8	97.5	27.2	60.1	55.2
	20	289.1	201.2	335.9	129.8	34.2	84.5	79.5
	25	359.3	249.3	420.2	158.3	41.1	103.3	105.4
	30	422.3	299.4	505.8	181.9	57.3	126.7	126.7
Debonded	5	74.1	55.3	80.9	23.6	7.5	17.1	17.7
	10	146.3	106.1	164.5	32.7	9.9	38.1	2.3
	15	216.1	157.8	248.2	48.5	21.2	61.8	1.0
	20	284.7	212.7	334.0	71.9	39.7	87.1	2.4
	25	354.4	263.9	419.9	93.6	58.9	107.3	-1.9
	30	416.0	313.5	507.4	114.2	79.6	130.9	-2.5

Table A.13: Principal strain in specimen 11-03057 under bending load application

Condition	Load (N)	Gauge						
		E10 ($\mu\epsilon$)	E5 ($\mu\epsilon$)	E4 ($\mu\epsilon$)	E2 ($\mu\epsilon$)	E1 ($\mu\epsilon$)	I4 ($\mu\epsilon$)	I1 ($\mu\epsilon$)
Bonded	5	72.8	82.9	49.8	59.7	37.9	24.4	15.9
	10	153.9	165.8	105.2	118.3	79.1	49.3	25.7
	15	233.7	247.7	154.9	179.8	117.0	77.8	36.4
	20	315.2	329.6	205.4	240.4	152.6	106.2	46.5
	25	397.9	416.5	257.8	302.7	187.7	136.4	59.9
	30	477.5	498.4	304.4	361.2	214.5	165.0	67.6
Semi-bonded	5	80.9	85.1	53.6	69.7	35.9	28.0	9.3
	10	161.8	164.4	107.0	130.4	69.3	57.8	19.4
	15	244.2	241.6	159.3	188.3	98.1	90.0	29.8
	20	325.1	324.5	211.5	248.3	123.7	124.4	39.1
	25	403.5	401.1	265.4	301.9	147.3	156.3	48.2
	30	486.1	486.6	316.6	360.0	169.5	190.8	57.9
Fully Debonded	5	72.9	85.4	64.2	14.6	12.5	12.3	52.7
	10	154.4	186.2	134.3	26.9	29.7	26.2	115.9
	15	237.7	291.9	209.2	39.9	46.4	41.1	176.5
	20	319.1	382.9	275.4	54.3	64.2	53.6	250.0
	25	399.2	467.8	340.7	69.0	74.4	64.2	315.7
	30	481.6	558.0	401.4	84.6	91.0	72.3	393.0
Semi-debonded	5	52.2	59.7	34.7	30.4	1.5	4.4	22.4
	10	99.8	111.0	65.4	56.1	0.5	11.5	39.5
	15	143.6	161.9	93.5	81.6	-0.8	22.7	56.6
	20	173.8	191.9	110.3	93.2	-5.5	39.9	72.2
	25	201.1	221.1	128.4	104.0	-9.5	50.3	87.6
	30	225.7	250.0	140.6	109.8	-9.7	52.1	104.7
Debonded	5	80.1	80.9	58.8	52.0	0.8	19.1	8.7
	10	161.0	173.0	117.7	107.7	1.9	44.0	26.4
	15	239.0	253.5	168.2	156.6	3.3	66.0	37.9
	20	319.2	333.7	220.0	203.1	8.6	85.9	51.6
	25	398.6	410.7	272.8	249.6	13.8	100.4	63.4
	30	478.5	493.5	322.0	296.6	21.1	113.5	76.2

Strain Data for Torsional Loading**Table A.14: Principal strain in specimen 11-03022 during torsional loading**

Condition	Load ($\times 10^{-2}$ Nm)	Gauge						
		E10 ($\mu\epsilon$)	E10 ($\mu\epsilon$)	E10 ($\mu\epsilon$)	E10 ($\mu\epsilon$)	E10 ($\mu\epsilon$)	E10 ($\mu\epsilon$)	E10 ($\mu\epsilon$)
Bonded	2.5	15.6	12.4	9.3	20.5	7.3	8.5	7.1
	5.0	28.5	26.1	16.2	39.1	10.3	15.5	15.8
	7.5	32.4	29.0	18.6	48.6	9.5	20.0	19.4
	10.0	35.5	32.0	19.3	54.9	9.3	22.4	22.8
	12.5	39.5	37.2	20.7	65.3	8.3	26.8	25.3
	15.0	42.4	39.2	21.4	70.6	6.2	29.1	28.1
Semi-bonded	2.5	8.2	6.1	4.1	12.1	7.9	6.6	11.9
	5.0	18.4	7.7	11.3	26.0	13.3	15.1	23.7
	7.5	27.0	16.6	19.2	44.8	18.4	23.5	34.6
	10.0	37.5	28.9	28.5	65.1	22.5	32.3	47.3
	12.5	48.8	39.5	39.5	83.0	27.5	38.7	61.1
	15.0	57.9	50.5	47.8	100.2	31.8	45.1	74.5
Fully Debonded	2.5	27.0	30.0	28.9	17.4	5.6	70.4	24.0
	5.0	57.7	65.7	60.7	26.9	7.4	193.8	104.8
	7.5	80.2	97.3	86.1	35.1	10.5	319.3	221.6
	10.0	101.3	128.6	114.2	40.4	32.2	492.3	447.1
	12.5	122.6	150.9	137.4	45.1	22.9	489.2	428.2
	15.0	149.7	205.8	180.3	62.7	84.3	666.0	806.9
Semi-debonded	2.5	12.3	13.6	14.2	5.5	3.8	10.0	22.8
	5.0	14.4	16.9	17.3	6.5	3.2	9.5	32.1
	7.5	17.3	23.3	20.7	9.4	3.4	9.6	43.8
	10.0	22.1	30.3	25.1	10.8	4.5	10.3	55.2
	12.5	26.0	37.0	29.1	13.0	4.5	10.7	66.6
	15.0	28.0	41.9	30.1	16.1	4.4	11.7	75.2
Debonded	2.5	6.6	6.8	5.5	2.9	1.5	0.9	5.0
	5.0	4.1	11.4	8.5	1.6	0.0	2.5	9.5
	7.5	3.4	16.4	13.0	-1.8	-1.5	-2.1	15.1
	10.0	5.0	22.5	15.8	-0.7	-3.1	-6.1	20.1
	12.5	7.4	26.7	21.3	-1.3	-3.6	-8.3	24.9
	15.0	10.9	32.7	26.6	-1.3	-2.9	-7.0	32.7

Table A.15: Principal strain in specimen 10-01004 during torsional loading

Condition	Load ($\times 10^{-2}$ Nm)	Gauge						
		E10 ($\mu\epsilon$)	E10 ($\mu\epsilon$)	E10 ($\mu\epsilon$)	E10 ($\mu\epsilon$)	E10 ($\mu\epsilon$)	E10 ($\mu\epsilon$)	E10 ($\mu\epsilon$)
Bonded	2.5	44.9	65.8	51.1	38.6	19.7	30.7	15.0
	5.0	75.0	121.6	88.0	69.4	36.1	55.0	26.1
	7.5	78.2	146.3	103.1	80.9	43.9	64.0	31.1
	10.0	74.5	162.4	110.0	87.4	46.2	69.5	32.5
	12.5	77.8	171.3	119.7	87.8	50.3	70.6	34.3
	15.0	73.8	186.6	124.8	91.3	52.5	74.1	35.3
Semi-bonded	2.5	47.5	51.0	34.7	28.9	15.0	21.1	12.7
	5.0	92.1	111.2	72.7	59.8	27.1	44.8	23.2
	7.5	102.2	133.2	86.6	65.9	31.8	50.7	27.2
	10.0	102.3	141.0	92.8	66.9	34.0	51.0	29.0
	12.5	113.4	158.2	105.4	73.9	37.8	56.8	31.4
	15.0	117.5	173.7	114.8	77.1	39.9	60.5	33.8
Fully Debonded	2.5	27.7	53.3	44.1	5.0	9.1	59.5	4.9
	5.0	47.8	98.0	78.1	10.3	10.0	92.9	3.5
	7.5	56.2	119.6	97.5	10.3	10.1	112.8	3.3
	10.0	62.2	140.4	111.8	13.1	12.8	129.2	1.2
	12.5	66.5	151.3	124.5	11.6	14.8	147.4	-1.1
	15.0	65.6	161.9	133.5	13.5	16.1	159.6	-6.6
Semi-debonded	2.5	16.3	25.5	11.7	12.3	9.6	9.4	22.7
	5.0	26.5	44.0	25.4	18.2	13.9	14.2	44.3
	7.5	36.9	66.2	38.4	26.5	18.1	21.6	73.5
	10.0	44.7	82.1	49.9	32.3	20.3	25.9	94.8
	12.5	55.0	102.9	61.8	40.3	22.6	32.7	123.2
	15.0	64.9	118.3	73.2	44.5	23.0	34.0	144.1
Debonded	2.5	5.7	17.0	14.5	8.2	4.7	3.2	6.7
	5.0	14.6	34.4	26.3	13.2	2.6	4.3	9.8
	7.5	24.2	50.2	37.6	16.4	1.7	4.7	9.2
	10.0	32.1	66.3	48.0	22.2	0.7	5.6	9.7
	12.5	43.1	83.8	62.0	25.9	0.2	3.2	13.5
	15.0	53.2	103.8	75.7	33.6	0.8	7.3	17.9

Table A.16: Principal strain in specimen 11-03026 during torsional loading

Condition	Load ($\times 10^{-2}$ Nm)	Gauge						
		E10 ($\mu\epsilon$)	E10 ($\mu\epsilon$)	E10 ($\mu\epsilon$)	E10 ($\mu\epsilon$)	E10 ($\mu\epsilon$)	E10 ($\mu\epsilon$)	E10 ($\mu\epsilon$)
Bonded	2.5	39.7	28.2	27.6	17.4	7.8	13.8	21.3
	5.0	74.9	55.9	48.5	43.8	33.1	30.0	43.9
	7.5	108.8	76.6	70.3	59.8	48.6	43.0	66.1
	10.0	143.6	104.0	90.5	77.4	62.0	59.0	80.4
	12.5	157.4	112.8	100.2	95.7	89.0	82.4	95.3
	15.0	174.9	120.8	109.9	108.6	93.8	90.3	92.6
Semi-bonded	2.5	18.5	21.4	18.5	15.1	13.5	6.5	32.0
	5.0	41.9	46.8	38.7	28.8	30.2	19.9	45.9
	7.5	67.1	70.1	61.4	43.6	46.3	32.6	70.5
	10.0	92.9	90.3	84.2	56.7	63.9	46.8	131.9
	12.5	113.0	110.3	102.6	67.9	82.0	63.9	160.0
	15.0	131.6	131.0	119.2	79.9	104.7	89.6	207.5
Fully Debonded	2.5	11.3	12.1	12.9	12.1	8.4	2.6	962.6
	5.0	22.1	27.1	23.3	21.6	6.4	11.3	107.3
	7.5	34.4	40.9	34.6	37.5	8.3	21.0	187.5
	10.0	45.0	53.2	42.9	48.1	9.7	29.1	255.9
	12.5	54.3	65.8	50.6	60.5	13.3	36.8	313.9
	15.0	66.4	82.3	61.7	67.3	12.4	47.8	396.0
Semi-debonded	2.5	11.3	8.4	10.6	7.2	9.6	5.3	21.5
	5.0	36.1	29.2	28.3	13.9	21.5	16.5	58.3
	7.5	49.5	39.9	39.0	19.2	29.4	27.9	83.9
	10.0	63.8	53.8	51.0	26.0	38.4	40.3	112.1
	12.5	74.7	65.7	60.3	32.8	46.4	51.3	136.2
	15.0	84.1	78.0	69.3	40.2	54.1	65.4	159.0
Debonded	2.5	16.6	13.4	11.3	6.5	12.5	8.3	23.5
	5.0	36.1	27.0	24.3	12.8	25.3	19.6	46.9
	7.5	47.4	37.0	32.9	17.5	30.9	28.9	62.0
	10.0	58.0	46.4	40.4	21.1	30.7	34.4	78.9
	12.5	64.4	53.3	46.2	27.5	29.7	40.9	95.5
	15.0	73.6	59.9	54.7	33.3	29.2	45.8	110.4

Table A.17: Principal strain in specimen 09-12057 during torsional loading

Condition	Load ($\times 10^{-2}$ Nm)	Gauge						
		E10 ($\mu\epsilon$)	E10 ($\mu\epsilon$)	E10 ($\mu\epsilon$)	E10 ($\mu\epsilon$)	E10 ($\mu\epsilon$)	E10 ($\mu\epsilon$)	E10 ($\mu\epsilon$)
Bonded	2.5	35.8	31.4	25.0	21.3	26.7	6.9	14.0
	5.0	65.7	58.7	43.6	43.2	43.5	11.8	23.6
	7.5	91.5	89.0	61.2	68.0	63.3	16.8	33.3
	10.0	118.0	114.7	79.1	88.5	84.0	20.9	43.2
	12.5	143.3	135.5	97.2	107.4	102.8	23.9	52.1
	15.0	166.2	161.6	112.3	129.2	122.4	28.9	61.5
Semi-bonded	2.5	28.4	5.5	15.0	17.5	6.0	8.8	14.4
	5.0	52.5	19.6	28.0	26.4	11.7	14.4	32.2
	7.5	72.2	35.6	40.4	33.6	15.4	19.4	46.0
	10.0	90.9	54.2	52.0	42.4	21.2	24.6	57.6
	12.5	108.5	71.5	63.5	52.3	26.9	28.6	69.5
	15.0	123.6	93.2	74.8	63.0	35.1	33.8	82.3
Fully Debonded	2.5	24.3	24.4	15.6	5.0	6.0	59.3	10.5
	5.0	40.9	47.4	32.5	11.7	5.8	118.8	19.2
	7.5	57.7	64.6	50.1	16.8	10.5	182.2	20.0
	10.0	74.1	85.5	68.3	23.9	21.8	272.1	-1.9
	12.5	89.9	102.0	85.0	31.9	36.6	351.7	2.9
	15.0	106.3	122.2	100.5	45.7	69.0	477.5	27.0
Semi-debonded	2.5	36.1	30.8	25.9	22.9	11.1	13.3	19.3
	5.0	62.5	55.7	45.7	42.3	22.9	19.4	41.6
	7.5	86.1	83.5	65.8	63.5	35.5	26.2	67.3
	10.0	108.0	111.7	84.0	85.1	47.4	34.3	94.6
	12.5	130.8	136.3	107.6	102.8	59.7	41.7	124.7
	15.0	153.8	167.1	128.0	124.9	72.6	51.3	161.9
Debonded	2.5	27.2	33.2	17.2	15.4	8.7	4.0	17.9
	5.0	44.7	50.7	28.0	24.6	9.5	11.5	23.0
	7.5	63.3	66.5	37.4	26.3	12.7	11.9	22.6
	10.0	79.6	86.6	47.2	33.6	21.0	9.6	22.3
	12.5	92.2	101.4	56.7	39.6	29.2	7.4	22.9
	15.0	107.1	118.7	65.2	41.5	42.2	-0.7	24.7

Table A.18: Principal strain in specimen 09-13055 during torsional loading

Condition	Load ($\times 10^{-2}$ Nm)	Gauge						
		E10 ($\mu\epsilon$)	E10 ($\mu\epsilon$)	E10 ($\mu\epsilon$)	E10 ($\mu\epsilon$)	E10 ($\mu\epsilon$)	E10 ($\mu\epsilon$)	E10 ($\mu\epsilon$)
Bonded	2.5	12.2	35.6	27.4	27.2	8.8	15.5	
	5.0	21.3	57.1	48.3	43.3	12.4	21.1	
	7.5	30.3	83.5	68.9	58.8	16.1	26.1	
	10.0	37.2	103.3	89.1	73.8	20.5	33.1	
	12.5	46.5	124.6	109.3	88.5	25.6	40.2	
	15.0	51.8	145.8	128.9	102.4	28.7	45.7	
Semi-bonded	2.5	34.5	54.9	45.0	33.4	16.9	17.7	
	5.0	44.8	75.9	61.7	47.0	20.0	24.2	
	7.5	51.9	88.3	74.8	56.4	23.2	28.9	
	10.0	58.6	99.9	86.0	63.8	26.3	32.7	
	12.5	65.6	112.8	97.3	72.5	30.2	35.8	
	15.0	69.5	127.7	107.3	80.1	33.5	40.0	
Fully Debonded	2.5	13.9	19.1	17.9	12.6	3.4	10.6	
	5.0	20.8	33.6	31.6	15.7	4.1	34.1	
	7.5	27.4	46.9	45.6	18.9	4.7	48.6	
	10.0	35.3	63.7	62.8	23.9	5.4	62.0	
	12.5	42.8	80.2	79.5	27.2	6.6	77.6	
	15.0	50.4	93.4	95.5	33.5	8.7	88.8	
Semi-debonded	2.5	20.9	23.2	23.3	11.0	4.4	7.7	11.3
	5.0	34.7	42.0	41.9	18.9	3.9	12.7	13.8
	7.5	49.6	61.2	59.6	25.4	4.5	18.1	12.0
	10.0	62.2	75.4	75.8	29.4	4.0	22.6	8.0
	12.5	74.8	99.2	94.3	40.9	3.8	30.1	4.3
	15.0	85.9	118.7	114.1	47.0	2.8	36.9	-1.1
Debonded	2.5	16.7	39.7	36.5	16.5	5.7	13.2	53.4
	5.0	24.2	61.6	56.2	28.8	5.2	20.3	69.0
	7.5	34.9	81.4	75.3	35.6	5.2	25.5	76.9
	10.0	41.6	98.9	92.9	41.2	4.1	30.4	92.8
	12.5	50.5	116.6	110.5	46.3	3.2	34.9	97.6
	15.0	56.2	130.0	126.5	47.5	2.4	38.9	94.7

Table A.19: Principal strain in specimen 10-06020 during torsional loading

Condition	Load ($\times 10^{-2}$ Nm)	Gauge						
		E10 ($\mu\epsilon$)	E10 ($\mu\epsilon$)	E10 ($\mu\epsilon$)	E10 ($\mu\epsilon$)	E10 ($\mu\epsilon$)	E10 ($\mu\epsilon$)	E10 ($\mu\epsilon$)
Bonded	2.5	16.6	19.1	21.0	13.9	5.6		11.4
	5.0	29.0	36.7	42.5	35.4	15.1		23.2
	7.5	42.1	59.7	65.9	57.8	26.8		38.2
	10.0	53.8	76.6	88.1	78.4	34.9		50.2
	12.5	68.0	100.3	112.4	103.4	47.3		66.3
	15.0	78.2	122.3	136.3	127.6	57.9		80.4
Semi-bonded	2.5	26.0	26.8	18.4	23.0	20.3		16.0
	5.0	28.3	41.3	35.1	40.0	27.5		18.7
	7.5	35.3	57.2	52.1	54.4	34.6		25.0
	10.0	44.5	73.7	68.2	73.3	42.9		31.0
	12.5	51.3	87.8	85.8	90.4	49.7		34.8
	15.0	60.2	106.7	104.2	109.7	59.1		44.2
Fully Debonded	2.5	28.7	38.2	32.7	20.6	17.3		6.9
	5.0	46.6	71.2	60.9	34.4	21.5		13.8
	7.5	58.4	94.9	87.9	49.4	17.3		15.3
	10.0	68.7	116.0	111.5	62.3	15.6		19.3
	12.5	80.7	143.3	132.4	78.9	20.4		25.8
	15.0	90.0	162.1	151.1	90.1	18.9		29.9
Semi-debonded	2.5	11.2	16.0	26.4	22.7	6.9		19.1
	5.0	25.0	39.6	50.3	48.2	7.8		37.7
	7.5	39.2	63.1	74.0	72.3	11.7		51.2
	10.0	52.3	82.8	98.3	94.1	14.8		63.8
	12.5	64.3	107.0	121.8	119.4	17.6		80.9
	15.0	76.7	124.5	145.4	137.5	23.4		97.1
Debonded	2.5	28.3	32.2	29.4	12.3	8.9		10.5
	5.0	42.3	52.6	49.4	22.1	8.4		15.0
	7.5	52.1	66.2	62.7	28.8	9.1		19.7
	10.0	61.2	80.2	76.2	36.5	9.5		23.6
	12.5	70.3	93.6	90.1	45.0	8.5		26.1
	15.0	77.8	104.3	107.1	51.0	7.3		29.9

Table A.20: Principal strain in specimen 11-02045 during torsional loading

Condition	Load ($\times 10^{-2}$ Nm)	Gauge						
		E10 ($\mu\epsilon$)	E10 ($\mu\epsilon$)	E10 ($\mu\epsilon$)	E10 ($\mu\epsilon$)	E10 ($\mu\epsilon$)	E10 ($\mu\epsilon$)	E10 ($\mu\epsilon$)
Bonded	2.5	43.3	35.8	49.9	31.7	30.5	16.2	32.6
	5.0	54.7	51.8	69.5	48.2	49.8	22.2	52.1
	7.5	63.1	59.5	86.7	59.6	67.7	23.7	69.3
	10.0	69.2	70.0	100.3	70.8	83.0	27.7	86.3
	12.5	73.7	78.3	112.9	81.4	98.0	30.1	100.2
	15.0	78.1	87.9	126.5	88.5	111.4	32.3	114.7
Semi-bonded	2.5	13.9	14.7	15.0	15.9	15.2	9.1	19.3
	5.0	20.1	22.9	25.6	25.0	24.8	11.9	35.9
	7.5	30.1	30.5	37.0	32.4	35.9	14.4	54.1
	10.0	38.6	38.2	47.8	38.8	44.7	17.2	72.0
	12.5	44.0	43.9	57.3	46.5	52.7	20.9	89.3
	15.0	50.5	46.3	67.2	50.0	59.8	22.8	105.7
Fully Debonded	2.5	25.5	25.6	42.7	13.4	0.9	24.6	38.1
	5.0	47.4	45.8	68.8	15.2	2.3	48.4	46.6
	7.5	54.6	57.6	77.9	17.3	-0.5	69.5	55.0
	10.0	60.1	60.7	87.2	15.8	-5.0	79.5	49.0
	12.5	69.0	69.3	97.1	16.3	-7.9	85.7	52.2
	15.0	74.8	74.7	105.1	17.1	-12.0	88.9	51.8
Semi-debonded	2.5	15.3	8.1	18.1	10.6	5.9	2.4	3.3
	5.0	27.1	17.9	32.8	21.4	11.7	4.6	7.8
	7.5	37.7	25.7	46.9	28.7	17.3	5.7	8.0
	10.0	47.8	33.9	59.8	37.8	19.7	8.4	7.9
	12.5	56.3	43.4	70.5	46.7	21.3	12.4	8.8
	15.0	65.6	53.5	83.3	55.1	26.2	15.0	7.3
Debonded	2.5	9.0	16.4	21.6	9.4	10.0	12.6	11.1
	5.0	15.4	22.3	34.4	8.4	11.5	12.4	11.8
	7.5	24.3	30.4	47.7	9.1	12.8	14.8	12.7
	10.0	31.3	41.6	57.9	10.5	15.1	22.6	21.1
	12.5	35.3	46.4	64.4	10.3	15.0	25.1	22.0
	15.0	41.5	51.1	71.8	9.9	15.2	29.2	22.4

Table A.21: Principal strain in specimen 11-03057 during torsional loading

Condition	Load ($\times 10^{-2}$ Nm)	Gauge						
		E10 ($\mu\epsilon$)	E10 ($\mu\epsilon$)	E10 ($\mu\epsilon$)	E10 ($\mu\epsilon$)	E10 ($\mu\epsilon$)	E10 ($\mu\epsilon$)	E10 ($\mu\epsilon$)
Bonded	2.5	21.3	30.1	18.9	28.0	17.4	13.0	6.1
	5.0	40.5	53.4	35.0	50.0	34.0	21.1	9.0
	7.5	54.4	71.4	44.8	65.5	43.3	26.4	10.4
	10.0	68.5	89.4	56.0	82.3	58.1	33.6	13.9
	12.5	78.5	100.7	65.8	98.3	70.8	40.0	15.9
	15.0	86.9	117.2	72.5	114.8	83.9	48.1	18.6
Semi-bonded	2.5	46.2	52.9	27.6	32.8	15.7	13.1	6.6
	5.0	83.7	92.9	54.1	60.9	34.6	26.7	11.8
	7.5	119.4	133.3	78.9	89.8	51.8	42.0	16.2
	10.0	144.8	163.8	95.7	111.8	65.0	55.1	20.5
	12.5	156.2	176.6	103.9	123.6	72.3	62.7	22.5
	15.0	167.1	190.8	111.1	135.0	80.3	70.7	24.9
Fully Debonded	2.5	35.6	37.1	28.0	17.2	1.4	9.5	6.2
	5.0	74.3	73.0	54.3	26.0	-4.5	30.7	19.2
	7.5	114.8	108.0	81.5	31.0	-3.4	56.2	35.8
	10.0	153.3	148.7	107.4	38.9	0.5	80.2	56.6
	12.5	190.0	186.9	134.1	47.3	1.1	96.2	82.7
	15.0	227.4	224.5	158.8	52.9	5.5	111.8	121.9
Semi-debonded	2.5	41.4	46.1	32.6	26.6	10.5	9.7	12.5
	5.0	83.4	87.6	61.0	50.3	14.4	15.9	19.2
	7.5	125.2	129.7	89.4	71.4	20.6	27.6	26.9
	10.0	165.2	172.8	115.0	91.8	29.0	44.4	35.2
	12.5	201.9	207.7	139.9	109.6	32.9	61.2	40.9
	15.0	232.2	243.5	158.7	127.2	40.6	79.6	46.9
Debonded	2.5	72.2	66.5	44.8	40.3	-0.9	17.6	15.8
	5.0	102.7	96.4	63.5	58.1	-2.9	21.0	20.0
	7.5	129.3	125.7	78.3	75.6	-2.1	25.6	24.9
	10.0	151.9	145.5	90.3	86.5	-6.1	27.6	26.5
	12.5	164.7	161.0	95.7	94.1	-3.3	29.5	29.2
	15.0	171.9	164.2	95.8	95.2	-6.7	27.6	27.3

Strain Data for Combined Loading**Table A.22: Principal strain in specimen 11-03022 during combined loading**

Condition	Load N ($\times 10^{-2}$ Nm)	Gauge						
		E10 ($\mu\epsilon$)	E10 ($\mu\epsilon$)	E10 ($\mu\epsilon$)	E10 ($\mu\epsilon$)	E10 ($\mu\epsilon$)	E10 ($\mu\epsilon$)	E10 ($\mu\epsilon$)
Bonded	5 (2.5)	72.4	55.9	53.9	72.5	31.3	30.6	36.4
	10 (5.0)	138.8	116.6	105.6	139.2	54.5	57.3	72.1
	15 (7.5)	203.4	167.5	154.3	198.2	75.7	78.9	108.4
	20 (10.0)	266.6	224.6	202.3	263.2	95.4	105.2	144.5
	25 (12.5)	331.0	275.3	248.0	326.9	117.6	128.6	188.6
	30 (15.0)	394.2	335.6	299.2	390.5	134.3	154.8	225.4
Semi-bonded	5 (2.5)	65.3	52.2	48.7	65.7	19.6	25.5	38.1
	10 (5.0)	142.9	113.8	107.2	137.8	36.7	51.9	87.4
	15 (7.5)	212.3	176.6	161.6	209.4	51.3	79.0	131.2
	20 (10.0)	275.1	232.5	209.9	271.4	64.0	103.3	168.8
	25 (12.5)	350.8	292.6	267.2	340.0	81.1	129.8	208.7
	30 (15.0)	404.6	348.4	310.8	400.2	90.0	155.2	235.5
Fully Debonded	5 (2.5)	67.8	60.4	49.8	36.8	5.1	109.1	51.6
	10 (5.0)	154.9	142.0	122.9	92.9	17.9	206.1	68.6
	15 (7.5)	222.7	209.3	182.3	141.4	31.9	282.7	76.8
	20 (10.0)	279.3	271.6	236.5	184.6	47.4	372.8	86.9
	25 (12.5)	356.1	353.0	308.2	246.6	66.6	463.5	80.6
	30 (15.0)	413.9	425.0	369.8	299.7	80.3	567.4	93.9
Semi-debonded	5 (2.5)	70.7	65.3	62.1	55.2	15.1	30.2	58.3
	10 (5.0)	140.0	126.3	121.7	105.9	23.8	52.9	106.8
	15 (7.5)	186.0	165.4	163.7	137.1	29.4	68.7	134.1
	20 (10.0)	253.1	231.5	221.5	188.8	41.9	96.4	165.6
	25 (12.5)	320.0	289.9	276.2	227.6	61.6	121.9	185.9
	30 (15.0)	368.2	342.2	316.4	263.2	71.6	147.2	247.2
Debonded	5 (2.5)	75.6	61.8	52.5	37.0	12.1	55.0	-16.0
	10 (5.0)	139.7	120.5	104.5	78.8	22.7	103.0	-21.6
	15 (7.5)	195.9	177.7	147.7	114.3	47.0	135.5	-26.8
	20 (10.0)	248.2	226.8	189.3	150.2	67.1	143.2	-24.8
	25 (12.5)	323.7	299.8	251.0	213.3	75.7	165.9	-14.4
	30 (15.0)	378.9	354.6	299.5	265.3	84.6	177.5	-6.0

Table A.23: Principal strain in specimen 10-01004 during combined loading

Condition	Load N ($\times 10^{-2}$ Nm)	Gauge						
		E10 ($\mu\epsilon$)	E10 ($\mu\epsilon$)	E10 ($\mu\epsilon$)	E10 ($\mu\epsilon$)	E10 ($\mu\epsilon$)	E10 ($\mu\epsilon$)	E10 ($\mu\epsilon$)
Bonded	5 (2.5)	44.2	50.0	39.6	29.0	16.1	27.6	10.7
	10 (5.0)	93.8	114.5	83.9	63.5	33.9	60.3	19.7
	15 (7.5)	137.0	181.2	129.3	97.0	51.0	92.8	30.9
	20 (10.0)	180.2	248.9	173.9	129.4	64.7	123.4	42.4
	25 (12.5)	230.5	316.2	219.3	164.1	75.0	150.8	53.9
	30 (15.0)	260.6	388.0	261.4	191.9	74.8	178.5	66.7
Semi-bonded	5 (2.5)	42.8	51.8	37.1	35.1	10.9	21.3	16.3
	10 (5.0)	98.7	118.5	82.7	67.0	24.8	46.6	26.4
	15 (7.5)	149.3	191.7	127.0	102.3	37.4	74.4	43.3
	20 (10.0)	197.1	260.0	171.2	132.0	49.6	98.8	51.5
	25 (12.5)	251.2	330.6	216.3	165.7	60.5	125.9	63.2
	30 (15.0)	285.5	399.5	258.1	191.4	69.9	150.7	68.3
Fully Debonded	5 (2.5)	28.1	51.8	39.6	9.9	9.5	14.3	11.7
	10 (5.0)	57.9	114.6	84.6	25.6	15.9	34.1	17.8
	15 (7.5)	84.9	176.7	128.3	43.5	21.6	54.4	20.2
	20 (10.0)	112.4	239.8	173.7	61.4	28.8	81.6	20.0
	25 (12.5)	141.9	306.6	220.6	82.1	36.9	119.2	19.6
	30 (15.0)	165.8	373.8	266.8	97.8	43.0	159.8	23.4
Semi-debonded	5 (2.5)	30.8	53.6	37.7	26.3	6.0	21.8	39.5
	10 (5.0)	62.0	112.5	75.0	51.0	10.6	35.7	87.4
	15 (7.5)	93.2	174.3	113.7	76.9	17.2	47.6	132.8
	20 (10.0)	123.1	234.3	151.4	103.3	24.5	60.6	177.7
	25 (12.5)	154.8	297.6	190.5	132.2	32.7	74.7	220.5
	30 (15.0)	180.0	356.9	225.2	155.6	39.2	86.7	271.1
Debonded	5 (2.5)	27.1	49.3	33.5	19.1	5.1	17.2	13.7
	10 (5.0)	57.9	109.3	72.2	41.4	9.5	32.7	23.3
	15 (7.5)	84.5	168.7	109.5	63.5	14.0	40.3	33.2
	20 (10.0)	111.6	231.2	147.5	86.2	19.8	47.8	43.0
	25 (12.5)	142.1	293.9	187.7	110.4	27.3	58.3	50.4
	30 (15.0)	165.4	351.8	224.4	127.8	32.7	64.8	69.1

Table A.24: Principal strain in specimen 11-03026 during combined loading

Condition	Load N ($\times 10^{-2}$ Nm)	Gauge						
		E10 ($\mu\epsilon$)	E10 ($\mu\epsilon$)	E10 ($\mu\epsilon$)	E10 ($\mu\epsilon$)	E10 ($\mu\epsilon$)	E10 ($\mu\epsilon$)	E10 ($\mu\epsilon$)
Bonded	5 (2.5)	70.3	57.1	44.8	29.5	25.4	21.1	30.1
	10 (5.0)	146.4	114.3	92.9	65.7	54.7	46.1	64.0
	15 (7.5)	219.5	164.6	138.1	98.2	86.2	72.3	103.8
	20 (10.0)	300.7	225.8	189.8	138.3	118.2	97.5	137.6
	25 (12.5)	377.1	284.9	239.0	168.6	149.7	126.3	164.4
	30 (15.0)	450.1	330.7	283.7	197.6	188.7	158.7	190.1
Semi-bonded	5 (2.5)	65.7	51.5	38.4	32.8	18.1	21.9	36.4
	10 (5.0)	143.3	107.5	88.4	60.4	41.6	46.7	122.3
	15 (7.5)	219.2	166.2	137.8	87.2	66.8	75.8	157.5
	20 (10.0)	288.4	220.3	180.4	108.3	96.6	109.4	178.3
	25 (12.5)	363.6	278.5	228.7	136.8	118.0	133.5	194.0
	30 (15.0)	445.5	338.7	283.0	165.3	158.6	159.9	222.6
Fully Debonded	5 (2.5)	45.6	37.5	31.9	17.6	17.5	10.8	30.2
	10 (5.0)	129.6	107.8	88.8	46.5	48.0	36.1	69.9
	15 (7.5)	213.5	176.6	147.7	73.2	73.0	66.4	704.2
	20 (10.0)	298.5	241.6	205.6	93.9	95.2	96.5	804.2
	25 (12.5)	383.5	314.8	263.8	115.0	112.6	119.8	416.6
	30 (15.0)	468.7	379.7	320.8	128.1	127.0	134.1	-97.8
Semi-debonded	5 (2.5)	67.4	56.1	44.7	28.0	14.4	12.5	66.5
	10 (5.0)	147.8	120.9	99.9	53.4	30.4	31.2	155.1
	15 (7.5)	226.8	188.2	153.6	79.6	46.9	51.9	246.6
	20 (10.0)	307.5	251.4	209.4	104.6	63.9	74.0	341.4
	25 (12.5)	388.1	318.6	264.5	132.1	81.1	97.7	432.4
	30 (15.0)	468.8	377.8	319.6	156.4	98.8	124.8	521.8
Debonded	5 (2.5)	67.5	52.6	53.3	22.9	6.5	21.9	85.0
	10 (5.0)	148.4	120.0	106.0	40.3	12.2	44.5	191.2
	15 (7.5)	226.5	177.2	157.5	54.0	18.7	66.9	271.2
	20 (10.0)	307.0	244.3	209.9	73.8	28.4	89.4	334.4
	25 (12.5)	386.1	306.5	261.6	89.8	38.3	107.0	387.7
	30 (15.0)	467.5	364.9	316.1	104.3	49.3	119.9	432.2

Table A.25: Principal strain in specimen 09-12057 during combined loading

Condition	Load N ($\times 10^{-2}$ Nm)	Gauge						
		E10 ($\mu\epsilon$)	E10 ($\mu\epsilon$)	E10 ($\mu\epsilon$)	E10 ($\mu\epsilon$)	E10 ($\mu\epsilon$)	E10 ($\mu\epsilon$)	E10 ($\mu\epsilon$)
Bonded	5 (2.5)	86.2	74.6	44.2	55.7	36.0	13.0	22.9
	10 (5.0)	175.5	143.7	91.0	99.6	70.4	27.2	45.7
	15 (7.5)	265.0	216.4	137.6	146.2	106.0	43.0	68.5
	20 (10.0)	354.9	292.6	184.1	195.3	140.1	61.0	91.5
	25 (12.5)	443.4	363.3	230.3	240.1	175.8	77.6	114.2
	30 (15.0)	535.7	437.4	277.1	287.5	211.5	97.4	138.1
Semi-bonded	5 (2.5)	89.4	80.0	46.9	37.2	21.7	16.5	36.2
	10 (5.0)	177.3	153.1	93.6	73.8	43.1	33.1	69.5
	15 (7.5)	265.2	227.7	141.1	111.5	68.2	49.9	95.6
	20 (10.0)	354.0	297.9	187.3	148.7	94.7	66.4	124.4
	25 (12.5)	442.4	375.5	235.1	189.7	119.2	85.1	151.5
	30 (15.0)	532.8	450.9	279.8	226.2	146.2	104.2	179.7
Fully Debonded	5 (2.5)	79.6	77.2	48.8	29.5	8.7	15.0	34.6
	10 (5.0)	167.2	142.0	93.9	46.9	10.7	45.2	32.7
	15 (7.5)	255.8	214.6	138.8	65.9	16.0	102.7	23.3
	20 (10.0)	344.9	282.8	184.6	84.7	20.9	152.4	21.3
	25 (12.5)	433.7	355.7	232.1	108.1	31.6	181.6	25.6
	30 (15.0)	521.8	416.6	274.1	126.2	48.2	209.3	28.0
Semi-debonded	5 (2.5)	88.3	64.5	49.4	31.7	25.8	20.4	27.3
	10 (5.0)	178.5	135.3	98.3	69.0	46.1	38.3	71.3
	15 (7.5)	266.0	208.8	145.2	107.6	60.4	55.8	117.8
	20 (10.0)	354.0	282.6	189.1	141.0	80.4	73.6	218.9
	25 (12.5)	443.0	354.6	237.4	175.5	100.1	91.1	277.4
	30 (15.0)	527.0	425.7	281.3	202.0	119.8	109.8	288.6
Debonded	5 (2.5)	86.4	72.1	40.8	25.4	13.4	1.3	20.8
	10 (5.0)	172.8	140.8	86.8	47.4	24.8	-0.3	27.6
	15 (7.5)	259.6	207.3	133.1	70.9	38.7	-6.0	42.3
	20 (10.0)	346.7	281.7	178.8	102.3	56.7	-12.7	60.5
	25 (12.5)	436.6	350.2	227.6	131.4	80.7	-31.0	79.3
	30 (15.0)	526.7	422.0	272.6	163.5	106.2	-42.3	94.7

Table A.26: Principal strain in specimen 09-13055 during combined loading

Condition	Load N ($\times 10^{-2}$ Nm)	Gauge						
		E10 ($\mu\epsilon$)	E10 ($\mu\epsilon$)	E10 ($\mu\epsilon$)	E10 ($\mu\epsilon$)	E10 ($\mu\epsilon$)	E10 ($\mu\epsilon$)	E10 ($\mu\epsilon$)
Bonded	5 (2.5)	32.9	75.3	70.5	58.9	22.1	29.2	
	10 (5.0)	69.2	137.2	138.4	108.4	37.9	47.9	
	15 (7.5)	103.1	206.8	207.5	162.7	54.7	70.2	
	20 (10.0)	136.0	276.2	276.5	217.1	71.6	91.3	
	25 (12.5)	172.1	345.5	346.5	271.2	87.8	112.7	
	30 (15.0)	198.8	414.2	417.5	325.4	103.1	134.7	
Semi-bonded	5 (2.5)	39.6	68.2	69.8	51.4	19.3	22.6	
	10 (5.0)	77.6	133.8	137.3	100.3	34.0	42.1	
	15 (7.5)	112.6	203.4	204.4	153.2	47.7	64.1	
	20 (10.0)	147.3	270.4	272.5	201.3	61.7	84.0	
	25 (12.5)	184.3	334.4	339.5	249.0	75.8	104.6	
	30 (15.0)	212.7	405.6	408.0	300.7	88.5	126.0	
Fully Debonded	5 (2.5)	35.6	74.9	60.0	20.2	17.3	20.6	
	10 (5.0)	72.7	137.3	124.0	30.7	23.9	28.2	
	15 (7.5)	105.5	196.3	188.2	43.1	28.1	40.1	
	20 (10.0)	139.6	263.5	253.2	59.3	32.2	58.1	
	25 (12.5)	177.6	320.9	318.7	72.0	37.6	73.0	
	30 (15.0)	205.1	384.8	384.4	90.5	40.0	89.0	
Semi-debonded	5 (2.5)	31.7	61.9	56.9	38.8	6.6	25.8	3.7
	10 (5.0)	63.5	121.2	121.3	67.5	8.6	46.2	11.0
	15 (7.5)	93.4	175.7	185.8	91.8	10.5	65.5	24.5
	20 (10.0)	124.8	241.8	251.6	122.4	14.9	87.0	31.7
	25 (12.5)	160.4	302.4	317.0	149.0	19.4	107.1	39.4
	30 (15.0)	187.1	364.8	383.6	178.9	23.9	128.7	48.2
Debonded	5 (2.5)	32.9	61.4	59.7	38.1	2.6	24.4	54.4
	10 (5.0)	65.5	125.9	122.4	59.9	2.9	44.2	42.0
	15 (7.5)	98.8	189.0	186.5	80.1	7.1	64.5	37.7
	20 (10.0)	130.0	247.8	248.7	101.5	11.9	83.9	32.9
	25 (12.5)	165.6	312.4	314.8	131.2	17.3	106.5	28.9
	30 (15.0)	196.2	377.7	381.3	158.7	24.9	126.2	21.9

Table A.27: Principal strain in specimen 10-06020 during combined loading

Condition	Load N ($\times 10^{-2}$ Nm)	Gauge						
		E10 ($\mu\epsilon$)	E10 ($\mu\epsilon$)	E10 ($\mu\epsilon$)	E10 ($\mu\epsilon$)	E10 ($\mu\epsilon$)	E10 ($\mu\epsilon$)	E10 ($\mu\epsilon$)
Bonded	5 (2.5)	48.6	68.0	65.8	48.6	26.6		34.6
	10 (5.0)	99.0	140.9	136.8	100.0	48.9		65.0
	15 (7.5)	149.1	212.4	210.4	151.2	70.2		94.8
	20 (10.0)	199.1	283.7	281.7	201.8	89.7		125.3
	25 (12.5)	249.8	355.1	355.9	252.5	111.5		157.3
	30 (15.0)	296.4	426.7	430.5	303.7	128.5		188.6
Semi-bonded	5 (2.5)	54.2	64.8	70.1	47.4	16.8		19.0
	10 (5.0)	105.4	127.9	134.8	95.7	33.8		38.6
	15 (7.5)	156.4	196.1	201.7	144.1	51.0		63.4
	20 (10.0)	208.5	263.7	271.5	190.8	67.8		90.7
	25 (12.5)	260.6	333.9	339.4	238.6	85.0		120.1
	30 (15.0)	309.6	398.6	409.9	284.1	97.4		142.6
Fully Debonded	5 (2.5)	56.3	66.3	57.6	27.3	9.6		9.1
	10 (5.0)	107.8	132.5	119.7	52.9	13.3		17.0
	15 (7.5)	155.0	195.8	182.2	78.2	14.4		23.0
	20 (10.0)	200.5	260.2	240.3	108.5	16.6		30.5
	25 (12.5)	246.6	314.7	295.6	132.0	22.3		40.8
	30 (15.0)	294.6	387.1	357.5	163.0	23.3		48.5
Semi-debonded	5 (2.5)	52.5	63.7	65.2	48.1	3.1		34.2
	10 (5.0)	101.9	132.5	132.0	94.4	0.2		61.4
	15 (7.5)	151.6	195.4	199.7	138.6	-1.0		81.2
	20 (10.0)	203.3	262.3	269.5	183.3	0.8		105.5
	25 (12.5)	254.9	330.0	339.3	229.1	-0.6		129.9
	30 (15.0)	302.8	397.7	409.0	270.8	2.8		157.7
Debonded	5 (2.5)	47.6	64.4	66.8	23.4	7.6		5.7
	10 (5.0)	100.9	130.1	133.1	47.1	12.8		9.2
	15 (7.5)	153.2	197.8	200.7	81.4	18.0		15.0
	20 (10.0)	203.9	263.0	267.6	117.0	20.8		22.9
	25 (12.5)	256.1	326.2	336.4	151.9	24.2		31.4
	30 (15.0)	305.4	387.1	407.2	185.0	28.1		41.6

Table A.28: Principal strain in specimen 11-03045 during combined loading

Condition	Load N ($\times 10^{-2}$ Nm)	Gauge						
		E10 ($\mu\epsilon$)	E10 ($\mu\epsilon$)	E10 ($\mu\epsilon$)	E10 ($\mu\epsilon$)	E10 ($\mu\epsilon$)	E10 ($\mu\epsilon$)	E10 ($\mu\epsilon$)
Bonded	5 (2.5)	71.3	40.6	74.5	47.9	33.8	19.0	34.5
	10 (5.0)	139.7	85.0	141.8	85.7	67.4	41.7	67.9
	15 (7.5)	210.6	125.4	211.9	119.2	100.2	63.7	102.0
	20 (10.0)	276.4	172.0	281.8	155.4	130.4	89.3	136.7
	25 (12.5)	343.0	215.6	350.1	190.4	157.5	115.4	170.1
	30 (15.0)	403.6	257.6	421.2	217.9	183.1	142.9	201.6
Semi-bonded	5 (2.5)	69.8	46.2	64.7	45.1	31.0	34.1	39.1
	10 (5.0)	139.4	89.2	132.8	76.5	55.1	65.0	72.7
	15 (7.5)	208.3	129.4	203.1	105.3	76.9	98.8	109.5
	20 (10.0)	278.9	173.0	275.5	134.0	99.2	136.4	148.5
	25 (12.5)	347.4	223.4	348.2	164.7	117.4	176.3	183.9
	30 (15.0)	410.7	265.9	423.7	186.8	137.4	212.7	217.5
Fully Debonded	5 (2.5)	73.0	56.2	73.4	21.3	17.6	39.2	56.3
	10 (5.0)	143.3	114.5	145.0	38.3	34.1	82.9	90.4
	15 (7.5)	211.5	163.3	213.6	48.3	54.5	117.5	104.0
	20 (10.0)	280.9	220.5	283.8	63.9	79.7	155.5	150.0
	25 (12.5)	350.7	273.2	355.6	77.8	102.7	189.9	163.8
	30 (15.0)	412.8	326.4	429.8	93.3	129.5	226.4	189.8
Semi-debonded	5 (2.5)	69.7	48.5	72.3	32.8	16.0	16.3	19.8
	10 (5.0)	138.3	97.6	146.2	61.6	27.1	35.4	20.6
	15 (7.5)	204.6	141.4	222.1	86.0	32.6	53.1	30.7
	20 (10.0)	270.2	188.7	298.6	109.7	42.5	72.5	51.5
	25 (12.5)	337.3	237.7	375.2	137.0	47.1	94.4	75.5
	30 (15.0)	396.3	283.5	454.3	153.3	54.3	120.0	81.1
Debonded	5 (2.5)	72.8	48.6	71.4	24.9	21.7	18.1	15.0
	10 (5.0)	143.5	96.6	143.1	43.6	34.3	34.8	16.9
	15 (7.5)	212.6	146.7	213.9	60.9	51.3	54.3	24.2
	20 (10.0)	279.4	190.0	286.7	77.8	64.5	71.8	14.9
	25 (12.5)	349.0	242.0	359.2	98.9	83.8	96.5	30.7
	30 (15.0)	411.8	287.4	434.8	114.7	100.6	112.8	15.1

Table A.29: Principal strain in specimen 11-03057 during combined loading

Condition	Load N ($\times 10^{-2}$ Nm)	Gauge						
		E10 ($\mu\epsilon$)	E10 ($\mu\epsilon$)	E10 ($\mu\epsilon$)	E10 ($\mu\epsilon$)	E10 ($\mu\epsilon$)	E10 ($\mu\epsilon$)	E10 ($\mu\epsilon$)
Bonded	5 (2.5)	71.6	75.5	45.4	58.7	34.2	25.6	12.8
	10 (5.0)	146.1	146.7	92.2	108.7	66.1	46.5	20.2
	15 (7.5)	220.5	222.5	136.9	160.4	96.2	68.7	29.3
	20 (10.0)	296.5	300.9	181.7	214.6	127.0	93.2	39.9
	25 (12.5)	370.9	372.7	227.7	263.3	155.1	115.2	48.0
	30 (15.0)	446.5	451.5	270.5	316.0	183.1	139.5	58.2
Semi-bonded	5 (2.5)	76.9	70.5	45.5	52.9	32.4	30.6	5.9
	10 (5.0)	149.4	143.3	91.9	103.5	60.1	56.1	13.4
	15 (7.5)	224.1	212.8	138.2	149.5	86.4	81.3	23.4
	20 (10.0)	297.2	287.9	183.7	198.9	108.1	109.8	31.8
	25 (12.5)	372.2	361.9	231.4	244.8	129.3	138.3	42.1
	30 (15.0)	447.2	442.3	274.3	295.7	147.5	169.9	51.2
Fully Debonded	5 (2.5)	66.5	64.2	49.9	11.1	-4.3	82.3	18.6
	10 (5.0)	140.7	136.2	101.8	22.2	-2.0	93.4	42.2
	15 (7.5)	216.5	210.3	152.6	34.7	8.1	98.8	69.8
	20 (10.0)	289.8	287.6	202.5	50.3	22.9	93.0	101.8
	25 (12.5)	365.4	358.5	255.0	62.6	32.0	83.4	134.2
	30 (15.0)	441.8	440.7	305.8	81.2	51.2	74.8	176.2
Semi-debonded	5 (2.5)	72.5	75.2	42.2	40.3	10.5	22.4	14.6
	10 (5.0)	148.7	147.6	88.6	70.7	17.5	56.5	27.3
	15 (7.5)	222.5	222.2	132.5	105.0	26.7	92.9	38.8
	20 (10.0)	297.9	292.3	176.1	136.3	34.3	132.6	49.0
	25 (12.5)	374.4	369.2	221.6	170.9	46.6	174.0	62.4
	30 (15.0)	450.6	445.2	263.6	199.4	54.1	207.7	75.8
Debonded	5 (2.5)	73.6	77.4	47.8	40.3	7.0	20.7	13.1
	10 (5.0)	148.7	149.2	93.9	83.7	3.9	37.9	24.5
	15 (7.5)	223.4	223.1	139.4	127.0	5.7	55.6	37.7
	20 (10.0)	298.0	298.6	182.8	170.4	7.9	74.4	51.8
	25 (12.5)	374.6	372.9	228.8	212.4	11.4	90.1	66.0
	30 (15.0)	451.8	448.1	273.2	251.3	13.0	100.4	79.3

Appendix 15 – Detailed Bone and Implant Modeling Process

The following procedure outlines a process used to generate finite element models of bonded and debonded implants cemented in bone.

Step 1: 3D Surface Development from a CT file

- A. Using the 'Microview' program (available at microview.sourceforge.net) convert the .vff files obtained from the microCT scanner to DICOM files.
- B. In Mimics, select File/Import Images and select the folder containing the DICOM files for one bone. Press and then , a window will appear requesting verification of image orientation in the orthogonal planes, as shown in Figure A.8. If necessary right click on the orientation characters to modify their layout, otherwise select to proceed. The plane layout will now be displayed in the main window in addition to a 3D representation of the bone. The scroll wheel may be used to look at cross-sections throughout the bone and control-rightclick used to manipulate the zoom.

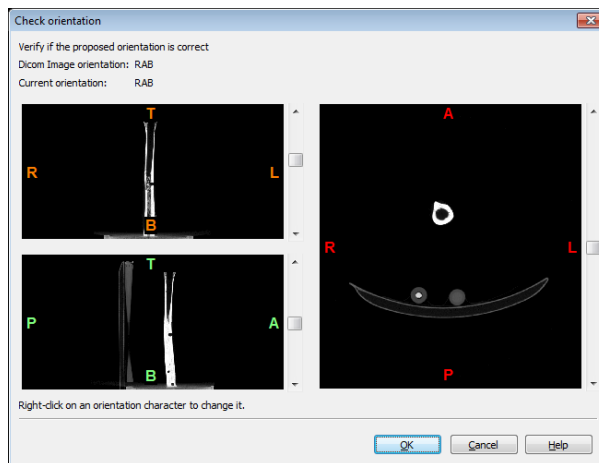



Figure A.8: Verification of 3D image orientation.

This window appears when importing DICOM files into Mimics to allow for selection of image orientation.

Step 1.1: 3D Bone Surface Development

- A. To develop a 3D model of the bone, the image must first be sectioned through thresholding, which allows the user to develop a segmented object containing only those pixels within selected minimum and maximum threshold values.
 - i. Click the thresholding icon () in the top left corner of the segmentation module to begin.
 - ii. A window will appear allowing user to vary the minimum and maximum thresholding values via a slider or by typing the desired values into the appropriate text boxes (Figure A.9). As the threshold values are adjusted the selected pixels will be visualized as a colored mask.
 - iii. When the desired values have been selected, click the 'Fill holes' and 'Keep largest' checkboxes to limit the voids in the developed mask and focus the mask on the largest pixel grouping.

- iv. Click to generate the mask, which will appear in the top right side of the Mimics window under the 'Masks' tab.

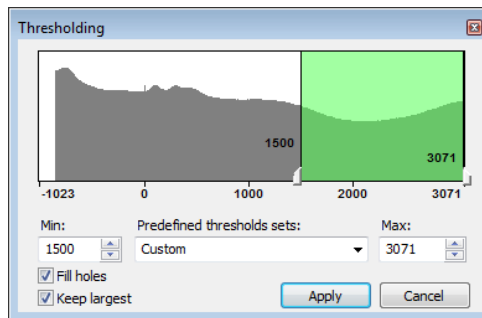





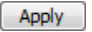


Figure A.9: Thresholding

The user may vary the minimum and maximum thresholding values via the slider or by typing the desired values into the appropriate text boxes. The 'Fill holes' and 'Keep largest' check boxes to limit the voids in the developed mask and focus the mask on the largest pixel grouping respectively.

- B. From the new mask limit the length of the bone by using the Region Growing function. This will enable the user to generate a new mask focused on a selected region of interest without extraneous proximal or distal data.
- i. Click the Region Growing icon () and select the desired mask from the 'Source:' dropdown list.
 - ii. In the target dropdown list select <New Mask>, and uncheck both the 'Leave Original Mask' and 'Multiple Layer' checkboxes.
 - iii. Select the most proximal and distal layers by clicking on the colored region in the axial view. Select the 'Multiple Layer' checkbox and click on the colored region in any slice between the previously selected layers to fill the region in-between.

- iv. A new mask will now be available under the 'Masks' tab containing only the selected region of interest.
- C. The newly formed regional mask will contain large internal voids that need to be eliminated.
- i. In the 'Masks' tab select the regional mask and click 'Calculate 3D from Masks' (). In the window that appears select a quality level of 'Optimal', and press . This will develop a 3D image with the most favorable ratio between quality and development time.
 - ii. A new object will now appear in the 3D visualization window and be available in the '3D Objects' tab on the middle right side of the Mimics window.
 - iii. Click the 'Calculate polylines from 3D' button () and select the newly created 3D image.
 - iv. A series of polylines will be displayed in both the axial view and in the 3D visualization window.
 - v. To isolate the outer contours and remove the inner polylines click 'Cavity fill from polylines' (). Select the polylines to be filled in the 'Fill cavity of:' drop down list and enter <New Mask> in the 'Using Mask:' field. Click  to complete this action and generate a filled mask. See Figure A.10 for an axial view of a filled mask and source polyline series.

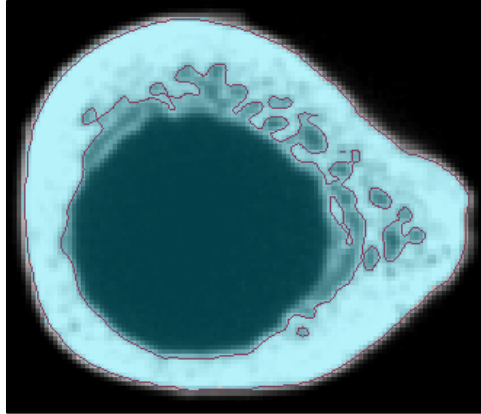







Figure A.10: Axial view of a polyline series and mask

The polyline series (purple) was used to generate the filled mask (blue) using 'Cavity fill from polylines'.

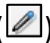

- D. Excess tissue on the exterior of the bone and any remaining cavities must be filled manually using 'Edit Masks' () or 'Multiple Slice Edit' () to generate a solid mask. Both functions allow the user to draw, erase, or threshold areas on the mask with a variable size and shape modification tool. The 'Edit Masks' function allows the user to modify each image independently while the 'Multiple Slice Edit' tool allows users to carry modifications to neighbouring frames.
- E. Using the newly edited mask, polylines need to be created to represent the outer surface of the bone.
- i. Click 'Calculate Polylines' () and select the fully edited mask, then click to proceed.
 - ii. The newly created polylines may contain instances where two or more contours are on the same plane. To eliminate this error select 'Polyline Growing' (). In the 'From:' drop down list enter the source polylines and enter 'New Set' in the 'To:' field. Check 'Auto multi-select' to allow

neighbouring frames containing only one contour to be automatically selected.

In the axial window select the polylines on each plane until all of the desired contours are selected.

- F. To generate a 3D surface for exporting the polylines must be converted into a surface CAD Object.
- i. Right click on the desired polyline set and select 'Fit Surface'. In the window that appears the u and v-parameters may be adjusted to modify the splines in generating the surface. Where the higher the u and v-parameters the better the fit, but also the greater the errors at the extremities.
 - ii. After selecting , the new surface will appear in the middle-right side of the Mimics window under the 'CAD Objects' tab. Right click on the surface, select 'Iges Export...' () and the file to the desired computer folder, before clicking to export.

Step 1.2: 3D Cement Surface Development

- A. To develop a 3D model of the cement the image must first be sectioned through thresholding. To do this follow the actions outlines in Step 1.1 (A), but do not select the 'Fill holes' and 'Keep largest' checkboxes.
- B. The generated mask will contain excess pixels exterior to the bone. These may be removed using 'Edit Masks' () and 'Multiple Slice Edit' () thereby restricting the mask to the pixels in the internal channel.

- C. To complete the generation of a 3D cement surface repeat Step 1.1 (C-F) for the internal canal mask.

Step 2: 3D Model Development from 3D Surface

- A. The .igs files exported from Mimics are open ended hollow shells; however solidity may be added to the 3D surfaces in Abaqus®.
- i. To import the file, open Abaqus®, click file/import/part and select the bone .igs file. Ctrl-Alt and mouse movement may be used to rotate the bone and the scroll wheel used to manipulate the zoom.
 - ii. The ends of the part are currently open. To close these faces select Tools/Geometry Edit/Face/Cover Edges in the 'Part' module and select the distal and proximal edges on the bone (Figure A.11).
 - iii. To fill the hollow part, select Shape/Solid/Form Shell, select the distal surface of the bone and fill inwards. The bone will now be solid.
 - iv. Repeat this process with the cement IGS file to generate to generate a solid cement body.
 - v. Repeat step (i) to import the implant into the model.

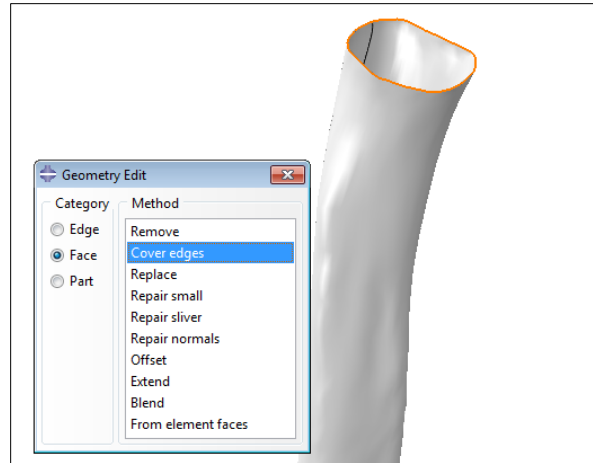










Figure A.11: Editing the geometry of the imported bone IGS file

Editing was performed on a surface in order to close the distal end of the part. The selected surface is highlighted in orange.

- B. All of the parts are now available in the model and may be fit together to represent the experimental setup. As the cement and bone are both oriented as they were experimentally they may be easily merged in the 'Assembly' module.
- i. Import the parts into the same instance by selecting Instance/Create and selecting the parts as dependents.
 - ii. To join the cement and bone select Instance/Merge/Cut Instances and with the parts selected opt to 'retain boundaries' so as not to merge the cement and bone and 'suppress original' to keep only the newly created cement-bone part.
 - iii. To reduce potential errors at the extremities due to the original polyline fitting during shell formation in Mimics, remove the distal 0.4 mm of the assembly using the 'Create Datum Plane: 3 Points' () , 'Create Datum Plane: Offset from Plane' () , and 'Create Cut: Extrude' () functions.

- C. The orientation of the implant will vary from that of the bone-cement setup. However, it may be oriented in the bone by aligning the distal surface of the bone with the proximal surface of the implant head, as well as, the boundaries and alignment of the cement canal with the positioning and alignment of the implant stem. Multiple functions are used in this process, in particular 'Create Datum Plane: 3 Points' () , 'Create Datum Point: Enter Coordinates' () in the 'Part' module, as well as, 'Translate Instance' () , 'Translate To' () , and 'Rotate Instance' () in the 'Assembly' module are all necessary for this task.



NOTE: It is critical that the implant is adapted to match the bone's orientation. At no point in this process may the bone's position be altered.

- D. Once satisfied with the implant orientation combine the implant and cement using Instance/Merge/Cut Instances and with the parts selected opt to 'retain boundaries' so as not to merge the implant and cement and 'suppress original' to keep only the newly created implant-cement-bone part.
- E. To simplify the identification of areas of strain monitoring and the application of material properties at this point it is helpful to separate the assembly into two parts, one containing the bone and the other the implant and cement. This may be accomplished by generating two copies of the complete part and in the 'Part' module removing the desired cells using Tools/Geometry Edit.../Face/Remove.

Step 3: Identifying Areas of Strain Monitoring in 3D Model

Step 3.1: External Gauges

A. During experimental testing MicroScribe data was collected of the external gauge locations, and a coordinate system developed based on three identifiable points along a notch in the PVC cylinder used to pot the bone. These same coordinate points were identified on the CT images in Mimics (Figure A.12).

- i. To find points in Mimics under the 'CAD Objects' tab click 'New' () /point/draw and using the stylus that appears place a point in the desired location. Coordinates may be viewed by selecting the point in the 'CAD Objects' tab and selecting 'Properties' ()

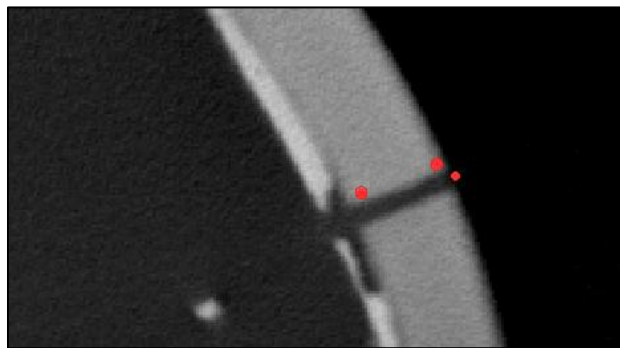
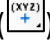


Figure A.12: Axial view of the coordinate points selected in Mimics

The three coordinate points (red) were based on a linear marking placed on the PVC potting fixture of specimen 09-12057R prior to CT'ing.


B. Using the matrix equations outlined in Equation 9 and Equation 10 the MicroScribed points on the external gauges were converted to the CT coordinate

system and plotted on the Abaqus® model using the ‘Create Datum Point: Enter Coordinates’ () function.

$$\begin{bmatrix} \text{MicroScribeT} \\ \text{BoneT} \end{bmatrix} \begin{bmatrix} \text{BoneT} \\ \text{CTT} \end{bmatrix} = \begin{bmatrix} \text{MicroScribeT} \\ \text{CTT} \end{bmatrix} \quad \text{Equation 9}$$

$$\begin{bmatrix} \text{MicroScribeT} \\ \text{CTT} \end{bmatrix} \begin{bmatrix} \text{MicroScribeP} \\ \text{External GaugesP} \end{bmatrix} = \begin{bmatrix} \text{External GaugesP} \\ \text{CTP} \end{bmatrix} \quad \text{Equation 10}$$

- Where:
- $\begin{bmatrix} \text{MicroScribeT} \\ \text{BoneT} \end{bmatrix}$ - Transformation matrix of the bone coordinates in relation to the MicroScribe
 - $\begin{bmatrix} \text{BoneT} \\ \text{CTT} \end{bmatrix}$ - Transformation matrix of the CT coordinates in relation to the bone
 - $\begin{bmatrix} \text{MicroScribeT} \\ \text{CTT} \end{bmatrix}$ - Transformation matrix of the CT coordinates in relation to the MicroScribe
 - $\begin{bmatrix} \text{MicroScribeT} \\ \text{CTT} \end{bmatrix}$ - Transformation matrix of the MicroScribe coordinates in relation to the CT
 - $\begin{bmatrix} \text{MicroScribeP} \\ \text{External GaugesP} \end{bmatrix}$ - Coordinates of the external gauges with respect to the MicroScribe
 - $\begin{bmatrix} \text{MicroScribeP} \\ \text{External GaugesP} \end{bmatrix}$ - Coordinates of the external gauges with respect to the CT

- C. Using the previously formed points and the ‘Partition Face: Sketch’ () function a circular section (2 mm diameter) was portioned from the surface of the bone at each gauge location. The pixels within the circular gauge sections will be averaged to determine the external strain at those locations. The completed bone post sectioning is shown in Figure A.13.

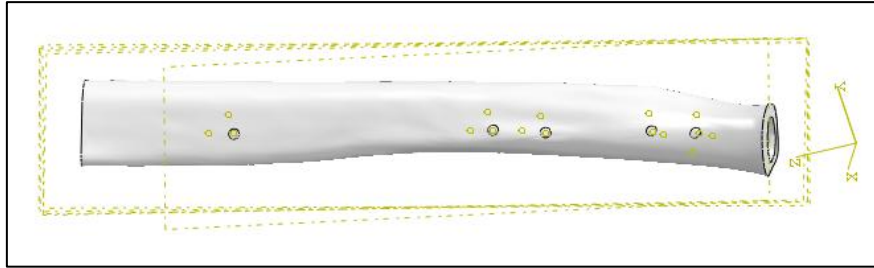


Figure A.13: Bone model segmented to denote external gauge locations.

The gauge points (yellow circles) and datum planes (yellow hash lines) upon which the segmentation is based are also visible.

Step 3.2: Internal Gauges

- A. Post fixation of the internal gauges on the implant MicroScribe data was collected of the internal gauge locations, and a coordinate system developed based on four identifiable points on the implant head. These same coordinate points were identified on the implant in Abaqus®, as shown in Figure A.14.

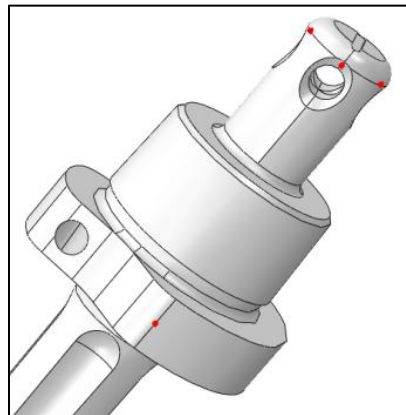
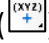


Figure A.14: Axial view of the implant coordinate points


The three coordinate points (red) were selected experimentally with the MicroScribe and in Abaqus® to form the implant coordinate system.

- B. Using the matrix equations outlined in Equation 11 and Equation 12 the internal gauges MicroScribed points were converted to the Abacus coordinate system and plotted on the model using the 'Create Datum Point: Enter Coordinates' () function.

$$\begin{bmatrix} \text{Implant}_T \\ \text{MicroScribe}_T \end{bmatrix} \begin{bmatrix} \text{MicroScribe}_T \\ \text{Internal Gauges}_T \end{bmatrix} = \begin{bmatrix} \text{Implant}_P \\ \text{Internal Gauges}_P \end{bmatrix} \quad \text{Equation 11}$$

$$\begin{bmatrix} \text{Abacus}_T \\ \text{Implant}_T \end{bmatrix} \begin{bmatrix} \text{Implant}_P \\ \text{Internal Gauges}_P \end{bmatrix} = \begin{bmatrix} \text{Abacus}_P \\ \text{Internal Gauges}_P \end{bmatrix} \quad \text{Equation 12}$$

- Where:
- $\begin{bmatrix} \text{Implant}_T \\ \text{MicroScribe}_T \end{bmatrix}$ - Transformation matrix of the implant coordinates in relation to the MicroScribe
 - $\begin{bmatrix} \text{MicroScribe}_P \\ \text{Internal Gauges}_P \end{bmatrix}$ - Coordinates of the internal gauges with respect to the MicroScribe
 - $\begin{bmatrix} \text{Implant}_P \\ \text{Internal Gauges}_P \end{bmatrix}$ - Coordinates of the internal gauges with respect to the implant
 - $\begin{bmatrix} \text{Abacus}_T \\ \text{Implant}_T \end{bmatrix}$ - Transformation matrix of the implant coordinates in relation to Abacus
 - $\begin{bmatrix} \text{Abacus}_P \\ \text{Internal Gauges}_P \end{bmatrix}$ - Coordinates of the internal gauges with respect to Abacus

- C. Using the previously formed points and the 'Create Solid: Extrude' () function a circular section (2 mm diameter) was portioned from the gauge level to the surface of the cement at each gauge location. The pixels on the internal surface of the gauge sections will be averaged to determine the internal strain at that location. The cement complete with sectioning is shown in Figure A.15.

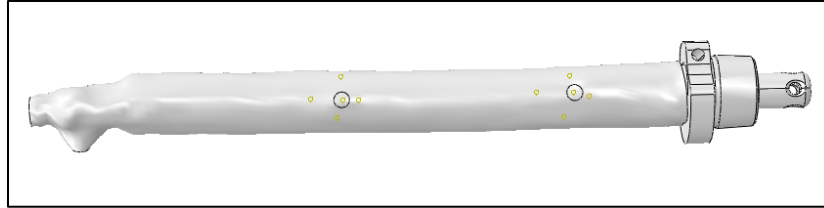

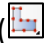





Figure A.15: Implant and cement model segmented to denote gauge locations.

On the implant and cement model the gauges (denoted as black circles) within the cement and gauge points (yellow circles) upon which the gauge locations are based are visible.







Step 4: Generating a Tetrahedral Solid Mesh

A tetrahedral solid mesh was selected and applied with an approximate global size of 0.75 (0.50 for convergence study) and local size of 0.30 (0.20 for convergence study) at the gauge locations on both the bone and implant-cement models.

- i. In the 'Mesh' module and using 'Assign Mesh controls' () , select all parts and apply a 'Tet' mesh. As the only meshing technique compatible with tetrahedral elements is 'Free' the part will turn pink, as shown in Figure A.16(B). Select the default algorithm and to complete the mesh control application.
- ii. Apply an approximate global seed size of 0.75, with a maximum deviation factor in curvature control and minimum size control by fraction of global size of 0.10, using the 'Seed Part' () function.
- iii. To the gauge circles use the 'Seed Edges' () function to apply a local seed size of 0.30.
- iv. To reduce potential errors, mesh segments individually using the 'Mesh Regions' () function, and use the highlight function in 'Verify Mesh' () to

confirm that there are no errors or warnings before proceeding. The fully meshed cement and implant is shown in Figure A.16(C).

v. Should errors or warnings appear several options are available to aid in their removal.

- To manually edit any errors select the 'Edit Mesh' () function and use the Node/Drag feature to manually modify the problematic node.
- Errors resulting from excessively segmented lines or regions may be eliminated by removing the mesh and using 'Virtual Topology: Combine Edges' () or 'Virtual Topology: Combine Faces' () respectively to smooth the edges. The mesh may then be reapplied.
- Segmentation of the region may also be utilized to reduce the area to be meshed on each pass thereby reducing errors. To do this remove the mesh and create a plane perpendicular to the part using 'Create Datum Plane: 3 Points' (). Create additional planes using 'Create Datum Plane: Offset from Plane' (), use 'Partition Cell: Define Cutting Plane' () to Segment the bone at each datum plane, and remesh using the new smaller segments.

NOTE: To reduce meshing errors the distal tip of the implant was excluded from the mesh.

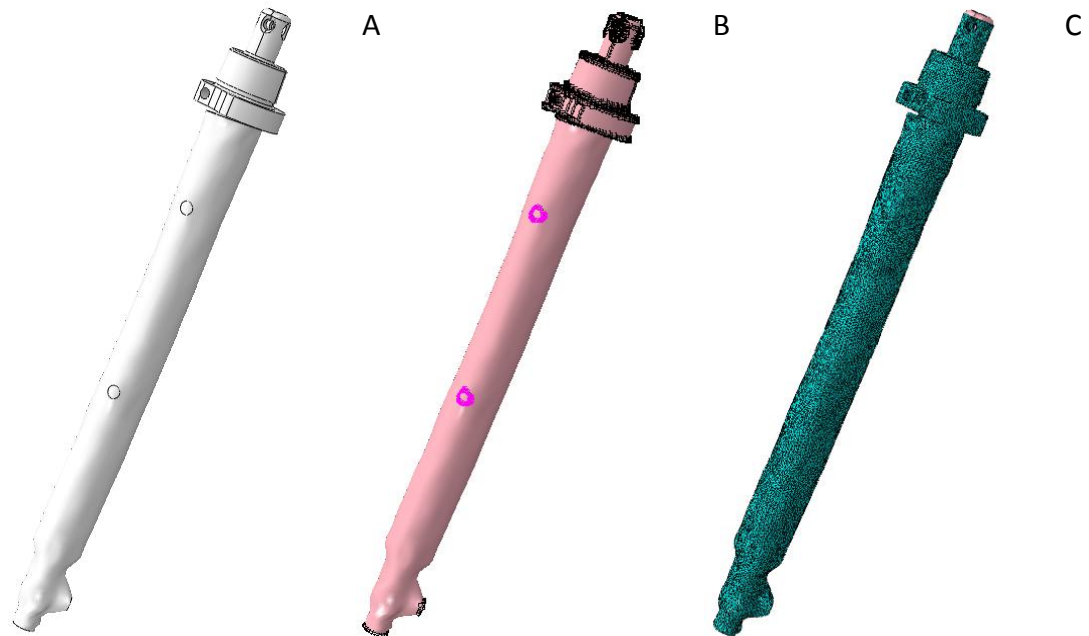




Figure A.16: Implant and cement model


Implant and cement (A) segmented, (B) with mesh controls applied and edges seeded, and (C) meshed.

Step 6: Assign Material Properties

Step 6.1: Homogeneous

- A. To generate the materials for the stem and cement in the 'Property' module select the 'Material Manager' () and click . In the window that appears name the material and assign relevant material properties.
- B. Use the 'Assign Section' () feature to select the cement and implant individually and assign the appropriate material properties.





Step 6.2: Inhomogeneous



- A. Export the meshed bone from Abaqus® as an .inp file.
 - i. Copy the Model containing the meshed bone and implant-cement. In the copied model delete all but the final meshed bone part. Ensure that the assembly has been created with an independent bone instance.
 - ii. In the 'Job' module select the 'Job Manager' () and click . Select the newly created model, name the job and then click and in the windows that appear.
 - vi. Right click on the newly created job and select 'Write Input'.
- B. Use the 'MapFE' program to assign material properties to the bone model.
 - i. Specify the 'Number of Materials' as the number of material groupings in which the range of elastic moduli (E) determined for the bone may be divided into. (Selection of 400 materials for an ulna is recommended.)
 - ii. Using the browse buttons specify the path to the exported INP bone file in the 'INP Input' field, the original .vff files in the 'VFF Input' field, and desired output location in the 'INP Output' field.
 - iii. If available select the 'Material Definition File:' from the desktop. Otherwise enter the appropriate values in the associated fields.
 - Calibrate - Specify the calibration units to convert Hounsfield units to ash density, using two points to define a linear relationship.

- Scale - State the conversion factor from ash to apparent density.
 - E-relate - Provide the density-modulus relationship.
 - V-relate - Identify Poisson's ratio.
- iv. Select 'Start' to begin the program.
- C. Import the file to Abaqus® as a second-order tetrahedral orphan mesh by clicking File/Import/Model... and selecting the new .inp file. Copy the bone part into the module containing the implant and cement part.

Step 5: Apply Node Sets to Areas of Desired Strain Measurement

To record strains within a select area a set may be created to isolate strains within a given region. As such, a unique set is required for each of the internal and external strain gauges.

- i. In the bone part, right click on the 'Sets' list item and select Create.../Element, name the set and select .
- ii. Using the 'Select the Entity Closest to the Screen' () , 'Select from Exterior Entities' () , 'Use Circular Drag Shape' () and 'Select Entities Inside and Crossing the Drag Shape' () tools, select the surface elements within the previously sectioned circular gauge areas. The completed node sets for the internal gauges is shown in Figure A.17.

- iii. Repeat this process for the gauges within the cement using 'Select from All Entities' () and 'Use Rectangular Drag Shape' () to pick the elements on the circular interior surface of the sectioned gauge area.

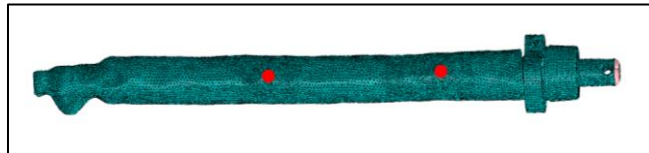



Figure A.17: Completed node set for both internal gauge locations

The circular node sets are shown in red and, though they appear to be located on the cement surface, the nodes selected are within the body of the cement.

Step 7: Generate Bonded/Debonded Model

At this point the cement-implant and bone parts may be combined to form either the bonded or debonded model. Prior to development any instances in the assembly of the current parts model must be removed and two copies of the model generated. These copies will become the bonded and debonded models.


Step 7.1: Bonded

In the 'Assembly' module click 'Instance Part' () and select both the implant-cement and bone parts. An assembly will now be generated with both components

Step 7.2: Debonded

- A. Isolate both the implant and the cement. This may be accomplished by generating two copies of the complete part and in the 'Part' module removing the desired cells



using Tools/Geometry Edit.../Face/Remove. If the mesh was removed in the process of completing this action it will need to be reapplied.

- B. In the 'Assembly' module click 'Instance Part' () and select both the implant, cement, and bone parts. An assembly will now be generated with all three components



Step 8: Apply Load, Boundary Conditions, Constraints and Interactions

Step 8.1: Loading/Boundary Conditions and Constrains

This section will need to be completed for both the bonded and debonded models.


- A. In the implant part generate an applied load at the distal end of the implant
- i. In the bone part right click on the 'Sets' list item and select Create.../Node, name the set and click . Select the nodes by 'Feature Edge' and record the number of nodes selected.
 - ii. In the 'Part' module use 'Create Datum CSYS: 3 Points' () to select three points on the loading area and generate a loading coordinate system.
 - iii. In the 'Load' module select 'Create Load' () , chose 'Concentrated Force' and use the previously generated loading set to select the location of the load. Select the loading coordinate system enter the force in the appropriate direction.


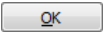
NOTE: The force will be applied per node.

- B. Generate a boundary condition on the proximal surface of the bone.
- Right click on the 'Sets' list item and select Create.../Node, name the set and click . Select the nodes 'by angle' and select the proximal face of the bone.
 - In the 'Load' module select 'Create Boundary Condition' () chose 'Symmetry/Antisymmetry/Encastre' and use the previously generated boundary condition set to select the proximal end of the bone as a 'pinned' boundary condition.
- C. Constrain the external cement to the internal bone surface. This functionality is available in the 'Interaction' module. Use 'Create Constraint' () to create a 'Tie' constraint, and select both master and slave surfaces. The slave surface should be the one with a finer mesh, or if the meshes are approximately equal the surface with a smaller elastic modulus.


Step 8.2: Interface Interactions

As the implant and cement are connected in the bonded scenario this section is only required for the debonded model.



- In the 'Interaction' module, select 'Create Interaction Property' () name the property, and pick 'Contact'.
- In the window that opens select Mechanical/Tangential Behavior.
- Select the desired 'Friction formulation', enter the appropriate 'Friction Coeff', and adjust the other properties as required. When finished click .

- D. Select the 'Interactions' () icon, name the interaction and pick the desired type. For 'Penalty' interactions 'Surface-to-surface contact' is recommended.
- E. Select the desired master and slave surfaces from the model. From the 'Contact interaction property:' dropdown list chose the previously created interaction property. When finished select .

Step 9: Create and Run Job

- A. In the 'Job' module click 'Create Job' () and select the desired model. In the 'Edit Job' window enter the job details, such as, the directory in which to store data, the amount memory allocation, and number of processors to be used.

NOTE: Using additional processors also uses an equal number of additional tokens on the license.

- B. To check for errors and warnings in the model prior to running the full analysis, right click on the job name and select 'Data Check'.
- C. Once satisfied with the functionality of the model, right click on the job and select 'Submit'.
- D. Once the job has completed the results may be viewed by right clicking on the job and selecting 'Results'. Use 'Plot Contours on Deformed Shape' () to view deformations and strain gradients within the model. Use 'Probe Values' () to view stress or strain gradients in a particular region or at an element face or node. The probe values window is shown in Figure A.18.

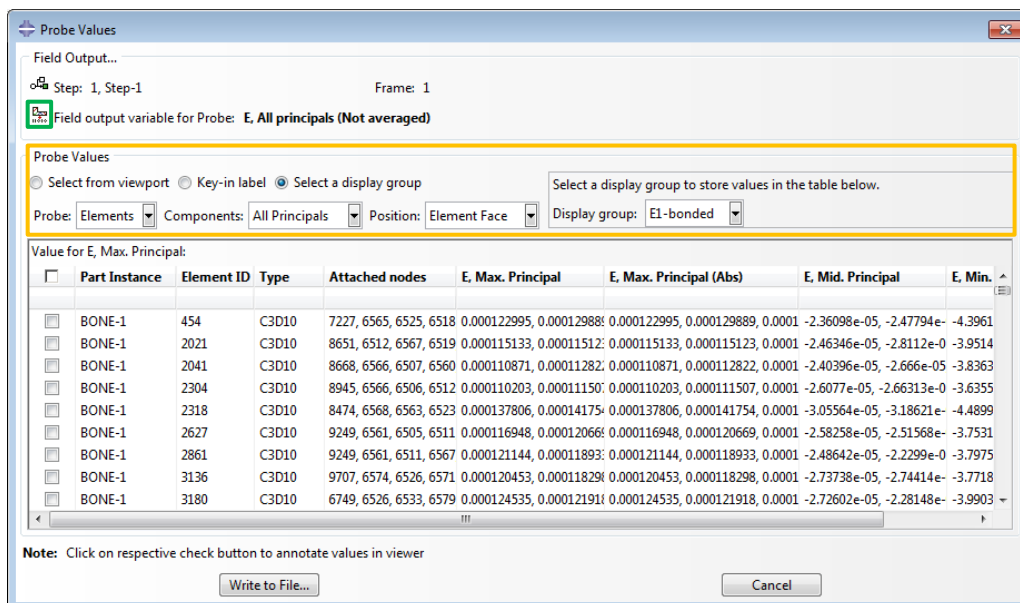


Figure A.18: Probe values input window

Selecting the icon in the green rectangle allows modification of field output variables, while any modifications made to the components within the orange box will alter the areas selected for value identification.

Curriculum Vitae

SAYWARD R. FETTERLY

Education

Master of Engineering Science, Mechanical and Materials Engineering University of Western Ontario, London, Ontario, Canada	2010 – 2012
Bachelor of Engineering, Biological Engineering, Honours Co-Op University of Guelph, Guelph, Ontario, Canada	2003 – 2008

Research Projects and Awards

Masters in Mechanical Engineering, University of Western Ontario Determining the effect of implant-cement interface debonding on strains in the cement and bone surrounding a distal ulnar implant in a cadaver bone.	2012
Project Soy Competition, Third Place Designed and developed a line of edible candy art supplies containing soy as a primary ingredient.	2008
Biological Eng Design IV, University of Guelph Designed and modeled a cardiac implant to reduce mitral valve regurgitation in canines.	2008
Project Soy Competition, Third Place Researched and developed a flexible fabric made from waste soy stock.	2007
Biological Eng Design III, University of Guelph Designed a prosthetic ankle joint that maintained stability while allowing for ankle flexion.	2007
Project Soy Competition, Third Place Created a healthy nacho chip containing soy as a primary ingredient.	2006
Guelph Creative Recycling Initiative, Third Place Designed and developed a sound-blocking material from environmentally friendly components.	2006
Bioinstrumentation Design, University of Guelph Researched and created a bite-measuring instrument to detect jaw instability in patients with clenching disorders.	2006
Project Soy Competition, First Place Design and developed of a low-fat, heart-healthy doughnut containing soy as a primary ingredient.	2005

Canadian Appropriate Technologies in Mine Action Competition, Second Place 2004
Designed an adaptable below-knee prosthetic for landmine victims in third-world countries.

Teaching Experience

Teaching Assistant - Robotics and Manufacturing Automation University of Western Ontario	2011 – 2012
Teaching Assistant - Fluid Machinery University of Western Ontario	2011
Continuing Education Tutor Upper Grand District School Board	2008

Conference Presentation

Fetterly, S.R., King, G.J., Dunning, C.D, (2012) Development of an Experimental Technique to Quantify Cement Mantle Strains in the Distal Ulna. *Ontario Bioengineering Conference*, Barrie, Ontario (Poster)

Professional Work Experience

Management Trainee ShawCor Ltd, Toronto, On	2008 – 2010
Environment, Health and Safety Team Member (Ergonomics), Co-op GE-Hitachi Nuclear Energy Canada Inc, Arnprior, On	2007
Materials Testing – Inside Sales Support, Co-op Hoskin Scientific, Burlington, On	2006
Materials Testing – Inside Sales Support, Co-op Baylis Medical, Mississauga, On	2006

Meetings Attended

Canadian Orthopedic Research Society Annual Meeting Ottawa, Ontario	2012
Ontario Bioengineering Conference Barrie, Ontario	2012
ASME Summer Bioengineering Conference Farmington, Pennsylvania	2011